


5-2013

# Development of a PDMS Based Micro Total Analysis System for Rapid Biomolecule Detection

Balaji Srinivasan Venkatesh  
*University of Arkansas, Fayetteville*

Follow this and additional works at: <http://scholarworks.uark.edu/etd>

 Part of the [Biomechanical Engineering Commons](#), and the [Electro-Mechanical Systems Commons](#)

---

## Recommended Citation

Srinivasan Venkatesh, Balaji, "Development of a PDMS Based Micro Total Analysis System for Rapid Biomolecule Detection" (2013). *Theses and Dissertations*. 594.  
<http://scholarworks.uark.edu/etd/594>

This Dissertation is brought to you for free and open access by ScholarWorks@UARK. It has been accepted for inclusion in Theses and Dissertations by an authorized administrator of ScholarWorks@UARK. For more information, please contact [scholar@uark.edu](mailto:scholar@uark.edu), [ccmiddle@uark.edu](mailto:ccmiddle@uark.edu).



DEVELOPMENT OF A PDMS BASED MICRO TOTAL ANALYSIS SYSTEM FOR RAPID  
BIOMOLECULE DETECTION

DEVELOPMENT OF A PDMS BASED MICRO TOTAL ANALYSIS SYSTEM FOR RAPID  
BIOMOLECULE DETECTION

A dissertation submitted in partial fulfillment  
of the requirements for the degree of  
Doctor of Philosophy in Mechanical Engineering

By

Balaji Srinivasan Venkatesh  
Pondicherry University  
Bachelor of Technology in Mechanical Engineering, 1999  
University of Arkansas  
Master of Science in Mechanical Engineering, 2005

May 2013  
University of Arkansas

## **ABSTRACT**

The emerging field of micro total analysis system ( $\mu$ TAS) powered by microfluidics is expected to revolutionize miniaturization and automation for point-of-care-testing systems which require quick, efficient and reproducible results. In the present study, a PDMS based  $\mu$ TAS has been developed for rapid, multi-purpose, impedance based detection of biomolecules. The major components of the  $\mu$ TAS include a micropump, micromixer, magnetic separator and interdigitated electrodes for impedance detection. Three designs of pneumatically actuated PDMS based micropumps were fabricated and tested. Based on the performance test results, one of the micropumps was selected for integration. The experimental results of the micropump performance were confirmed by a 2D COMSOL simulation combined with an equivalent circuit analysis of the micropump. Three designs of pneumatically actuated PDMS based active micromixers were fabricated and tested. The micromixer testing involved determination of mixing efficiency based on the streptavidin-biotin conjugation reaction between biotin conjugated fluorescent microbeads and streptavidin conjugated paramagnetic microbeads, followed by fluorescence measurements. Based on the performance test results, one of the micromixers was selected for integration. The selected micropump and micromixer were integrated into a single microfluidic system. The testing of the magnetic separation scheme involved comparison of three permanent magnets and three electromagnets of different sizes and magnetic strengths, for capturing magnetic microbeads at various flow rates. Based on the test results, one of the permanent magnets was selected. The interdigitated electrodes were fabricated on a glass substrate with gold as the electrode material. The selected micropumps, micromixer and interdigitated electrodes were integrated to achieve a fully integrated microfluidic system. The fully integrated microfluidic system was first applied towards biotin conjugated fluorescent

microbeads detection based on streptavidin-biotin conjugation reaction which is followed by impedance spectrum measurements. The lower detection limit for biotin conjugated fluorescent microbeads was experimentally determined to be  $1.9 \times 10^6$  microbeads. The fully integrated microfluidic system was then applied towards immuno microbead based insulin detection. The lower detection limit for insulin was determined to be  $10^{-5}$ M. The total detection time was 20 min. An equivalent circuit analysis was performed to explain the impedance spectrum results.

This dissertation is approved for recommendation  
to the Graduate Council.

Dissertation Director:

---

Dr. Chao-Hung Steve Tung

Dissertation Committee:

---

Dr. Yanbin Li

---

Dr. Douglas E. Spearot

---

Dr. Uchechukwu C. Wejinya

---

Dr. Po-Hao Adam Huang

**DISSERTATION DUPLICATION RELEASE**

I hereby authorize the University of Arkansas Libraries to duplicate this dissertation when needed for research and/or scholarship.

Agreed

\_\_\_\_\_  
*Balaji Srinivasan Venkatesh*

Refused

\_\_\_\_\_  
*Balaji Srinivasan Venkatesh*



## **ACKNOWLEDGEMENTS**

I would like to thank my advisor Dr. Steve Tung for his guidance, encouragement and support in this project. I would also like to thank Dr. Yanbin Li for giving me an opportunity to work with his lab members, helping me learn about impedance biosensors and providing me valuable suggestions related to the biological aspects of this project. I would like to express my appreciation to my advisory committee, Dr. Po-Hao Adam Huang, Dr. Uchechukwu C. Wejinya, and Dr. Douglas E. Spearot for their critical comments on my research. Also, I would like to express my gratitude to HiDEC staff members, Mr. Errol Porter and Mr. Michael Glover.

## **DEDICATION**

I would like to dedicate this dissertation to my father, Srinivasan Rengasamy, for having faith in me, for providing continued support and encouragement, without which I could not have completed this work.

## TABLE OF CONTENTS

<b>1. INTRODUCTION</b>	<b>1</b>
1.1. Microelectromechanical Systems (MEMS)	1
1.2. Microfabrication	2
1.2.1. Fabrication Materials for Microfluidic Devices	4
1.3. Miniaturization of Diagnostic Assays	6
1.4. Microfluidic System Designs	8
1.4.1. Capillary	8
1.4.2. Pressure Driven	9
1.4.3. Other Systems	10
1.5. Biosensing	11
1.6. Pathogens and Biomolecules	13
1.6.1. Bacteria and Viruses	13
1.6.2. Insulin	14
1.7. Conventional Biodetection Methods	16
1.7.1. Limitations of Conventional Biodetection Methods	17
1.8. Biosensor	18
1.8.1. Bio-Recognition Element	19
1.8.2. Transducer Element	20
1.9. Immunoassay	22
1.9.1. Pretreatment of Biological Samples	23

1.9.2. Micro/Nano Magnetic Bead Immunoassay	24
1.9.3. Immunomagnetic Separation	25
1.10. Micro Total Analysis System	26
1.10.1. Microchannels	27
1.10.2. Micropump	28
1.10.3. Micromixer	30
1.10.4. Microseparator	31
1.10.5. Microsensor	32
1.11. Primary Objectives of Study	33
1.11.1. Specific Tasks	34
1.12. Dissertation Organization	35
<b>2. THEORY AND DESIGN</b>	<b>36</b>
2.1. Micropump	36
2.1.1. Working Principle	36
2.1.2. Micropump Geometry	37
2.2. Micromixer	40
2.2.1. Working Principle	40
2.2.2. Micromixer Geometry	43
2.3. Integration of Micropump and Micromixer	45
2.4. Impedance Spectroscopy	47
2.4.1. Impedance Spectrum Measurement for a Microfluidic System	48

2.4.2. Design of IDE	49
2.5. Magnetic Separation Techniques	52
2.6. Integration of Micropump, Micromixer, and IDE	53
2.7. Biotin-Streptavidin Interactions in Assay Systems	56
2.7.1. Biotin-Streptavidin Conjugation Reaction	56
2.8. Insulin Detection	58
<b>3. MICROFABRICATION</b>	<b>60</b>
3.1. PDMS Soft Lithography	60
3.2. Mask Design	60
3.3. Fabrication of SU-8 Master Mold	62
3.4. Thick PDMS Casting	65
3.5. Thin PDMS Casting	66
3.6. Oxygen Plasma Bonding	69
3.7. Fabrication of IDE	72
3.7.1. PDMS Bonding with IDE	75
3.8. PDMS-Glass Thermal Bonding	76
3.9. Fully Integrated Microfluidic System	77
<b>4. EXPERIMENTAL SETUP AND TESTING</b>	<b>79</b>
4.1. Surface Modification of PDMS	79
4.2. Micropump Performance Testing	80
4.3. Micromixer Performance Testing	84

4.3.1. Materials	87
4.3.2. Sample Preparation	87
4.3.3. Micromixer and Table Top Mixer Comparison	88
4.3.4. Performance Testing	88
4.3.5. Fluorescence Measurements	89
4.4. Integrated System of Micromixer and Micropump	90
4.5. Impedance Spectrum Measurement	92
4.6. Magnetic Microbead Separation	94
4.6.1. Magnet Selection	94
4.6.2. Magnetic Separation Testing	95
4.7. Fully Integrated System Testing	98
4.8. BCF Microbeads Detection	100
4.9. Insulin Detection	101
4.9.1. Preparation of Magnetic Beads-Antibody Conjugate (MBAC)	101
4.9.2. Activation of Carboxyl Groups	101
4.9.3. Antibody Coupling	102
4.9.4. Coupling Efficiency Determination	103
4.9.5. Insulin Detection	104
<b>5. RESULTS AND DISCUSSIONS</b>	<b>107</b>
5.1. Performance of Micropumps	107
5.1.1. Repeatability of Flow Rate	107

5.1.2. Peak Flow Rate	112
5.2. Micropump Simulation – Equivalent Circuit Analysis	113
5.2.1. Transient Response of the Equivalent Circuit	115
5.3. Micropump Simulation – COMSOL	118
5.4. Performance of Micromixers	125
5.4.1. Qualitative Testing	125
5.4.2. Comparison with Table Top Mixer	126
5.4.3. Mixing Performance Variation with Frequency	127
5.4.4. Mixing Performance Variation with Flow Rate	129
5.5. Performance of Integrated Micromixer and Micropump	131
5.6. Magnetic Microbead Separation Scheme	134
5.6.1. Electromagnets	134
5.6.2. Permanent Magnets	135
5.7. Integrated Microfluidic System Testing	137
5.7.1. Impedance Detection of BCF Microbeads	137
5.7.2. Immuno Microbead Based Insulin Detection	144
<b>6. CONCLUSIONS</b>	<b>150</b>
<b>7. FUTURE WORK</b>	<b>153</b>
7.1. Parallel Processing	153
7.2. Inclusion of Valves	153
7.3. Nanobeads	153

7.4. COMSOL Simulation	153
7.5. PDMS Alignment System	154



## **LIST OF TABLES**

<b>Table 2.11</b> Design dimensions of various IDE designs.....	<b>51</b>
<b>Table 4.1</b> Specification of permanent magnets.....	<b>95</b>
<b>Table 4.2</b> Specification of electromagnets.....	<b>95</b>
<b>Table 5.1</b> Mechanical/Fluidic parameters and their electrical analogues.....	<b>114</b>
<b>Table 5.2</b> Equivalent circuit component values for Design 3.....	<b>116</b>

## LIST OF FIGURES

<b>Figure 1.1</b> Microfluidic systems classified according to their main liquid propulsion principle...	8
<b>Figure 1.2</b> Distribution, by industry of application, of the relative number of works appeared in the literature on detection of pathogenic bacteria.....	12
<b>Figure 1.3</b> Conventional biodetection methods.....	16
<b>Figure 1.4</b> Schematic of a biosensor.....	19
<b>Figure 1.5</b> Schematic of a general analytical process.....	24
<b>Figure 1.6</b> Basic steps of immunomagnetic separation (a) Introduction of the beads and the analyte mixture, (b) mixing and binding of the target analyte to Ab-SPM complex (c) magnetic separation of the Ab-SPM complex and target analyte conjugate, (d) washing of the non-target entities and background fluid by buffer.....	26
<b>Figure 1.7</b> Components of a $\mu$ TAS.....	27
<b>Figure 2.1</b> Cross-sectional view of the actuation mechanism of the pump. (1) Liquid enters the microchannel (2) When compressed air fills the air chambers, the first membrane deflects downwards (3) – (5) sequential actuation of PDMS membranes causing the liquid to be pumped to the right.....	38
<b>Figure 2.2</b> Various layers of the micropump assembly.....	38
<b>Figure 2.3</b> Micropump Design1 – Control Layer.....	39
<b>Figure 2.4</b> Micropump Design2 – Control Layer.....	39
<b>Figure 2.5</b> Micropump Design3 – Control Layer.....	40
<b>Figure 2.6</b> Fluidic layer microchannel design.....	40
<b>Figure 2.7</b> Working of a micromixer with two pneumatically actuated membranes.....	41
<b>Figure 2.8</b> Various layers of the micromixer assembly.....	42
<b>Figure 2.9</b> Micromixer Design1 control layer with two semi-circular air chambers.....	43
<b>Figure 2.10</b> Micromixer Design2 control layer with four quadrant air chambers.....	44

<b>Figure 2.11</b> (a) Micromixer Design3 control layer with six air chambers connected in series (b) Close up view of the Design3 air chambers.....	<b>44</b>
<b>Figure 2.12</b> Fluidic layer of the micromixer with a mixing chamber.....	<b>45</b>
<b>Figure 2.13</b> Different layers of the integrated micromixer-micropump assembly.....	<b>46</b>
<b>Figure 2.14</b> Fluidic layer of the integrated micromixer-micropump.....	<b>46</b>
<b>Figure 2.15</b> Alignment of the layers of integrated micromixer-micropump.....	<b>47</b>
<b>Figure 2.16</b> Components of Impedance.....	<b>48</b>
<b>Figure 2.17</b> Impedance spectrum measurement setup for a microfluidic system.....	<b>49</b>
<b>Figure 2.18</b> (a) Basic IDE features (b) Dimensions of IDE.....	<b>51</b>
<b>Figure 2.19</b> Various layers of an IDE chip assembly.....	<b>52</b>
<b>Figure 2.20</b> Different layers of the fully integrated device assembly.....	<b>54</b>
<b>Figure 2.21</b> Outer dimensions of the control layer.....	<b>54</b>
<b>Figure 2.22</b> Outer dimensions of the fluidic layer.....	<b>55</b>
<b>Figure 2.23</b> Outer dimensions of the IDE layer.....	<b>55</b>
<b>Figure 2.24</b> Outer dimensions of the alignment.....	<b>55</b>
<b>Figure 2.25</b> Biotin Streptavidin conjugation reaction.....	<b>57</b>
<b>Figure 2.26</b> Basic steps insulin sample preparation (a) Introduction of MBAC target insulin, (b) mixing and binding of the target insulin to MBAC (c) magnetic separation of the target insulin and MBAC complex, (d) washing of the unbound insulin by buffer.....	<b>59</b>
<b>Figure 3.1</b> Soft lithography process flow for a PDMS component fabrication.....	<b>61</b>
<b>Figure 3.2</b> Fabrication of SU-8 mold.....	<b>62</b>
<b>Figure 3.3</b> Thick PDMS casting process.....	<b>65</b>
<b>Figure 3.4</b> (a) Typical SU-8 mold on Si wafer (b) A thick PDMS fluidic layer.....	<b>66</b>

<b>Figure 3.5</b> Thin PDMS casting process.....	<b>67</b>
<b>Figure 3.6</b> Thin PDMS casting process.....	<b>68</b>
<b>Figure 3.7</b> (a) SU-8 mold on Si wafer for thin PDMS control layer (b) A thin PDMS control layer.....	<b>68</b>
<b>Figure 3.8</b> Process flow for assembling the device.....	<b>69</b>
<b>Figure 3.9</b> Roll PDMS layer to obtain uniform bonding.....	<b>71</b>
<b>Figure 3.10</b> Thick and thin PDMS layers of a micropump bonded together (b) A close view of the alignment of the air chambers over the microchannel.....	<b>71</b>
<b>Figure 3.11</b> Fabrication steps for IDE.....	<b>72</b>
<b>Figure 3.12</b> A typical IDE chip with a close view of the IDE fingers.....	<b>74</b>
<b>Figure 3.13</b> PDMS bonding to IDE.....	<b>75</b>
<b>Figure 3.14</b> PDMS – Glass thermal bonding process.....	<b>76</b>
<b>Figure 3.15</b> A fully integrated microfluidic system.....	<b>78</b>
<b>Figure 3.16</b> A close view of the various components on the fully integrated system.....	<b>78</b>
<b>Figure 4.1</b> (a) 3-port ultra-miniature solenoid valve (SMC part# S070C-5BG-32) (b) Mini Air Compressor (Hargraves part# D730A-23-01).....	<b>81</b>
<b>Figure 4.2</b> Schematic of experimental setup layout for micropump performance testing.....	<b>81</b>
<b>Figure 4.3</b> Experimental setup for micropump performance testing.....	<b>82</b>
<b>Figure 4.4</b> Test fixture for micropump testing with various components.....	<b>83</b>
<b>Figure 4.5</b> 3-port solenoid valve with tubing connected to pressure source and micropump.....	<b>83</b>
<b>Figure 4.6</b> A micropump clamped on the test fixture.....	<b>84</b>
<b>Figure 4.7</b> (a) Initial position of DI water front (b) Final position of DI water front.....	<b>84</b>

<b>Figure 4.8</b> Schematic of an experimental setup layout for micromixer performance testing.....	<b>85</b>
<b>Figure 4.9</b> Experimental setup for micromixer performance testing.....	<b>85</b>
<b>Figure 4.10</b> Test fixture with various components.....	<b>86</b>
<b>Figure 4.11</b> Micromixer clamped on the test fixture.....	<b>86</b>
<b>Figure 4.12</b> (a) VersaFluor Fluorometer (b) a microcuvette with test sample inserted in the cuvette holder and also shown are the excitation and emission filters.....	<b>89</b>
<b>Figure 4.13</b> Schematic of experimental setup for integrated micropump-micromixer testing.....	<b>91</b>
<b>Figure 4.14</b> Experimental setup on an optical table for micropump-micromixer testing.....	<b>92</b>
<b>Figure 4.15</b> (a) A test fixture for integrated micropump-micromixer testing (b) An integrated micropump-micromixer clamped on the test fixture.....	<b>92</b>
<b>Figure 4.16</b> Modified block diagram of Example.vi.....	<b>93</b>
<b>Figure 4.17</b> Modified block diagram of Measure.vi.....	<b>94</b>
<b>Figure 4.18</b> (a) to (c) Permanent magnets (d) to (f) Electromagnets for magnetic separation of SCP beads.....	<b>95</b>
<b>Figure 4.19</b> Schematic of a setup for testing magnets for magnetic separation of SCP beads.....	<b>97</b>
<b>Figure 4.20</b> Experimental test setup on an optical table for magnetic separation of SCP microbeads using an electromagnet.....	<b>97</b>
<b>Figure 4.21</b> (a) Close view of the test fixture showing the electromagnet placed on a lab jack and in contact with the microfluidic device (b) Top view showing the electromagnet in contact with the device.....	<b>98</b>
<b>Figure 4.22</b> (a) Test setup for magnetic separation of SCP beads with a permanent magnet (b) Top view of the device with a permanent magnet positioned on top.....	<b>98</b>
<b>Figure 4.23</b> Schematic of an experimental setup layout for testing a fully integrated device.....	<b>99</b>
<b>Figure 4.24</b> Experimental test setup for fully integrated microfluidic system.....	<b>100</b>
<b>Figure 4.25</b> Test fixture with various components for fully integrated system testing.....	<b>100</b>

<b>Figure 4.26</b> Fully integrated microfluidic system clamped on the test fixture.....	<b>101</b>
<b>Figure 4.27</b> Process flow for BCF microbead detection using the fully integrated microfluidic system.....	<b>102</b>
<b>Figure 4.28</b> Process flow for insulin detection using the fully integrated microfluidic system.....	<b>106</b>
<b>Figure 5.1</b> Flow rate variations within a single Design1 micropump.....	<b>109</b>
<b>Figure 5.2</b> Flow rate variations between three different micropumps of Design1.....	<b>109</b>
<b>Figure 5.3</b> Flow rate variations within a single Design1 micropump.....	<b>110</b>
<b>Figure 5.4</b> Flow rate variations between three different micropumps of Design2.....	<b>110</b>
<b>Figure 5.5</b> Flow rate variations within a single Design3 micropump.....	<b>111</b>
<b>Figure 5.6</b> Flow rate variations between three different micropumps of Design3.....	<b>112</b>
<b>Figure 5.7</b> Equivalent circuit representation of a micropump with four PDMS membranes.....	<b>117</b>
<b>Figure 5.8</b> PSPICE transient response of the equivalent circuit.....	<b>118</b>
<b>Figure 5.9</b> 2D view of the micropump model with multiple layers.....	<b>120</b>
<b>Figure 5.10</b> Material properties of PDMS.....	<b>120</b>
<b>Figure 5.11</b> Definition of global parameters.....	<b>121</b>
<b>Figure 5.12</b> Waveform wv1 definition parameters and plot of waveform wv1.....	<b>122</b>
<b>Figure 5.13</b> Boundary load definition.....	<b>122</b>
<b>Figure 5.14</b> Mesh diagram of membrane M1 before and after deformation.....	<b>123</b>
<b>Figure 5.15</b> Membrane displacements vs membrane arc length at various time instances.....	<b>124</b>
<b>Figure 5.16</b> Membrane displacements vs. arc length of four membranes at t=0.01s.....	<b>124</b>
<b>Figure 5.17</b> Experimental and simulation flow rates variation with frequency.....	<b>125</b>
<b>Figure 5.18</b> Diffusion only mixing at various time instants.....	<b>127</b>

<b>Figure 5.19</b> Active mixing at various time instants.....	<b>127</b>
<b>Figure 5.20</b> Increase in binding efficiency using a micromixer and table top mixer.....	<b>128</b>
<b>Figure 5.21</b> Normalized RFU vs Frequency for three mixer designs.....	<b>129</b>
<b>Figure 5.22</b> Normalized RFU vs. Frequency for individual mixer designs.....	<b>130</b>
<b>Figure 5.23</b> (a) Normalized RFU vs Frequency (b) Mixing efficiency vs Frequency.....	<b>133</b>
<b>Figure 5.24</b> (a) Normalized RFU vs. pressure (b) Mixing efficiency vs. pressure.....	<b>134</b>
<b>Figure 5.25</b> (a) Normalized RFU vs. flow rate (b) Mixing efficiency vs. flow rate.....	<b>134</b>
<b>Figure 5.26</b> Comparison of magnetic field strengths of electromagnets with drag force.....	<b>135</b>
<b>Figure 5.27</b> Comparison of magnetic field strengths of permanent magnets with drag force...	<b>137</b>
<b>Figure 5.28</b> Images of the mixing chamber with a permanent magnet in the background (a) Before the beads were injected into the circular mixing chamber (b) after beads were injected with trapped beads (appears orange in color) inside the mixing chamber.....	<b>138</b>
<b>Figure 5.29</b> Impedance spectrum (Bode plot) for different concentrations of BCF beads.....	<b>139</b>
<b>Figure 5.30</b> The difference in magnitude of impedance (represented by NIC) between $4.8 \times 10^6$ BCF beads and control sample. NIC was calculated for the measurements in the range of frequency from 1 KHz to 10 MHz.....	<b>140</b>
<b>Figure 5.31</b> Magnitude of impedance at 200 kHz for various concentrations of BCF beads....	<b>141</b>
<b>Figure 5.32</b> Equivalent circuit for impedance measurement system.....	<b>141</b>
<b>Figure 5.33</b> Bode plots of the impedance spectra of experimental and curve fitted data of control in the frequency range 10 Hz to 10 Mhz. Solid lines indicate the experimental data and crosses indicate the fitted data obtained from Zview software based on the the equivalent circuit. (a) Magnitude of impedance (b) Phase angle in degrees.....	<b>143</b>
<b>Figure 5.34</b> RFU vs concentration of BSA standards.....	<b>145</b>
<b>Figure 5.35</b> Impedance spectrum (Bode plot) for different concentrations of insulin.....	<b>146</b>
<b>Figure 5.36</b> The difference in magnitude of impedance (represented by NIC) between $10^{-5}$ M insulin sample and control sample. NIC was calculated for the measurements in the range of frequency from 1 KHz to 10 MHz.....	<b>147</b>

**Figure 5.37** Magnitude of impedance at 100 kHz for various concentrations of insulin.....147

**Figure 5.38** Bode plots of the impedance spectra of experimental and curve fitted data of control in the frequency range 10 Hz to 10 Mhz. Solid lines indicate the experimental data and crosses indicate the fitted data obtained from Zview software based on the equivalent circuit. (a) Magnitude of impedance (b) Phase angle in degrees.....148



# 1. INTRODUCTION

## 1.1 Microelectromechanical Systems (MEMS)

MEMS refers to devices that have a characteristic length scale between 1  $\mu\text{m}$  and 1 mm. MEMS devices usually combine electrical and mechanical components and are fabricated using integrated circuit batch-processing technologies. These devices have the ability to sense, control and actuate on the micro scale. Most of the MEMS fabrication methods were developed in the 1970s and 1980s by the silicon microprocessor industry. In 1975, the first analytical MEMS device fabricated on silicon, a gas chromatographic analyzer was reported [1]. This gas chromatograph was able to separate a simple mixture of compounds in a few seconds. Most of the research work during the period from 1975 - 1989 was focused on the microfabrication of silicon based components such as micropumps [2], microvalves [3], and Ion-Sensitive Field-Effect (ISFET) chemical sensors [4]. Some of the early MEMS components that were used in commercial products and applications include accelerometers used to control airbag deployment in vehicles, pressure sensors for medical applications, and inkjet printer heads. In 1990, the silicon-based analyzers re-emerged with a miniaturized open-tubular liquid chromatograph on a silicon wafer [5]. In 1990s, the MEMS industry diversified and devices were fabricated for chemical, biological, and biomedical applications which led to the creation of a new discipline called microfluidics. Microfluidic devices include micrometer sized channels, chambers, filters and other components to manipulate sub- $\mu\text{L}$  to  $\mu\text{L}$  volumes of samples and reagents. Fluid flows in micro devices are significantly different from their macroscopic counterparts. The surface to volume ratio for a machine with a characteristic length of 1 m is  $1 \text{ m}^{-1}$ , while that for MEMS devices with a size of 1  $\mu\text{m}$  is  $10^6 \text{ m}^{-1}$ . The million fold increase in the surface to volume ratio

substantially affects the transport of mass, momentum and energy through the surface. The MEMS component market is expected to reach \$20B in 2016 [6].

## **1.2 Microfabrication**

The two most common methods for production of MEMS devices are surface micromachining and bulk micromachining. Surface micromachining is an additive process. It consists of a series of deposition, patterning and etching of thin films with thickness typically in the range of 1-100  $\mu\text{m}$ . One of the crucial steps in surface micromachining is the selective removal of the underlying film (sacrificial layer) without damaging the overlying films (structural layer). Many commercial MEMS products such as airbag sensors apply this fabrication technique. Bulk micromachining is a subtractive fabrication method which involves patterning and etching of the substrate materials such as silicon, quartz, SiC, GaAs, and glass. The etching can be carried out using orientation dependent (anisotropic) or orientation independent (isotropic) wet etchants. If the process requires a dry environment, deep reactive ion etching (DRIE), a Bosch process invented and patented by Robert Bosch GmbH in Reutlingen, Germany, can be used to pattern silicon based materials. DRIE is a two-step process consisting of an etching and a passivation cycle. In the etching cycle, silicon is removed using  $\text{SF}_6$  and in the passivation cycle,  $\text{C}_4\text{F}_8$  is used to produce a very thin layer of fluorocarbon polymer to passivate the side walls. In the following etch cycle the polymer film at the bottom of the trench is removed by ion bombardment, while the side walls are protected by the polymer film. The two step process is repeated until the desired depth is attained. With DRIE, microfeatures with high aspect ratios can be fabricated. Bulk and surface micromachining are limited to high stiffness semiconductor materials with Young's modulus  $\sim 100$  GPa [7]. The stiffness of the material is important as it affects the forces generated by the micro actuators. Furthermore, for active devices requiring multiple layers of

materials, adhesion between layers is of great concern. For bulk micromachining, complicated wafer bonding techniques are required to produce multilayer structures. For surface micromachining, thermal stress between layers limits the total thickness to  $\sim 20 \mu\text{m}$  [8]. Bulk and surface micromachining require clean room environment and fine control of process conditions in order to realize devices with good yields.

Micromolding is suitable for large scale production of polymeric devices. The most common techniques in micromolding are injection molding and compression molding. In injection molding, metal mold inserts are used as a replica master and the molding process is carried out at temperatures above the glass transition temperatures of amorphous thermoplastics such as polymethylmethacrylate (PMMA) and polyamide. Compression molding or hot embossing is a technique where the desired structure is pressed under vacuum into a semi-finished polymer material at an elevated temperature above the glass transition temperature. LIGA (lithographie galvanofornung abformtechnik) is a fabrication technique involving X-Ray lithography, electroforming, and a micromolding process [9]. Metal or plastic microstructures with straight sidewall and high aspect ratio (over 100:1) can be fabricated using LIGA.

Soft lithography is gaining popularity as an alternative to photolithography and is useful for prototyping of devices useful for applications in life sciences research. In soft lithography, a topologically patterned stamp (or mold) is used to transfer a pattern to a substrate [10]. There are two types of soft lithography [10]: 1) the replication of a pattern defined in a soft (elastomeric) stamp into organic material or onto the surface of metals, ceramics etc. 2) replication of a pattern defined in a hard stamp into a thin layer of soft organic molecules (e.g. thermoplastic polymers). The second type of soft lithography has been widely used in recent times to fabricate

microfluidic devices with SU-8 structures on silicon wafer as a mold and polydimethylsiloxane (PDMS) as the soft structural material for the device.

Soft lithography provides researchers with rapid prototyping from design to prototype in 24-48 hours using equipment found in most scientific laboratories. The tolerant process conditions of soft lithography permits the devices to be produced in ambient laboratory conditions without a need for clean room environment. The capabilities of soft lithography are compatible with requirement of devices in biology and biochemistry. It is easier to produce multi layered devices with soft lithography when compared to conventional micromachining. Furthermore, since the multilayer devices produced by soft lithography are monolithic, thermal stresses are avoided and interlayer adhesion failures are reduced.

### **1.2.1 Fabrication Materials for Microfluidic Devices**

Microfluidic devices have been fabricated from various materials which include silicon, glass, ceramic, hard plastics and elastomers. In recent years, ever since Whitesides' group introduced the soft-lithography technique [11], PDMS casting on SU-8 mold has been extensively used in various microfluidic research activities. There has been an increasing interest in rapidly prototyping microfluidic systems in PDMS as an alternative to glass and silicon based systems. PDMS micro-molding techniques have been used to fabricate microfluidic systems by many groups [12-15]. PDMS is a low-cost material when compared to traditional micro-fabrication materials, such as silicon and glass. A major advantage of PDMS is that once a master mold is fabricated, multiple devices can be rapidly cast without the need for a clean room environment. PDMS processes are simple and rapid when compared to traditional etching and bonding approaches. The patterned PDMS layers can be stacked to make multilayered device structures.

PDMS rapid prototyping enables device design modifications and optimization to be completed in a shorter time with minimum cost. PDMS is self-releasing and leaves very little residue on a mold, thus allowing the mold to be reused for a long time.

Some of the other advantages of PDMS include:

1. Excellent optical properties (with transparency down to 280 nm) for optical detection schemes.
2. It can be thermally cured at low temperatures (at room temperature in 24 hours and at 80°C in 2 hours).
3. Features on the micron scale can be reproduced with high resolution.
4. Non-toxic and biocompatible.
5. Its surface properties can be easily modified to be hydrophobic or hydrophilic by well-established surface treatment protocols.
6. Its elastic properties can be easily altered by changing the mixing ratios of the base and curing agent of the pre-polymer.

SYLGARD 184 Silicone Elastomer Kit (Dow Corning, Midland, MI) is widely used to prepare PDMS. The SYLGARD 184 PDMS kit consists of a curing agent and prepolymer which can be mixed in a 1:10 ratio and thermally cured to obtain PDMS. Traditionally, thick ( $> 100 \mu\text{m}$ ) and high aspect ratio microstructures have been fabricated using LIGA [16], microstereolithography [17] and DRIE [18] processes. These techniques require complex and expensive equipment that are not readily accessible to small scale laboratory facilities. The application of SU-8 (MicroChem Corp., Newton, MA) to fabricate thick microstructures for MEMS applications has attracted lot of interest [19] in the recent years. SU-8 is a high contrast, negative, epoxy-based line of near-ultraviolet (UV) radiation-sensitive photoresists with suitable chemical and

mechanical properties that can be used to fabricate high aspect ratio microstructures with near-vertical side walls in a single photolithographic step [19]. A developed SU-8 structures is thermally (up to 200 °C) and chemically stable, making them well suited for fabricating permanent structures such as pixel walls, fluidic channels, nozzles, micro arrays and spacers.

### **1.3 Miniaturization of Diagnostic Assays**

A wide variety of classical, macroscopic liquid handling systems for performing analytical and diagnostic assays have been in use for many decades. Miniaturization of the macroscopic liquid handling system has become a popular trend in the last few decades and has led to a new class of microanalyzers. The common feature of all these devices is the miniaturization of an analytical process or part of the analytical process into a device built on a small substrate of glass, plastic or silicon.

There are several compelling reasons for the miniaturization of analyzers. The scaling effects due to decreased length scales allow for new applications that are not achievable in macroscopic liquid handling systems. Miniaturization makes the analytical processes cost effective by reducing the volume of reagents used per assay (in the order of nano to pico liter) when compared to the traditional analysis. In case of drug discovery applications, where there is a limited amount of drug compound to be tested, a reduction in the volume of the reagents, allows more tests to be performed on that drug compound. The reduction in footprint of each individual test enables a higher degree of parallelization within a small space. A key example is parallel reactions in hundreds of thousands of individual wells with picoliter volumes and minimum reagent consumption for genome sequencing [20]. The chemical reaction rate is high and the response time of the device is fast due to the small scale of the devices and smaller volumes of

the samples. Due to decreasing length scales, surface phenomenon such as capillary forces and surface charges in miniaturized devices becomes dominant. This permits purely passive liquid actuation based on capillary forces in the lateral flow assays also known as capillary test strips. Another outcome is the onset of a laminar flow at low Reynolds number in small channels. This enables the creation of well-defined and stable liquid-liquid interfaces. The use of multiple laminar streams in a microfluidic channel to deliver membrane permeable molecules to selected subcellular microdomains has been reported [21]. Another important advantage of miniaturization is the ability to integrate all the steps of a multi-step analytical process on to a single device. It is possible to design a microsystem which can be used to perform different tasks like sample addition, processing and analysis, all on a microchip that is  $2\text{ cm} \times 2\text{ cm}$  or smaller [22]. This concept is very similar to the integrated electronic circuits, where millions of individual components are integrated into a single chip. Some of the other helpful properties of small assay volumes are fast thermal reaction and low power consumption for liquid manipulation and thermal control [23]. This can speed up assays such as PCR that require a thermocycling step. However, miniaturization has some disadvantages. The small size of the microchip can make their handling difficult. This can only be overcome by packaging the microchip into a larger holder or by mounting the microchip onto a platform. A drastic reduction in the sample size can sometimes make the sample a bad representative of the specimen such as non-homogenous biological specimens that contain a diversity of constituents like cells, proteins, etc. This problem can be overcome by developing flow-through sampling in which large volumes of the sample are transported through a low volume microanalyzer. Another problem associated with sample volume reduction is the detection limit. If the concentration of the analyte

is low in the specimen, a volume reduction can decrease the quantity of the analyte detectable by the microanalyzer.

## 1.4 Microfluidic System Designs

A microfluidic system provides a set of fluidic unit operations, which provide a generic and consistent way for miniaturization, integration, automation and parallelization of (bio-) chemical processes [23]. Microfluidic systems can be broadly classified according to the main liquid propulsion principle as shown in Figure 1.1.

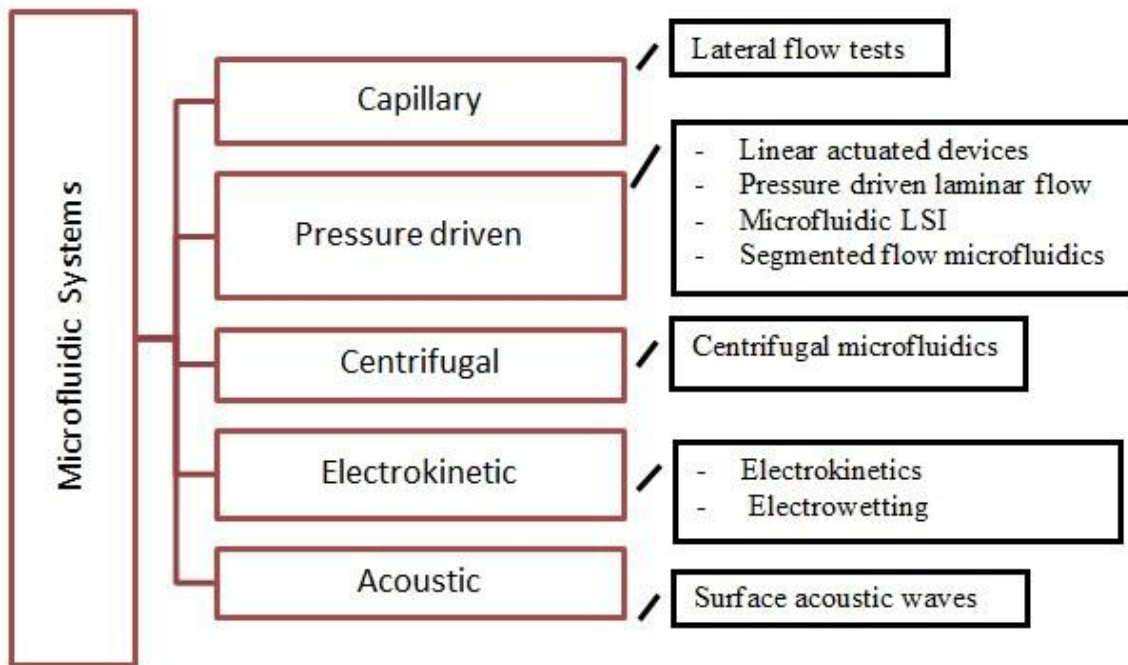


Figure 1.1 Microfluidic systems classified according to their main liquid propulsion principle

### 1.4.1 Capillary

Lateral flow (LF) tests are commonly known as test strips where the sample liquids are driven by capillary forces. The liquid flow is controlled by the wettability and feature size of the



microstructured substrate. All the required chemicals are pre-stored within the test strip. The test results are optical signals and are usually implemented as a color change in the detection area that is visible to the naked eye.

#### **1.4.2 Pressure Driven**

In linear actuated devices (LAD), liquid movement is controlled by mechanical displacements of a plunger. Liquid flow is usually restricted to a single direction without any branches or alternate flow pathways. In these devices, the calibration liquids and buffers are usually pre-stored in pouches. A pressure driven laminar flow (PDLF) system is characterized by a liquid transport due to pressure gradients. Typically, this creates stable laminar flow profiles within the microchannels. There are a wide range of external and internal pressure sources such as syringe, pumps or micropumps, gas expansion principles, and pneumatic displacement of a flexible membrane that can be used to implement a PDLF. A pressure driven microfluidic system has been implemented in the present study.

The samples and reagents are usually injected into the chip inlets, either in a batch or a continuous mode. PDLF offers predictable velocity profiles and controllable diffusion mixing. Microfluidic large scale integration (MLSI) describes a microfluidic channel circuitry with chip-integrated microvalves based on flexible membranes between a liquid-guiding layer and a pneumatic control-channel layer. The microvalves open and close according to the pneumatic pressure applied to the control-channels. Complex units such as micropumps, mixers, and multiplexers can be designed by combining several microvalves on one single chip. The MLSI platform developed in 1993 [24] when combined with soft lithography techniques enabled the monolithic fabrication of all necessary fluidic components within one single elastomer material

such as PDMS. Segmented flow microfluidics (SFM) transport small liquid plugs and/or droplets immersed in a secondary immiscible continuous phase (gas or liquid) within closed microfluidic channels [23]. The plugs/droplets are typically in the picoliter to microliter volume range and can be transported by pressure gradients generated by external pressure sources. The plugs/droplets can be merged, split, sorted, and processed.

### **1.4.3 Other Systems**

In centrifugal microfluidics (CM), all processes are controlled by the frequency protocol of a rotating microstructured substrate [23]. The forces involved in the liquid transport include centrifugal force, Euler force, Coriolis force and capillary force. All the assays are implemented as a sequence of liquid operations in a radially inward to outward direction. In electrokinetic (EK) system, microfluidic operations are performed by electric fields acting on electric charges or electric field gradients acting on electric dipoles [23]. Several EK effects such as electroosmosis (EO), electrophoresis (EP), dielectrophoresis (DEP) and polarization can be superimposed on each other. EO can be used to transport bulk liquid, while other effects can be used to separate different types of molecules within the bulk liquid. Electrowetting (EW) systems use droplets on a hydrophobic surface that contain one- or two- dimensional array of individually addressable electrodes. The droplets can be generated, transported, split, merged and processed by changing the voltage between neighboring electrodes. The surface acoustic wave (SAW) system uses droplets residing on a hydrophobic solid support in a gaseous environment (air) and the microfluidic unit operations are mainly controlled by acoustic shock waves travelling on the surface of the solid support [23]. The shock waves are generated by a piezoelectric transducer (PZT) chip consisting of interdigitated electrodes (IDE) placed on top of a piezoelectric layer.

## 1.5 Biosensing

Microorganisms such as bacteria and virus are an integral part of life on earth. Some of these microorganisms are pathogenic in nature and can cause disastrous effects on human health. The detection of pathogenic bacteria and viruses is a key to the prevention and identification of many health problems. Similarly, the ability to detect physiologically significant biomolecules in the body with high sensitivity and specificity offers a powerful prospect in early diagnosis and treatment of diseases. Early detection and diagnosis can significantly reduce the cost of patient care associated with advanced stages of many diseases. Figure 1.2 [25] shows that the food industry [26-27] water and environment quality control [28-29] and clinical diagnosis [30] constitute over two thirds of all research activities. The food industry dominates the need for pathogen detection. There are tough legislations in the food industry, where a failure to detect a contamination can lead to widespread public health damages. More than 200 known diseases are transmitted through food [31] and the symptoms of foodborne illnesses range from mild gastroenteritis to life-threatening neurologic, hepatic, and renal syndromes. It has been reported [32] that foodborne diseases cause approximately 76 million illnesses, 325,000 hospitalizations, and 5,000 deaths in the United States each year. The USDA estimates that \$2.9 - \$6.7 billion is lost annually due to medical costs and loss in productivity caused by major foodborne pathogens [33].

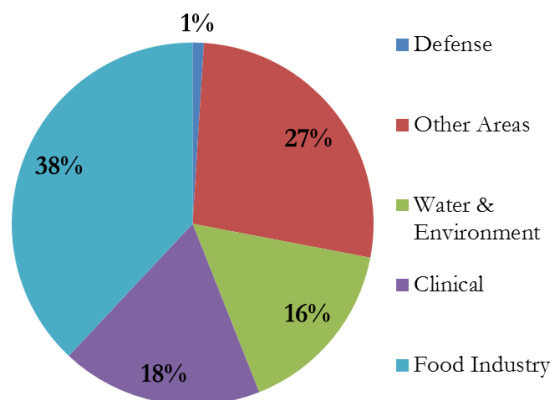


Figure 1.2 Distribution, by industry of application, of the relative number of works appeared in the literature on detection of pathogenic bacteria

The cost for patient care at advanced stages has been estimated to be \$75 billion [34] and \$90 billion [35] for cancer and diabetes, respectively. At present, cancer detection can be done by monitoring the concentration of certain antigens present in the bloodstream or other bodily fluids, or through tissue examinations. Diabetes is monitored by determining the glucose concentrations in the blood over time. But despite their widespread clinical use, these diagnostic techniques have a number of limitations. In order to diagnose and monitor various diseases in a patient, it is a common practice to examine blood/urine samples and perform various biochemical tests on the samples. Most clinical diagnostic applications have focused on the detection of biomolecules as early indicators of diseases but can also include monitoring of regular metabolic parameters such as glucose and lactate [36]. These tests require specific analytical techniques, as well as skilled personnel to collect the desired samples from the patient and perform the tests.

## 1.6 Pathogens and Biomolecules

Biosensors can detect pathogens such as bacteria, viruses or a range of biomolecules such as proteins, enzymes, DNA and RNA for clinical diagnostics. Foodborne illnesses can be caused by pathogens such as bacteria, viruses, parasites, toxins and prions [32]. The four major foodborne bacteria are *Salmonella*, *Listeria monocytogenes*, *Campylobacter* and *Escherichia coli* (*E. coli*) O157:H7. Viral infections can present generic symptoms and can be difficult to diagnose. A biosensor would allow a physician to determine the specific virus quickly and prescribe appropriate treatment. Viruses are capable of spreading rapidly by natural means and their ability to mutate quickly makes their detection a challenging task. In recent times, the emergence of avian influenza (AI) with pandemic potential has made the rapid screening of AI virus strains crucial in controlling worldwide outbreaks. Some of the other viruses of interest include dengue virus [37] rabies virus [38], human immunodeficiency virus (HIV) [39] and Adenovirus [40]. The rapid and quantitative detection of biomolecules such as protein biomarkers and nucleic acids is important for both clinical diagnostics and drug discovery applications. Early detection is particularly important in cases such as cancer, because the detection of the early stages of a disease can enable a greater probability of a successful treatment.

### 1.6.1 Bacteria and Viruses

Among the various types of bacteria, the most economically significant [41] infections are caused by *E. coli* O157:H7. Although most strains are harmless and some even live in the intestines of healthy humans and animals, the O157:H7 strain produces a potent toxin and can cause severe illness. Typical symptoms include abdominal cramping, diarrhea and bloody stools. Occasionally this infection results in kidney failure. There have been many instances of meat

recalls in the past. For example, in 2003, Howard Beef Processors in Minnesota voluntarily recalled approximately 194,700 pounds of frozen ground beef products. Recalls of this kind can be avoided if the bacteria are detected in advance before the meat reaches the market.

Among the various types of viruses, avian influenza (AI) virus has raised concerns about a potential pandemic. AI viruses are classified into sub-types based on antigenic differences of the surface glycoproteins, namely Hemagglutinin (HA) and neuraminidase (NA). To date, sixteen HA (H1 through H16) and nine NA (N1 through N9) subtypes have been identified [42]. AI viruses are usually found in wild birds but can also infect people, pigs, horses and other animals. In Asia and Europe [43], numerous outbreaks of AI virus have been reported in recent years. The economic significance of AI is substantial. According to CDC [44], the direct economic loss could be up to hundreds of billion dollars.

### **1.6.2 Insulin**

Insulin is a hormone responsible for glucose metabolism. Insulin is produced in the pancreas within the  $\beta$ -cells of the islets of Langerhans. Diabetes mellitus (DM) is a disease where the patient has difficulties in maintaining normal blood glucose levels. DM is mainly caused when insufficient insulin is produced by the  $\beta$ -cells in the pancreas, or the patient's body is unable to effectively utilize the insulin produced. The presence of high blood glucose levels in a patient can induce secondary complications such as nephropathy and retinopathy. The presence of low blood glucose levels is known as hypoglycemia which can lead to insulin shock as well as death.

There are three main types of DM, namely, type I (insulin dependent), type II (non-insulin dependent) and Gestational DM [45]. Type I DM is caused by an auto-immune reaction where the body's defense system attacks the insulin-producing cells. Patients with type 1 DM produce

very little or no insulin. Type I DM can affect people of any age, but mostly occurs in children or young adults. Type II DM accounts for at least 90% of all cases of diabetes and is characterized by insulin resistance and relative insulin deficiency. The occurrence of type II DM is typically seen in patients over the age of 40 but can occur earlier, especially in populations with high diabetes prevalence [45]. Gestational DM is a type of diabetes that causes high blood glucose levels in a patient during pregnancy. It develops in one in 25 pregnancies worldwide [45]. Gestational DM usually disappears after pregnancy, but patients and their offspring are at an increased risk of developing type II DM later in life. Diabetes is a chronic disease and has reached epidemic proportions in recent years. The prevalence of diabetes for all age groups worldwide by the year 2030 has been estimated to be 7.8% by the International Diabetes Federation [46]. The total number of people with diabetes is projected to rise from 171 million in 2000 to 439 million by 2030 [46].

Insulin monitoring is very important for clinical diagnosis of DM and several analytical methods have been devised for insulin detection. Some of these analytical methods reported include immunoaffinity chromatography with subsequent liquid chromatography/mass spectrometry analysis [47] immunoassays [48], imaging ellipsometry [49], electrochemical [50], amperometric [51], surface plasmon resonance [52] and mass-sensitive biosensors [53]. The efficiency of biochemical tests for disease diagnosis is determined by its sensitivity, specificity and time taken for obtaining the test results. There is a large demand for the development of inexpensive and easy to perform clinical diagnostic methods, which can provide fast and reliable measurements of the metabolic parameters of a human body with minimum invasion.

Type II DM has been observed [54] to be a progressive disease with the reduction in the pancreatic  $\beta$ -cell function commencing 10-12 years before diagnosis. By the time most patients

are diagnosed with type II DM, their pancreatic  $\beta$ -cell function may have deteriorated up to 50%. The reduction in  $\beta$ -cell function can lead to insulin deficiency and monitoring the insulin level can be highly useful to predict the occurrence of type II DM in a patient. The current methods for insulin detection are based on large automated immunoassay analyzers. These large analyzers are expensive and are not suitable for point-of-care-testing in a physician's office.

### 1.7 Conventional Biodetection Methods

The conventional biosensing techniques are listed in Figure 1.3. Morphological methods are performed by using microscopic techniques such as bright field, scanning electron microscopy (SEM) and atomic force microscopy (AFM). Morphological methods are more suitable for qualitative analysis than quantitative analysis. The sample preparation steps can be time consuming and in some cases, the sample preparation method can alter the morphology of the sample being investigated.

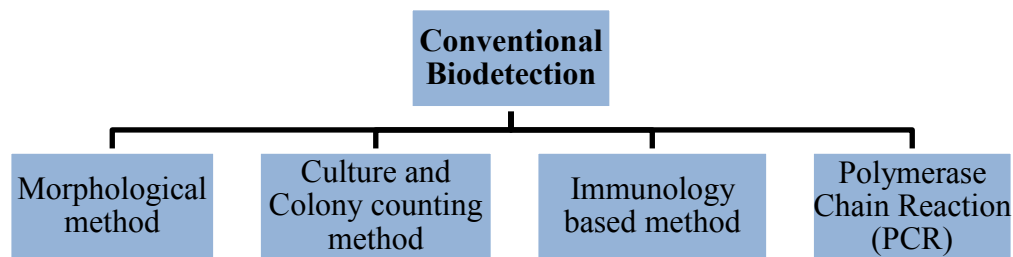


Figure 1.3 Conventional biodetection methods

Culturing and colony counting (CCC) method is performed by growing and multiplying the pathogens in a culture media such as agar under controlled laboratory conditions. CCC methods used for bacterial detection are cumbersome and time consuming, typically require weeks to complete, involving sequential steps for pre-enrichment, selective enrichment, selective plating



and subsequent biochemical and serological confirmation [55]. Immunology based methods involve antigen-antibody reactions. Examples of immunology based methods include enzyme immunoassay (EIA) [56], enzyme linked immunosorbent assay (ELISA) [57], enzyme-linked immunomagnetic chemiluminescence (ELIMCL) [58], immunomagnetic separation [59], immune-precipitation assay [60] and western blot test [61]. Some of the problems associated with immunology based methods are low sensitivity of the assays, low affinity of the antibody to the analyte/pathogen being measured, and potential interference from contaminants [62]. Polymerase Chain Reaction (PCR) is a nucleic acid amplification technology that was developed in the mid-80s [63]. It is based on the isolation, amplification and quantification of a short DNA sequence including the targeted pathogen's genetic material. A target DNA can be amplified 1-million-folds in less than an hour, with sensitivities in theory down to a single target pathogen [64] and is therefore a widely used detection method for pathogens in food. The PCR method is less time-consuming than techniques such as like culturing and plating. PCR can take anywhere from 5 to 24 h to produce a detection result depending on the type of PCR variation used and this time frame does not include any previous enrichment steps. A false negative PCR test result can occur due to interference with target-cell lysis necessary for nucleic acid extraction, nucleic acid degradation and/or direct inhibition of the PCR. The disadvantage of PCR based methods is that it is expensive, complicated and required highly skilled workers to carry out the tests.

### **1.7.1 Limitations of Conventional Biodetection Methods**

In order to prevent the spreading of diseases, prevent a pandemic and obtain important epidemiological information about any pathogen outbreaks, the industry needs a reliable, specific, sensitive, and rapid method for biodetection. The earlier the pathogen outbreak is detected the easier it is to prevent a pandemic by adopting appropriate confinement strategies.

The earlier the symptoms of a disease such as cancer/ diabetes are detected through clinical diagnostics, the better are the chances of a successful treatment. Most of the conventional methods are effective but are time consuming and required highly skilled professional to perform them. Also, the test sample needs to be transported to dedicated laboratories where these tests are performed. There is a need for a technology that can enable rapid, reliable, simple and sensitive detection. In addition, it should be capable of in-situ real-time monitoring at a low cost. In recent years, there has been much research activity in the area of biosensor development for detecting pathogens and physiologically relevant biomolecules. Biosensors are expected to address the limitations of traditional methods by enabling much faster detection schemes.

## **1.8 Biosensor**

A biosensor is a sensing device comprising of a bio-recognition element and a transducer. A bio-recognition element specifically identifies and interacts with an analyte and the changes in its physicochemical properties (optical, thermal, electrical and thermodynamic properties) are usually converted into an electrical signal by a transducer. Figure 1.4 shows the schematic of a biosensor. The bio-recognition element is a sensing material and may include enzyme, antibodies, microorganism, tissues, organelles and DNA/RNA [65]. The biosensors can be classified based on the type of bio-recognition element or the transducing method used. Based on the bio-recognition element, the biosensors can be classified as enzyme sensors, immunosensors, nucleic acid probe sensors, cell-, tissue- and organelle based sensor. Based on the transducing method, biosensors can be classified as piezoelectric biosensor, optical biosensor and electrochemical biosensor.

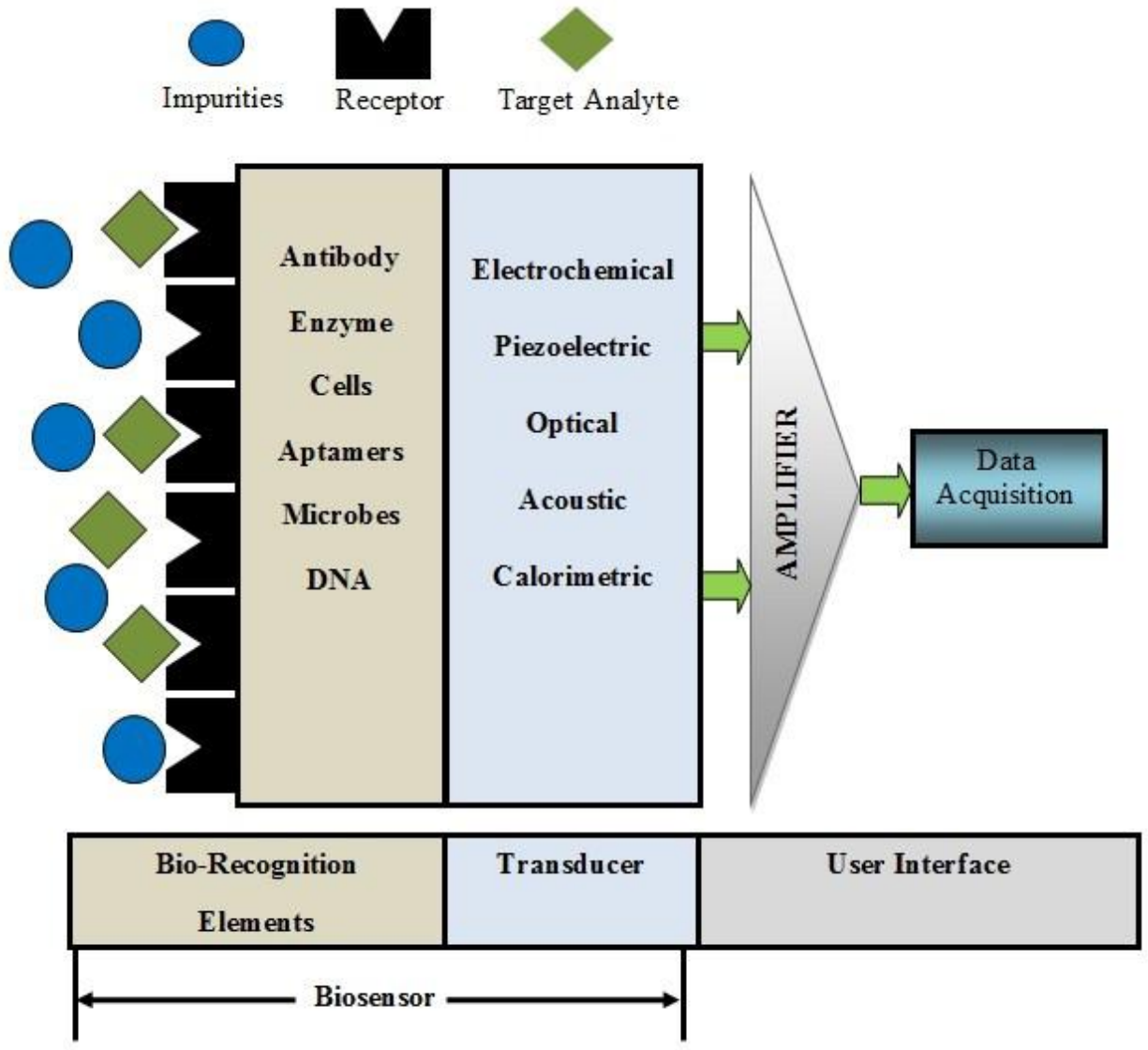


Figure 1.4 Schematic of a biosensor

### 1.8.1 Bio-Recognition Element

Antibody based sensors, also known as immunosensors, are based on the specificity of antibody-antigen reaction to produce a change in the transducer signal. Both polyclonal and monoclonal antibodies can be used and the suitability depends mainly on their specificity. Antibodies can be directly immobilized on the surface of the transducer by covalent bonding through amino, carboxyl or aldehyde groups. Antibodies can also be attached to the surface of magnetic beads to

perform immunomagnetic separation and detection. Antibody based biosensors with various transducing methods have been previously reported. For example, immunosensors have been designed for monitoring cancer cells [66], for cancer marker cell detection [67], for bacteria and virus determination assays [68], for toxins [69], etc. Enzyme based biosensors are based on using enzymes which are specific to the biomolecules under detection to catalyze the generation of a product which can be quantified by a transducer. Most of the enzymes used in biosensors are oxidases that react with dissolved oxygen to produce hydrogen peroxide. For example, oxidoreductase enzymes have been used for the detection of lactate [70], alcohol [71], cholesterol [72], etc. Nucleic acid based biosensors integrate a natural and biomimetic form of oligo- and polynucleotides and rely on the very strong base pair affinity between complementary sections of nucleotide strands for their high sensitivity and selectivity. In recent years, the use of synthetic oligodeoxyribonucleotides (ODNs) is gaining popularity. End-labels, such as thiols, disulfides, amines, or biotin, are incorporated to immobilize ODNs to the surface of a transducer element. Electrochemical DNA biosensors where the base-pair recognition event is converted into a measurable electrical signal are being used for the diagnosis of genetic diseases, pathogens, biomolecules of clinical interest, etc. [73] reported a low-density electrical 16S rRNA specific oligonucleotide microarray for detecting pathogens such as *E. coli*, *Pseudomonas aeruginosa*, *Enterococcus faecalis*, *Staphylococcus aureus*, and *Staphylococcus epidermidis*.

### **1.8.2 Transducer element**

Optical biosensors include surface plasma resonance (SPR) biosensor, adsorption and reflection biosensor, luminescence biosensor, fluorescence biosensor and optical fiber biosensor. SPR and fluorescence biosensors are the most popular optical biosensors. Fluorescence biosensors use fluorescent labels for signal generation and the intensity of the fluorescent signal is used to

determine the amount of the antigen being detected [74]. SPR is a direct optical-sensing technique that measures the refractive index change due to bio-specific interactions occurring in the vicinity of a thin metal film surface [75]. SPR biosensors for detecting influenza virus [76] and plant virus [77] have been reported. Piezoelectric biosensors consist of mass-sensitive piezoelectric crystals with excitation electrodes. The piezoelectric transducers allow a binding event to be converted into a measurable signal, such as resonant frequency changes [78]. The most popular transducer design is based on the quartz crystal microbalance (QCM), adapted to the liquid medium, which gives a direct response signal to characterize the binding event between a sensitive layer grafted onto the surface transducer and the analyte to be detected [78]. QCM has been used for the detection of DNA, protein–ligand interactions, virus capsids, bacteria, and mammalian cells [79]. A microcantilever is another type of mass-sensitive biosensor. The principle of this detection is based on the change in the mechanical response of a cantilever due to molecular adsorption on the functionalized cantilever surface. The sensitivity of a microcantilever is high enough to detect a single virus particle [80]. Electrochemical biosensors can be classified into amperometric, potentiometric and impedance biosensors based on the electrical parameters they measure. Potentiometric biosensors use ion-selective electrodes (ISE) and ISFET to measure the change in electric potential due to the accumulation of ions resulting from an enzyme reaction [81]. Amperometric biosensors measure the change in electrical current (typically in the nA to  $\mu$ A range) due to the oxidation/reduction process of an electroactive species. The working electrodes are usually a noble metal or a screen-printed layer covered by a bio-recognition element [82]. The amperometric biosensors are often used for analytes such as glucose, lactate [83], and sialic acid [84]. In addition, the detection of biological agents such as *Bacillus cereus* and *Mycobacterium smegmatis* [85], the serological diagnosis of

Francisellatularensis [86], pesticides and nerve agents [87] have been reported. Potentiometric biosensors measure the potential difference generated across an ion-selective membrane separating two solutions at virtually zero current flow. A potentiometric sensor array [88] for investigating the cytotoxicity of hydroquinone to cultured mammalian V79 cells has been reported. Impedance biosensors are based on the combined measurement of the resistive and capacitive properties of the targets in response to a small amplitude sinusoidal excitation signal [89-90]. Impedance detection involves measuring the change in impedance caused by the binding of analytes to receptors (antibodies, DNA, proteins etc.) immobilized on the surface of electrodes [91-93], change in the conductivity of the medium caused by the growth of bacteria [94-96], bacterial cells captured on an electrode surface using Dielectrophoresis [97-100], and change in the ionic concentration of a medium caused by activity of enzyme used as labels [101-104]. Calorimetric biosensors are based on measuring the heat of a biochemical reaction at the sensing element. These biosensors consist of temperature sensors with immobilized biomolecules. Once the analyte comes into contact with the biomolecules, the reaction temperature is measured. The total heat produced or absorbed is proportional to the molar enthalpy and the total number of molecules in the reaction. The change in temperature is proportional to the analyte concentration. Calorimetric biosensors have been used for food, cosmetics, pharmaceutical and other analysis. For example, a microcalorimetric sensor has been used for L-malic acid determination [105] in various types of food.

## **1.9 Immunoassay**

Immunoassay is a technique that exploits the sensitivity and specificity of antibody-antigen interactions for the detection of relevant analytes [106]. Immunoassays are routinely used for the quantification of proteins and small molecules in medical diagnostics, proteomics,

pharmaceutical and biological research [106]. Immunoassays can be broadly classified into homogenous and heterogenous immunoassay. In homogenous immunoassays, antibodies and antigens interact within a solution. In heterogeneous immunoassays, antibodies are immobilized on a solid support and interact with the antigen at the boundary layer. For example, the antibodies can be immobilized on the surface of micro and nano beads. The micro and nano beads can be either paramagnetic or non-magnetic.

### **1.9.1 Pretreatment of Biological Samples**

A sample pretreatment and enrichment step is necessary for detecting biological samples at very low concentrations. A generic analytical procedure [107] can be broken down into three broad categories as shown in Figure 1.5: the *analytical principle* on which the measurement is based, the *analytical method* which is the concept for optimizing the conditions of the analytical principle chosen, and the *analytical procedure* which includes all considerations from the analyte to the analytical result. It is necessary to pretreat raw biological samples (from body, laboratory or field) to ensure that the analyte to be detected is present in a form compatible with the measurement process and also be free of any foreign substance that may interfere with the accuracy of measurement. In a traditional sample pretreatment process, several steps that require the use of large-scale equipment such as high-speed centrifuge and shaker are involved.

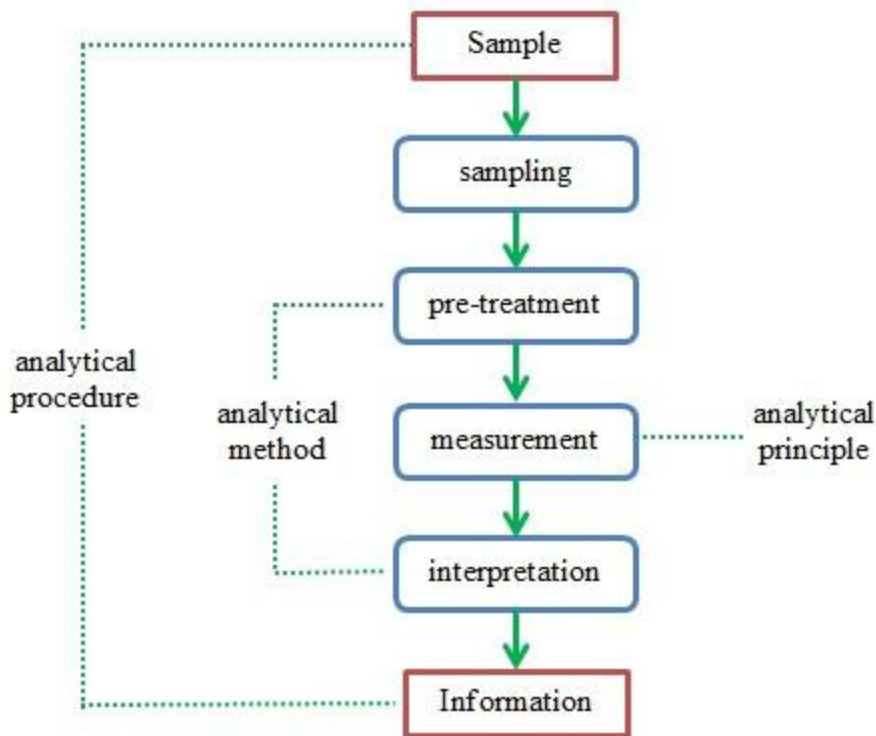


Figure 1.5 Schematic of a general analytical process

### 1.9.2 Micro/Nano Magnetic Bead Immunoassay

Microbeads are widely used due to their high surface area to volume ratio and ability to function as a simple mechanism of delivering antibodies to desirable locations within the microfluidic device [108]. Microbeads can be either magnetic or non-magnetic. For non-magnetic beads, they can be physically retained by dam-like microstructures [109] to facilitate the removal of unbound analytes. Alternatively, this can be achieved through the use of dielectrophoresis [110] or electrostatic forces [111]. The use of magnetic beads eliminates the need for retention microstructures. In magnetic bead based immunoassays, antibody coated magnetic beads can be immobilized on the device surface [112] or on the sensor surface [113]. The manipulations of magnetic beads can be accomplished in two ways: (1) by placing a permanent or electro magnet



outside the device, and (2) by fabricating the magnet inside the device. Approach (1) has the advantage of ease of fabrication and low cost. Approach (2) allows a more precise control of the field strength and direct contact with the magnetic beads.

### **1.9.3 Immunomagnetic Separation**

In recent years, the use of micro or nano superparamagnetic (SPM) beads in immunological assays has increased as the magnetic properties are shown to improve the assay sensitivity and duration [114]. In a magnetic immunoassay, the SPM beads are coupled with the target analyte using various immobilization techniques. One of these techniques is the antibody-antigen complex. The various steps of an immunomagnetic separation technique are illustrated in Figure 1.6. In this process, the SPM beads are first activated with functional groups that can bind to an antibody (Ab) specific to the target analyte. Upon mixing with the test sample containing the analyte, the Ab-SPM beads complex selectively capture the target analyte. The use of Ab-SPM complex provides a more efficient interaction between the capture Ab and the target analyte, when compared to Ab immobilized on the bottom of a microwell. The Ab-SPM particle complex with captured target is then magnetically separated by subjecting the test sample to a magnetic field. Magnetic separation techniques have much higher separation efficiency when compared to centrifugation [114].

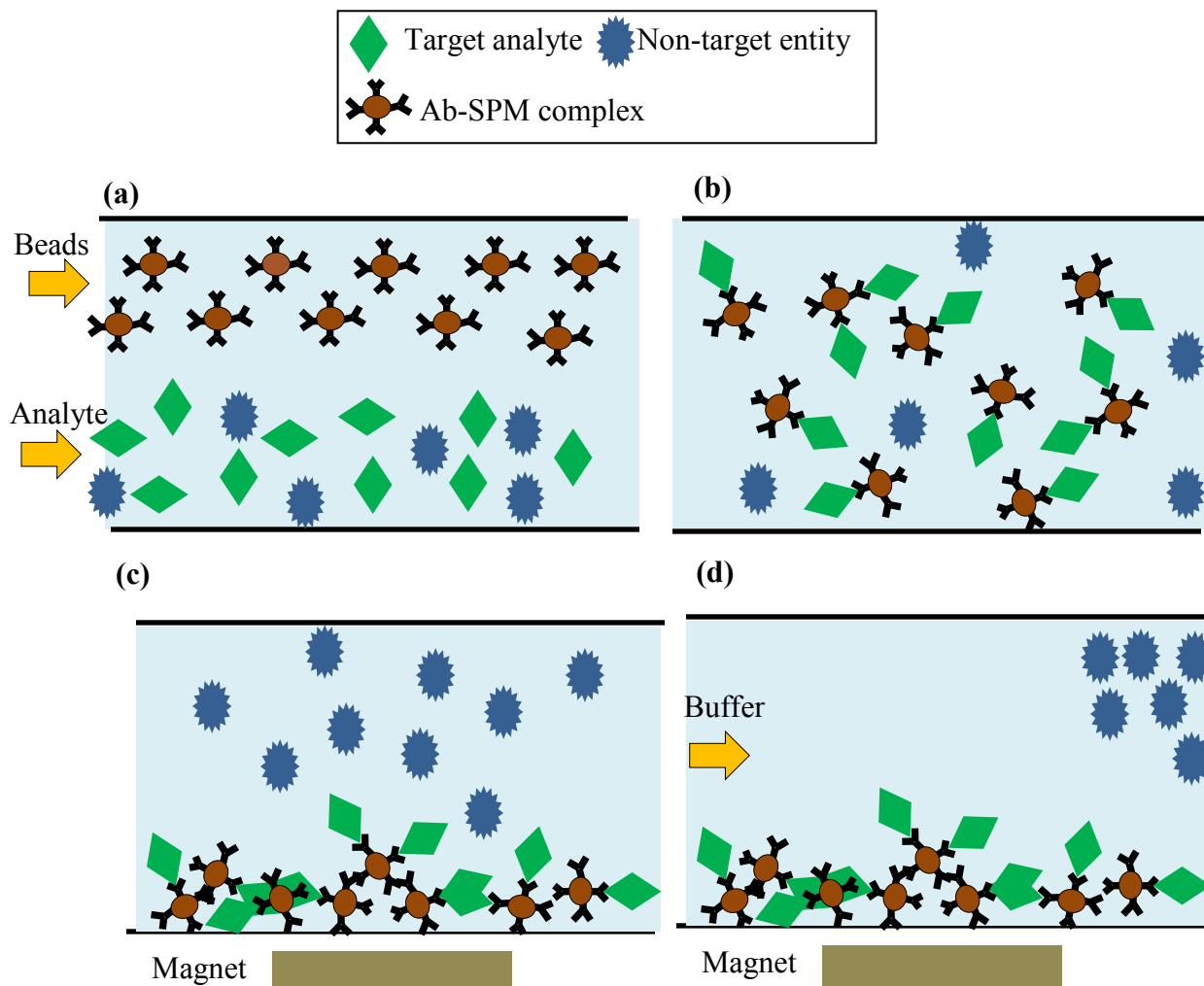


Figure 1.6 Basic steps of immunomagnetic separation (a) Introduction of the beads and the analyte mixture, (b) mixing and binding of the target analyte to Ab-SPM complex (c) magnetic separation of the Ab-SPM complex and target analyte conjugate, (d) washing of the non-target entities and background fluid by buffer

### 1.10 Micro Total Analysis System

In 1990, a new paradigm of integrated microfluidic devices, the concept of miniaturized total chemical analysis system (TAS) or  $\mu$ TAS was proposed by [115] in which silicon chip analyzers incorporating sample pretreatment, separation and detection were the key features. Figure 1.7 lists the various components of a  $\mu$ TAS which can be integrated on a single system to automate various analytical methods. The standard operation of a  $\mu$ TAS includes sample preparation,

sample injection, fluid and particle handling, reactors and mixing, separation and detection [116]. A fully integrated microfluidic system can be designed to perform all the standard operations of a  $\mu$ TAS. For example, a cell sample pretreatment step can be performed by micromixing the cells with fluorescent dyes. These fluorescent labeled cells can then be sorted and transported to subsequent components for further post-processing steps such as sorting and optical detection. All the operations of a  $\mu$ TAS are analogous to those performed in a conventional laboratory using the traditional equipment. A  $\mu$ TAS has the potential to replace the traditional, complicated biodetection systems and save time and labor.

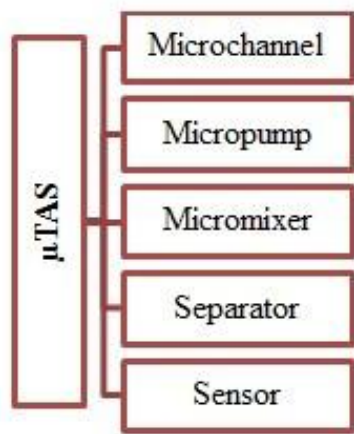


Figure 1.7 Components of a  $\mu$ TAS

The following sections provide a brief description of the various components of a  $\mu$ TAS.

### 1.10.1 Microchannels

Microchannels and reservoirs are passive components used to transport and confine microscale fluids. Microchannels can be defined as channels whose dimensions are less than 1 mm and greater than 1  $\mu$ m. Currently, most microchannels fall into the range of 10 to 100  $\mu$ m. Microchannels can be fabricated on a wide variety of substrate materials such as glass, polymers

and silicon. The choice of the material and fabrication methods depend on various factors like device yield, processing cost, the compatibility between the channel material and the fluid to be transported (hydrophobic, hydrophilic, chemical resistance, biocompatibility), geometry constraints like depth, width, surface roughness of the channel surface, and optical transparency requirements.

### **1.10.2 Micropump**

A micropump is an essential component of a  $\mu$ TAS and delivers fluid between different components in a controlled manner. Micropumps can be classified into two main categories: mechanical micropumps and non-mechanical micropumps. Mechanical micropumps can be further classified into two categories: dynamic pumps and displacement pumps [117]. Dynamic pumps add energy to the working fluid directly to increase its momentum. A few dynamic pumps, mostly micro gear pumps, have been reported. For example, a gear micropump fabricated by LIGA [118] and driven by a small electromagnetic motor, has two opposing in-line gears (0.6 mm in diameter) and can provide a maximum flow rate of 180  $\mu$ L/min and a maximum pressure of 100 kPa while operating at 2250 rpm. Dynamic pumps have moving parts and have complicated fabrication process. Dynamic pumps with moving parts such as micro gears can cause damage to bio-samples and are not suitable for biological applications. Displacement pumps operate by exerting pressure on the working fluid through one or more moving boundaries. The majority of micropumps are displacement pumps in which the moving surface is an oscillating diaphragm and also known as diaphragm pumps. Common pump diaphragm materials reported include silicon [119], glass [120], silicone rubber [121], polyimide [122], and PDMS [123]. Different actuating mechanisms have been used to drive the diaphragm including piezoelectric [124], electrostatic [125], thermo-pneumatic [126], pneumatic [127] and

electromagnetic [128]. Flow rates ranging from as low as 0.0006 mL/min [129] to as high as 16 mL/min [130] have been reported with diaphragm pumps. Non-mechanical micropumps convert non-mechanical energy (electrical/magnetic) to kinetic energy to add momentum to the working fluid. Non-mechanical micropumps include electrohydrodynamic (EHD pumps, electroosmotic (EO) pumps, and magnetohydrodynamic (MHD) pumps. EHD pumps [131-133] utilize electrostatic forces acting on dielectric liquids to generate flow. One of the fundamental requirements of EHD pumps is that the fluid must have low electrical conductivity. EO micropumps [134-136] are based on liquid flow generated by the presence of an electric field when an ionic solution is in contact with a charged solid surface. EO pumps have the limitations of high voltage requirement and electrically conductive fluid. MHD pumps are based on Lorentz force as the driving force with interaction of electrically conductive fluids and magnetic field. MHD pumps require working fluids with higher conductivity (greater than 1 S/m) and bubble generation due to ionization is a major drawback.

Micropumps used in  $\mu$ TAS for biomedical applications have requirements such as: biocompatibility, controllable flow rates, smaller footprints and less power consumptions. In general, non-mechanical pumps when compared to mechanical pumps have higher power requirements and limit the electrical properties of the working fluid. Polymer materials such as PDMS and PMMA are being widely used these days due to their biocompatibility and ease of fabrication of multilayer monolithic devices. In pneumatically driven diaphragm micropumps, the choice of the diaphragm material is important and a low-modulus diaphragm material is widely used to achieve maximum diaphragm deflection for a given driving force. It is also an advantage to select a diaphragm material such as PDMS that can be readily integrated into an existing device without affecting the fabrication process. A displacement pump with PDMS as

the structural material, based on moving membranes actuated in a sequence by external pneumatic pressure, can meet most of the requirements of a micropump used in  $\mu$ TAS for biomedical applications.

### **1.10.3 Micromixer**

Micromixer is another important component of a  $\mu$ TAS which often require the mixing of reactants. Mixing at the micro scale is a challenging task because the flow is laminar and mixing is dependent on molecular diffusion. Micromixers can be classified into passive and active devices. Passive micromixers have no moving parts, do not require external energy source and achieve mixing through the topology of the microfluidic device. Different types of passive micromixers have been reported: T-mixers [137], Y-mixer [138], injection micromixer [139], chaotic advection micromixers with obstacles in the fluid path [140], droplet micromixer [141]. Active mixers usually have moving parts and use external energy source to disturb the flow for mixing. Active micromixers are classified based on the type of external disturbance used. Examples of active micromixers include T-mixer with pressure disturbance [142], micromixer with EHD disturbance [150], micromixer with DEP disturbance [151], micromixer with MHD disturbance [145], micromixer with EK disturbance [146], and micromixer with acoustic disturbance [147]. In general, active mixers have higher mixing efficiency [148]. Some of the factors to be considered in selection of the type of micromixer used in a  $\mu$ TAS include the ease of integration with other components, fabrication material used and compatibility of actuation mechanism with the overall design of the  $\mu$ TAS. For example, if the fabrication material and actuation mechanism used for the micromixer and the micropump used in  $\mu$ TAS are the same, the fabrication process and integration becomes easier.

#### **1.10.4 Microseparator**

The separation of the target biomolecules from a test sample is an important part of the biochemical analysis. One of the methods for isolating biomolecules of interest from the bulk sample is by attaching them to functionalized microbeads through a mixing process, followed by separation of the microbeads. In recent years, various separation techniques have been reported and most of these involve continuous flow separation where the sample solution is continuously introduced through a separator device. There are various separation techniques that can be used for separation of the particles of interest from the test sample. Pinched flow fractionation [149] and hydrodynamic filtration [150] permit size based sorting of micrometer sized particles. Filtration obstacle separator [151] is based on flow through an array of pillars where the spacing between pillars is designed to function as an obstacle to particles in the sample. Lateral displacement separation [152] is based on pressure gradient from slanted obstacles designed to perform a size based separation of microparticles, DEP [153] is a separation technique where non uniform electric field can be used for separation based on the size and polarisability of microparticles. In recent times, the use of magnetic micro and nanobeads for immunomagnetic separation has gained popularity. The use of magnetic microbeads allows for magnetic separation. The magnets used can be external or integrated within the device. The advantage of an integrated magnet is that the magnetic field strength requirement is low due to the close proximity of the magnetic beads to the microfabricated magnet. Several integrated electromagnets such as the meandering permalloy-core, copper-wire design [154], the spiral design [155] and the serpentine copper-wires with a semi-encapsulated permalloy [156] have all been explored. However, the process of integrating microfabricated magnets with a microfluidic device takes many complicated fabrication steps, which make the approach costly. External

permanent magnets used for magnetic bead based immunoassay are usually Neodymium Iron Boron (NdFeB) magnets with a magnetic flux density up to 500 mT at the pole surface [157]. External electromagnets have the advantage of switching on and off and their field strength can be varied. However, electromagnets have not been as popular as permanent magnets because even with a large number of windings and high currents, it is difficult to build a small electromagnet with field strength comparable to a small NdFeB magnet. Also, electromagnets also have a joule heating problem.

#### **1.10.5 Microsensor**

The different types of biosensors based on the bio-recognition element and the transducer element are discussed in the previous section. The biosensors can also be broadly classified into label-free and labeled biosensors. In case of the labeled biosensors, labels such as fluorescent tags, luminescent compounds or radioisotope labels are attached to the target molecule to enhance signal generation and visualization. The labeling methods are time consuming and complicated and can substantially increase the assay complexity. Additionally, the attachment of labels can interfere with the molecular reaction and labeled biosensors cannot be used for real time measurements. A label-free biosensor on the other hand can be used for direct real time detection involves lesser assay complexity and is noninvasive in nature. Label free assays are faster than the labeled ones because they do not need additional incubation time and activation step for the attachment of labels. Several biosensors such as SPR, QCM, impedance biosensor, fiber optic immunoassay and magnetoelastic-immunosensors have been developed. Among the label-free biosensors, the impedance biosensors have added advantages due to their simplicity of operation and the speed of assay. Also, impedance biosensors have no moving parts and are easier to fabricate and integrate within a point-of-care testing device.



## 1.11 Primary Objectives of Study

The primary goal of the study is the development of a PDMS based  $\mu$ TAS for rapid, multi-purpose, impedance based detection of biomolecules. The following objectives have been established to attain the primary goal.

1. Design, fabrication and testing of pneumatically actuated PDMS based micropumps
2. Design, fabrication and testing of pneumatically actuated PDMS based active micromixers
3. Integration of micropump and micromixer with interdigitated electrodes (IDE) for impedance measurements
4. Numerical simulation of microfluidic components using COMSOL Multiphysics<sup>TM</sup>
5. Development of magnetic microbead separation scheme
6. Application of integrated microfluidic system towards biotin conjugated fluorescent (BCF) microbead detection based on streptavidin-biotin conjugation reaction.
7. Application of integrated microfluidic system towards immuno microbead based insulin detection

### 1.11.1 Specific Tasks

The individual tasks associated with the primary areas described previously are listed below.

#### *i. Design, fabrication and testing of pneumatically actuated PDMS based micropumps*

1. Mask design and fabrication of SU-8 mold

2. PDMS casting and oxygen plasma bonding followed by packaging
3. Flow characterization of three different designs of micropump

*ii. Design, fabrication and testing of pneumatically actuated PDMS based active micromixers*

1. Mask design and fabrication of SU-8 mold
2. PDMS casting and oxygen plasma bonding followed by packaging
3. Mixing efficiency characterization of three different designs of micromixer

*iii. Integration of micropump and micromixer with IDE for impedance measurements*

1. Mask design for integrated device and SU-8 mold fabrication
2. PDMS casting and oxygen plasma bonding followed by packaging
3. Flow characterization of micropump
4. Mixing efficiency characterization of the micromixer

*iv. Development of magnetic microbead separation scheme*

1. Selection of permanent magnet and configuration to optimize microbead separation
2. Separation efficiency at different sample flow rates

*v. Application of integrated microfluidic system towards immuno microbead based insulin detection*

1. Mask design for integrated microfluidic system and SU-8 mold fabrication

2. PDMS casting and oxygen plasma bonding followed by packaging
3. Testing integrated microfluidic system for detecting BCF microbeads and insulin

### **1.12 Dissertation Organization**

The remainder of this dissertation is divided into six chapters: Chapter 2: Theory and Design, Chapter 3: Microfabrication, Chapter 4: Experimental Setup and Testing, Chapter 5: Results and Discussions, Chapter 6: Conclusions and Chapter 7: Future Work. A bibliography of references is provided at the end of the dissertation. The second chapter provides details of the theory of operation, mask design and dimensions of the various devices fabricated. The third chapter describes the microfabrication procedure for all the components of the microfluidic system. The fourth chapter discusses all the experimental setup and testing protocols used in this study. The fifth chapter presents and discusses the results of the various experiments and simulations. The sixth and the seventh chapters summarize the accomplishments of this study and identify the areas in which future work can be accomplished.

## **2. THEORY AND DESIGN**

The following sections describe the theory and design of the microfluidic system components used in the present study. The focus will be on the design of the various components of the integrated microfluidic system such as micropump, micromixer, microbead magnetic separation scheme and impedance sensor.

### **2.1 Micropump**

#### **2.1.1 Working Principle**

The micropump consists of two PDMS layers bonded together by oxygen plasma bonding. One of the layers, referred to as the control layer, contains a sequence of air chambers that are connected via microchannels. The first air chamber has a smaller volume compared to the rest. The bottom surface of these air chambers is thin and functions as membranes that deflect when the air chambers are filled with compressed air. The second PDMS layer, referred to as the fluidic layer has a microchannel through which the fluid is pumped. An external mini air compressor is used to produce compressed air supply for the micropump. The pneumatic actuation frequency is controlled via a 3-port ultra-miniature solenoid valve. When a voltage is applied across the solenoid, the solenoid connects the micropump's actuator layer inlet to the compressed air supply. When compressed air is introduced into the air chamber inlet via a solenoid valve, air fills the three air chambers in a sequence, starting with the smallest chamber. The membrane of the smallest chamber deflects first and functions as an active valve to minimize back flow. There is a time delay between the filling of different air chambers due to the difference in chamber volume and also the presence of the interconnecting microchannels. The deflection of the membranes in a sequence leads to a peristaltic actuation and causes the fluid in

the underlying fluidic layer to be squeezed in one direction as shown in the Figure 2.1. When the solenoid valve is turned off the compressed air is released through the same path it enters the air chamber and the air chambers are depressurized causing the membrane to move back to its initial position with zero deflection.

### **2.1.2 Micropump Geometry**

Figure 2.2 shows the various layers of the micropump assembly. Both the PDMS layers have a glass layer for mechanical support with access holes for inlet and outlet. Three different micropump design geometries were developed and evaluated in the present study. The three designs differ in the geometry of the air chambers and the length of the interconnecting microchannels. The AutoCAD diagrams of the three micropump designs, namely Design1, Design2 and Design3 are as shown in Figures 2.3, 2.4 and 2.5 respectively. The fluidic layer microchannel design was the same for all three pumps. Figure 2.6 shows the design of the fluidic layer microchannel. The design of the air chambers of the control layer is a significant design parameter, since it governs the dynamic response of the micropump such as the peak operating frequency and the volume displaced per stroke. In general, large air chambers displace large fluid volume per stroke and thus lead to a large flow rate. Also, large air chambers require long fill and evacuate time, thus affecting the peak operating frequency of the micropump. The interconnecting microchannels between the air chambers provide a time delay between the sequential actuation of each membrane. This cycle of pressurizing and depressurizing of the air chambers due to the on-off cycle of the solenoid valve can actuate the fluid flow in one direction

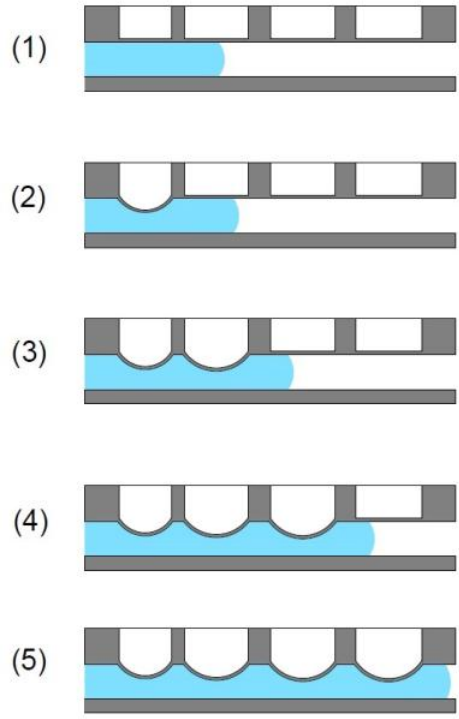


Figure 2.1 Cross-sectional view of the actuation mechanism of the pump. (1) Liquid enters the microchannel (2) When compressed air fills the air chambers, the first membrane deflects downwards (3) – (5) sequential actuation of PDMS membranes causing the liquid to be pumped to the right.

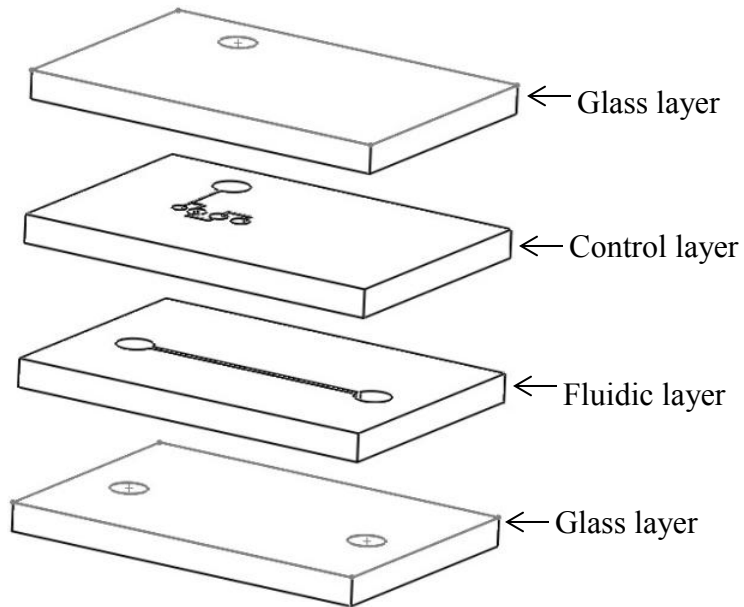
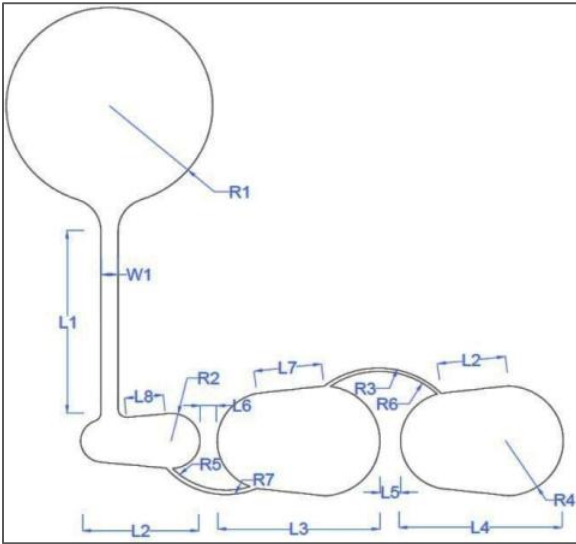
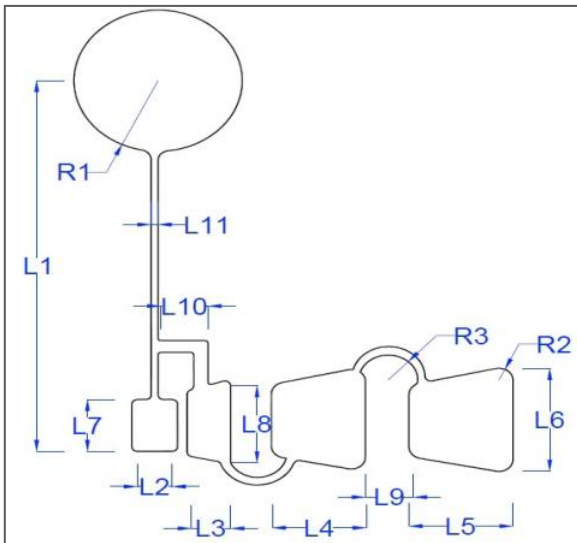


Figure 2.2 Various layers of the micropump assembly



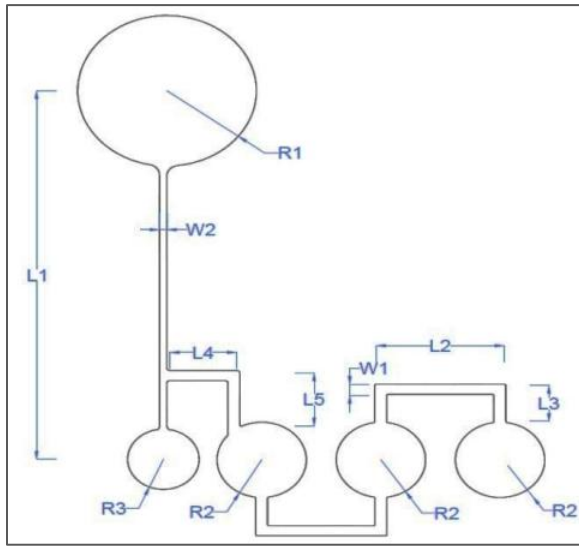
Label	Dimension (mm)	Label	Dimension (mm)
R1	3.0	L1	5.8
R2	0.84	L2	1.98
R3	2.41	L3	4.75
R4	1.68	L4	4.82
R5	2.16	L5	0.61
R6	2.54	L6	0.5
R7	2.27	L7	1.98
W1	0.5	L8	1.32

Figure 2.3 Micropump Design1 – Control Layer



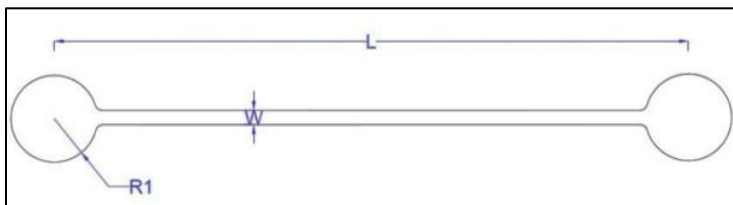
Label	Dimension (mm)	Label	Dimension (mm)
R1	1.5	L5	1.86
R2	0.25	L6	2.18
R3	0.53	L7	1.1
L1	7.77	L8	1.8
L2	0.62	L9	0.77
L3	0.78	L10	0.79
L4	1.68	L11	0.13

Figure 2.4 Micropump Design2 – Control Layer



Label	Dimension (mm)
R1	1.5
R2	0.75
R3	0.75
L1	7.93
L2	2.13
L3	0.74
L4	1.17
L5	1.06
W1	0.23
W2	0.13

Figure 2.5 Micropump Design3 – Control Layer



Label	Dimension (mm)
L	22
R1	1.5
W	0.5

Figure 2.6 Fluidic layer microchannel design

## 2.2 Micromixer

### 2.2.1 Working Principle

The micromixers used in this study utilize oscillating membranes to achieve active mixing. The micromixer consists of two PDMS layers bonded together by oxygen plasma bonding. One of the layers, referred to as the control layer, has air chambers. The bottom surface of the air chambers functions as a membrane that can deflect when the air chamber is filled with



compressed air. An external mini air compressor is used to produce compressed air supply for the micromixer. The pneumatic actuation frequency is controlled via a 3-port ultra-miniature solenoid valve. When a voltage is applied across the solenoid, the solenoid connects the micromixer's actuator layer inlet to the compressed air supply, causing the membranes to deflect. The second PDMS layer, referred to as the fluidic layer, has a mixing chamber with two inlets and one outlet. The two PDMS layers are bonded together by oxygen plasma bonding, with the mixing chamber in alignment with the air chambers. A set of glass layers with access holes to the inlet and outlets of the PDMS layers provide mechanical support. Figure 2.7 illustrates the motion of the micromixer membrane during one actuation cycle.

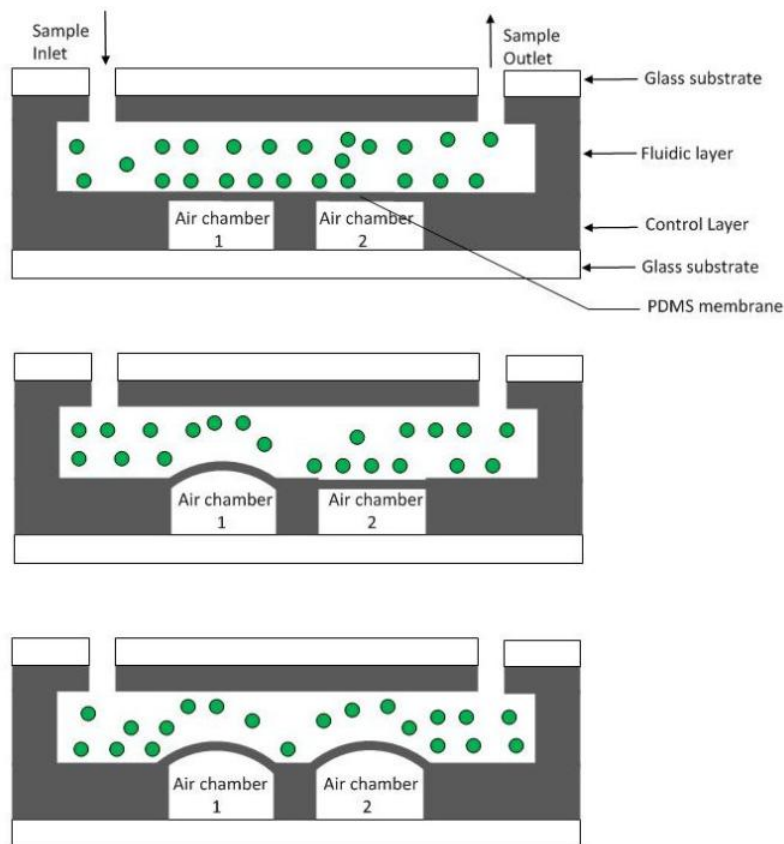


Figure 2.7 Working of a micromixer with two pneumatically actuated membranes

These PDMS membranes can be moved up and down sequentially and the membrane deflection generates fluid convection in the mixing chamber. This agitates the mixing species leading to better mixing. When the solenoid valve is turned off the compressed air is released through the same path it enters the air chamber and the air chambers are depressurized causing the membrane to move back to its initial position with zero deflection.

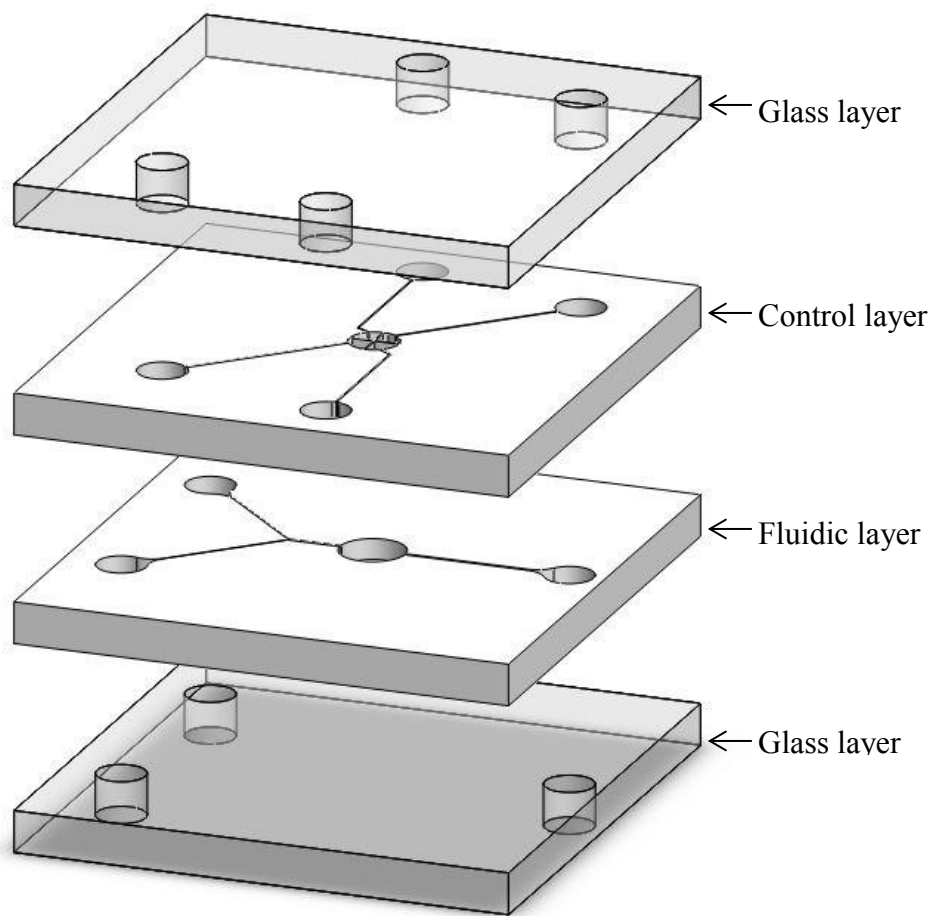


Figure 2.8 Various layers of the micromixer assembly

### 2.2.2 Micromixer Geometry

In the present study, three different micromixer design geometries were developed and evaluated. The primary difference between these designs is the membrane configuration in the control layer and the interconnecting delay microchannels. Design1, as shown in Figure 2.9, uses two independently operated semi-circular membranes to achieve mixing. Design2, as shown in Fig. 2.10, utilizes four separate quadrant membranes which can be independently controlled. Design3, as shown in Figures 2.11a and 2.11b, uses 6 membranes that can deflect in a sequence. In Design3, unlike Designs 1 and 2, the air chambers are interconnected in series by microchannels (100  $\mu\text{m}$  x 100  $\mu\text{m}$ ). The first air chamber in the series is connected to the compressed air source and the interconnecting microchannels provide the delay between the sequential actuation of each membrane. The fluidic channel layer for all the micromixers is the same and consists of a circular mixing chamber with two inlets and one outlet. Figure 2.12 shows the design geometry of the fluidic layer of the mixer.

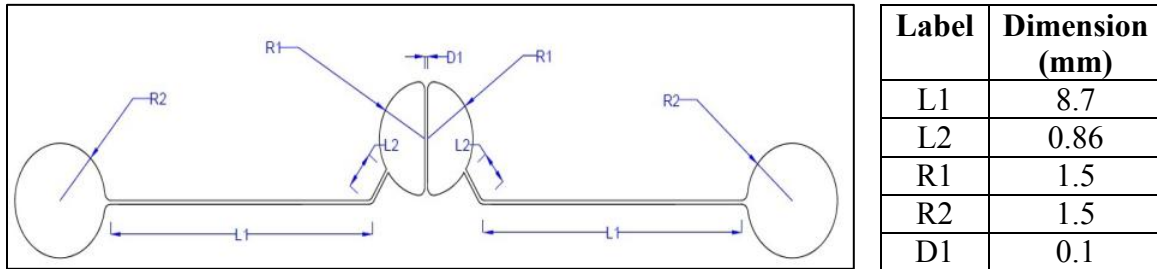
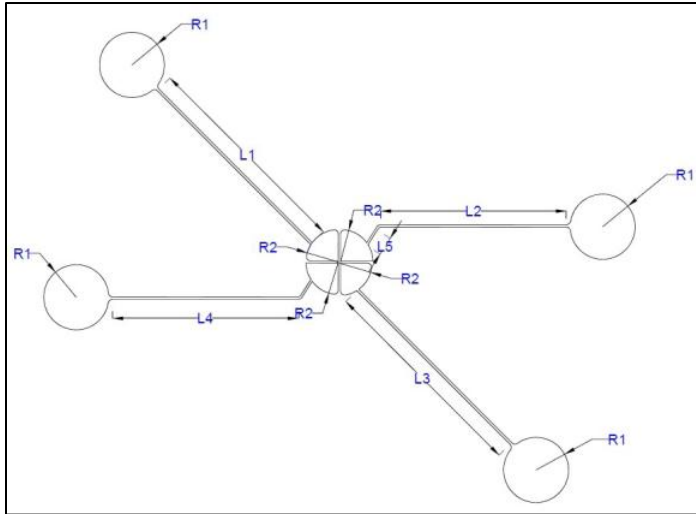


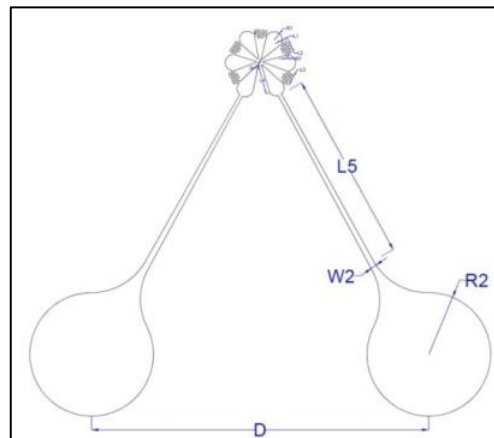
Figure 2.9 Micromixer Design1 control layer with two semi-circular air chambers



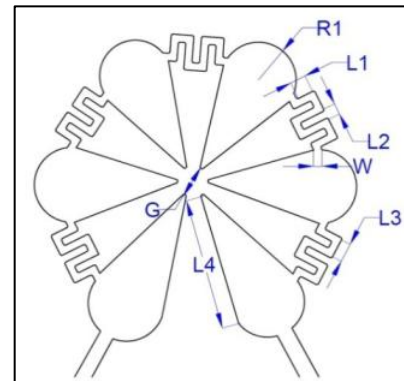
Label	Dimension (mm)
R1	1.5
R2	1.5
L1	10
L2	8.6
L3	10
L4	8.6

Figure 2.10 Micromixer Design2 control layer with four quadrant air chambers

Label	Dimension (mm)
L5	4.8
W2	0.14
R2	1.5
W	0.04
L1	0.1
L2	0.05
L3	0.12
G	0.17
L4	0.7

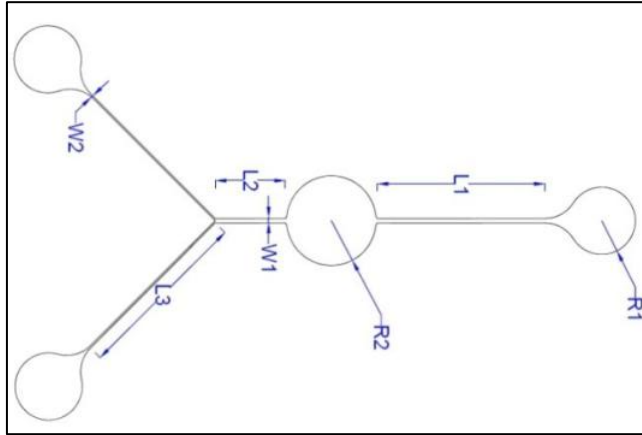


(a)



(b)

Figure 2.11 (a) Micromixer Design3 control layer with six air chambers connected in series (b) Close up view of the Design3 air chambers



Label	Dimension (mm)
R1	1.5
L1	7.5
L2	3.2
W1	0.2
R2	2
L3	8
W2	0.1

Figure 2.12 Fluidic layer of the micromixer with a mixing chamber

### 2.3 Integration of Micropump and Micromixer

The individual micropumps and micromixers were tested for their performance. Among the micropump and micromixer designs, Design3 of the micropump and Design3 of the micromixer were selected for integration into a single microfluidic system. The performance and selection criteria for the micropump and micromixer will be discussed in Chapter 5 (Results and Discussions). The control layers of selected micropump and micromixer designs were combined into a single PDMS control layer to achieve an integrated micromixer-micropump system. Figure 2.13 shows the various layers of the fully integrated micromixer-micropump system. The design of the fluidic layer for the integrated micromixer-micropump system is shown in Figure 2.14. Figure 2.15 shows the alignment of the control layer on top of the fluidic layer of the integrated micromixer-micropump system. The important alignment requirements are to center the micromixer air chambers with the mixing chamber below and position the micropump air chambers on top of the microchannel.

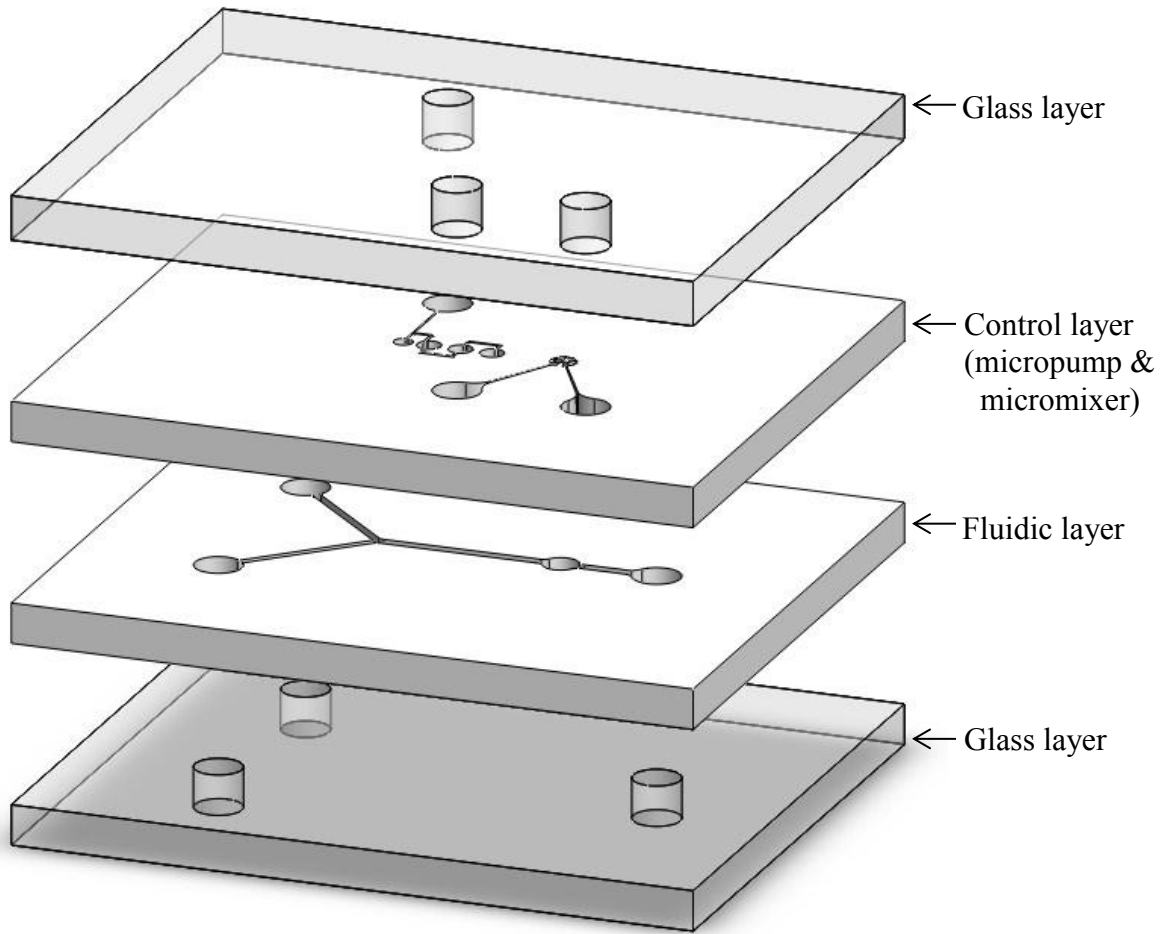
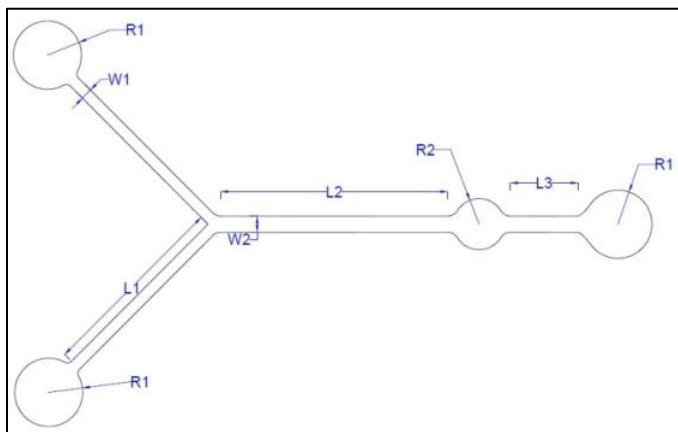
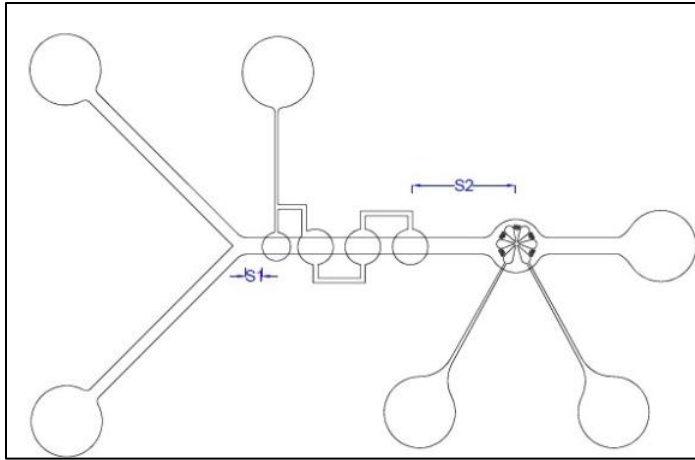


Figure 2.13 Different layers of the integrated micromixer-micropump assembly



Label	Dimension (mm)
R1	1.5
W1	0.5
L1	8.5
W2	0.7
L2	10
R2	1.125
L3	3

Figure 2.14 Fluidic layer of the integrated micromixer-micropump



Label	Dimension (mm)
S1	0.7
S2	4.3

Figure 2.15 Alignment of the layers of integrated micromixer-micropump

## 2.4 Impedance Spectroscopy (IS)

The electrical impedance  $Z$  of a system can be determined by applying a small amplitude voltage perturbation to the system and then measuring the current response.  $Z$  is the ratio of the voltage - time function  $V(t)$  and the resulting current-time function  $I(t)$

$$Z = \frac{V(t)}{I(t)} = \frac{V_o \sin \theta}{I_o \sin(2\pi ft + \phi)} = \frac{1}{Y} \quad (2.1)$$

where  $V_o$  and  $I_o$  are the peak voltage and current,  $f$  is the frequency,  $t$  is the time,  $\Phi$  is the phase shift between the voltage-time and current-time functions, and  $Y$  is the complex conductance or admittance.  $Z$  is a complex function and can be described by the modulus  $|Z|$  and the phase shift  $\Phi$  or by the real part  $Z_R$  and the imaginary part  $Z_I$ , as illustrated in Figure 2.16 The impedance data can be plotted in two different ways: the Bode plot which plots  $\log |Z|$  as a function of  $\log f$ , or the Nyquist plot which plots  $Z_R$  versus  $Z_I$ . The name IS refers to the fact that impedance generally varies with frequency. The impedance spectrum is often analyzed using the theory of equivalent circuit, which uses circuit elements such as resistances and capacitances to represent

the various physicochemical properties of the system under study [158]. The experimental data is curve-fitted by the equivalent circuit model using non-linear least square fitting techniques.

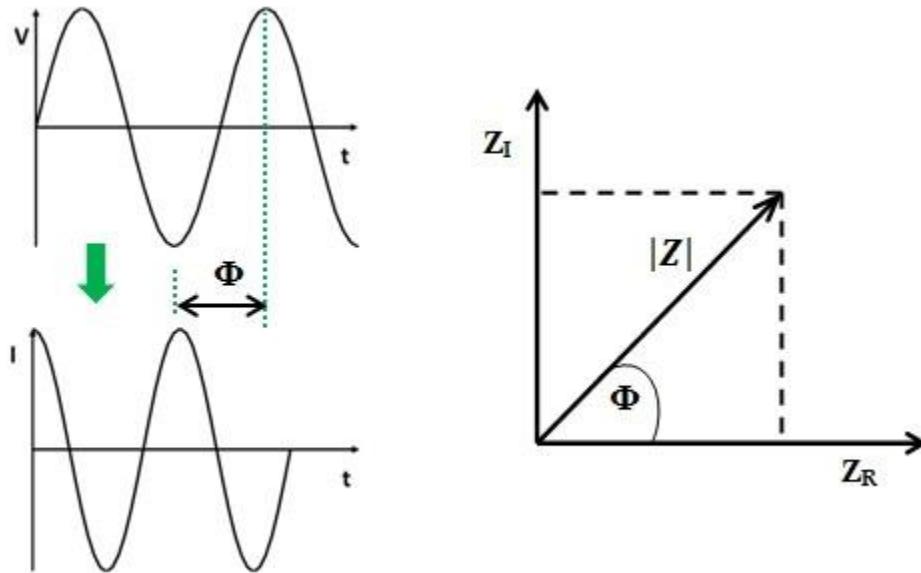


Figure 2.16 Components of Impedance

#### 2.4.1 Impedance Spectrum Measurement for a Microfluidic System

An impedance measurement setup for a microfluidic system typically consists of at least two electrodes within an electrode cell which contains the test sample. An impedance analyzer is connected to the electrodes to perform an impedance scan. A schematic of the impedance measurement scheme is shown in Figure 2.17. The impedance analyzer applies an AC voltage perturbation and the current flows through all components of the system, the electrodes, the suspension medium and the analyte.



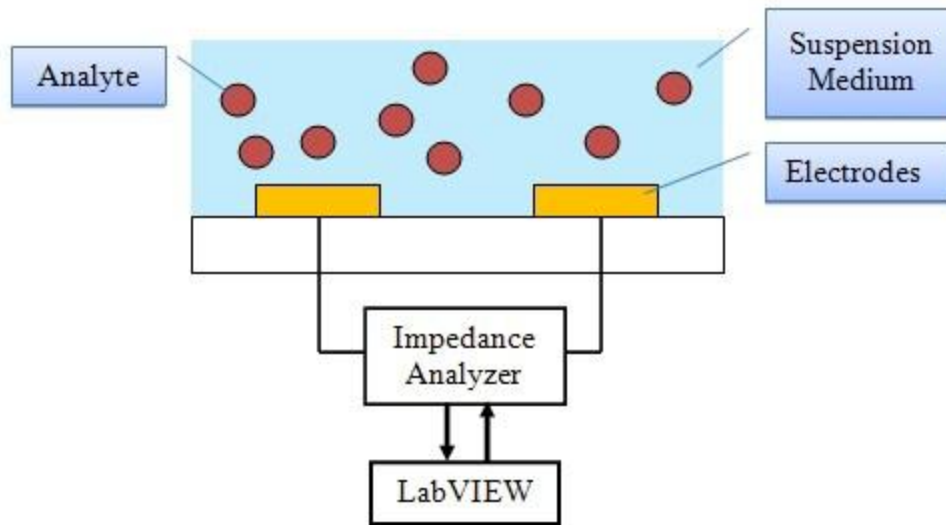


Figure 2.17 Impedance spectrum measurement setup for a microfluidic system

The measured impedance is therefore the sum of the contributions from all the components of the system. Some of the latest impedance analyzers also contain post-processing capabilities to perform equivalent circuit analysis. The impedance spectrum is measured as a function of the concentration of the analyte in the suspension medium. The frequency range of the impedance measurement can vary with the system under study but usually ranges from 5 Hz up to 10 MHz. The suspension medium can be used as the control/reference in impedance measurement. The impedance data for various analyte concentrations is compared with the control data to determine the change in impedance caused by the presence of analyte in the suspension medium.

#### 2.4.2 Design of Interdigitated Electrode (IDE)

The electrode configuration for impedance measurement can be IDE, double or triple electrodes. The choice of electrode material is also important because it can affect the chemistry and ease of functionalization of the electrode surface. Other selection criteria include durability and stability under measurement conditions, the possibility of cleaning and sterilizing the electrode surface

and biocompatibility. The most common electrode material is gold, but platinum and carbon electrodes have also been reported. Gold is a very good electrode material due to its relatively fast electrode kinetics and the possibility of forming self-assembled monolayers (SAM) to immobilize biorecognition element on the electrode surface. IDE is highly desirable in impedance measurement because of its well-defined geometry and reproducibility in fabrication [159]. IDE consists of multiple leads with branched electrode fingers interwoven between the leads [160]. Figure 2.18a shows a basic IDE configuration, including the electrical contact pads, side rails and interdigitated fingers. Figure 2.18 (b) shows the various design dimensions of an IDE configuration. In Figure 2.18 (b),  $L$  is the length of the electrode finger,  $W$  is the width of the electrode finger,  $S$  is the spacing between the electrode fingers,  $G$  is the gap between side rail and finger,  $A$  is the width of bond pad,  $B$  is the length of bond pad,  $C$  is the length of connection between bond pad and side rail. Figure 2.19 shows the various layers of an IDE chip assembly. The sensing area of the IDE is the region between the opposing electrode rails. The performance of the IDE for impedance measurements in a microfluidic chamber depends on the geometric design of the IDE and can be significantly impacted by variability or defects in manufacturing or material [160]. Several IDE configurations were designed and included alterations to the width of the electrodes, spacing between electrodes and the number of pairs of electrodes. The electrode material was gold for all designs. Table 2.11 lists the various IDE configurations used in the present study.

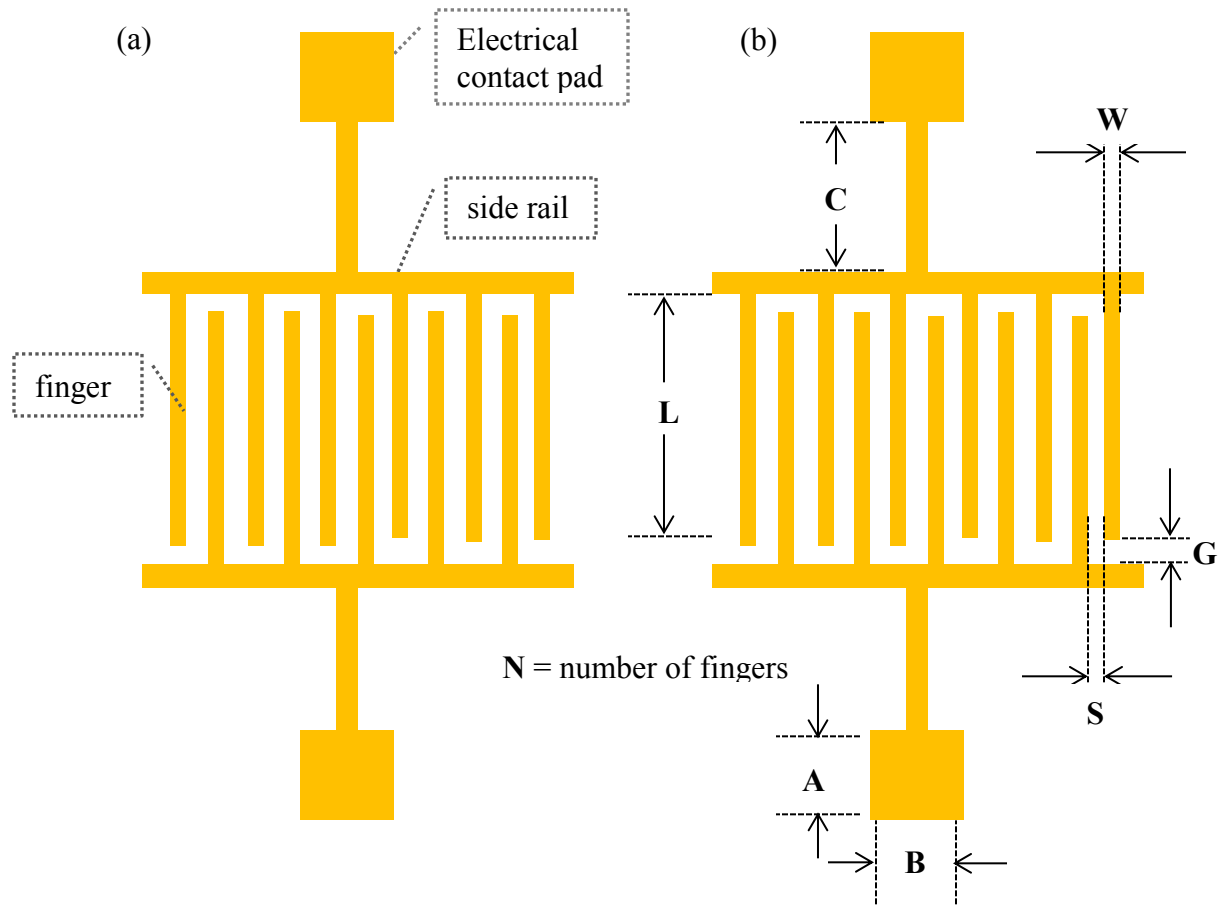


Figure 2.18 (a) Basic IDE features (b) Dimensions of IDE

Name	N	S ( $\mu\text{m}$ )	W ( $\mu\text{m}$ )	L (mm)	A (mm)	B (mm)	C (mm)	G ( $\mu\text{m}$ )
Design 25-10	20	20	20	0.9	4	4	16.6	50
Design 25-ext	50	20	20	2.83	4	4	16.6	100
Design 25-int	50	20	20	0.89	4	4	16.6	50
Circular	50	20	20	0.79-1.75	4	4	17	50

Table 2.1 Design dimensions of various IDE designs

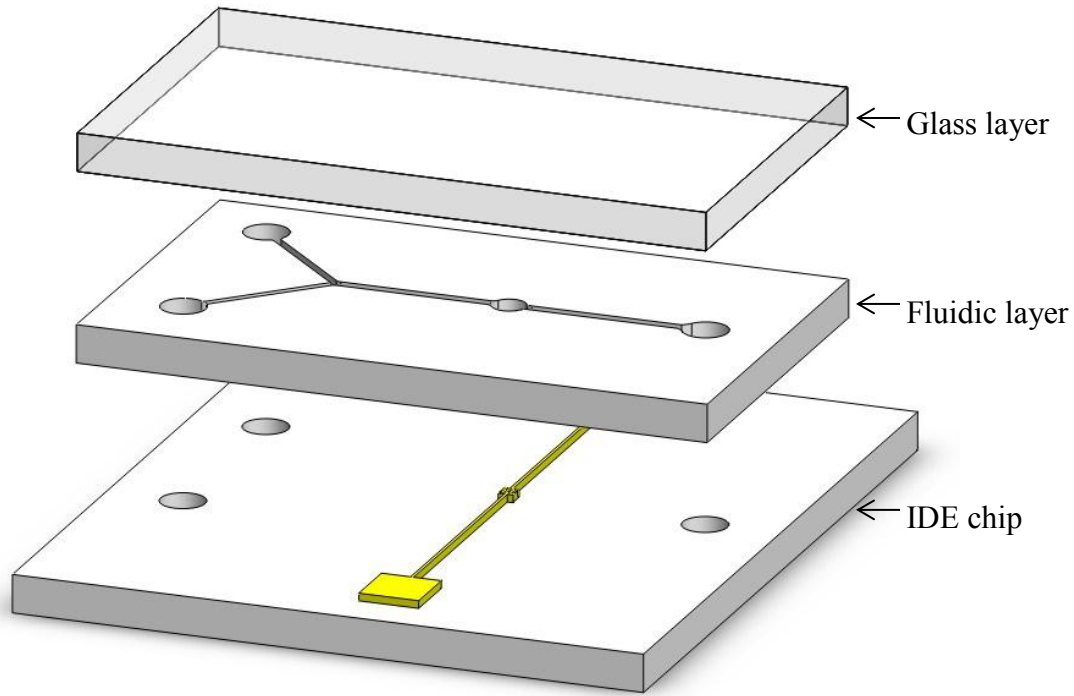


Figure 2.19 Various layers of an IDE chip assembly

## 2.5 Magnetic Separation Techniques

The magnetic force acting on a single magnetic particle is given by [161]

$$\bar{F}_{\text{mag}} = -\bar{\nabla}U = -V\chi\bar{\nabla}u = \frac{1}{2}\frac{V\chi}{\mu_0}\nabla B^2 \quad (2.2)$$

where  $\nabla B^2$  is the magnetic density gradient,  $\chi$  is the susceptibility of the magnetic particle,  $V$  is the volume of the magnetic particle, and  $\mu_0$  is the permeability of free space. If the magnetic particle moves in a suspension medium, it also experiences the hydrodynamic drag  $\bar{F}_{\text{drag}}$  and gravitational forces  $\bar{F}_g$  and can be calculated using the following equations.

$$\bar{F}_{\text{drag}} = 6\pi\eta R(V_p - V_{\text{medium}}) \quad (2.3)$$

$$\bar{F}_g = V_p(\rho_p - \rho_{\text{medium}})g \quad (2.4)$$

where  $V_p$ ,  $V_{\text{medium}}$ ,  $\rho_p$  and  $\rho_{\text{medium}}$  are the particle velocity, medium velocity, particle density and medium density, respectively. Solving for  $(V_p - V_{\text{medium}})$  for a particle with radius  $R$ ,

$$(V_p - V_{\text{medium}}) = -\frac{1}{9} \frac{R^2 \chi}{\mu_0 \eta} \nabla B^2 - \frac{2}{9} \frac{R^2}{\eta} (\rho_p - \rho_{\text{medium}})g \quad (2.5)$$

The hydrodynamic drag force is the most significant force acting against the magnetic force on the bead. The magnetic capture force will dominate when

$$F_{\text{mag}} > F_{\text{drag}} \quad (2.6)$$

## 2.6 Integration of Micropump, Micromixer, and IDE

A systematic study was carried out to determine the performance of the various designs of micropumps and micromixers. Based on the results (to be discussed in Chapter 5), Design3 of micropump and Design3 of micromixer were selected for the fully integrated microfluidic system. The fully integrated microfluidic system consists of a PDMS control layer with the micromixer and micropump, a PDMS fluidic layer with the mixing chamber and an IDE on glass substrate. The PDMS fluidic layer and the IDE on glass substrate are aligned such that the mixing chamber covers the IDE. Figure 2.20 shows the various layers of the fully integrated microfluidic system. Figure 2.21 shows the outer dimensions of the control layer. Figure 2.22 shows the dimensions of the fluidic layer. Figure 2.23 shows the outer dimensions of the IDE chip. Figure 2.24 shows the outer dimensions of the alignment.

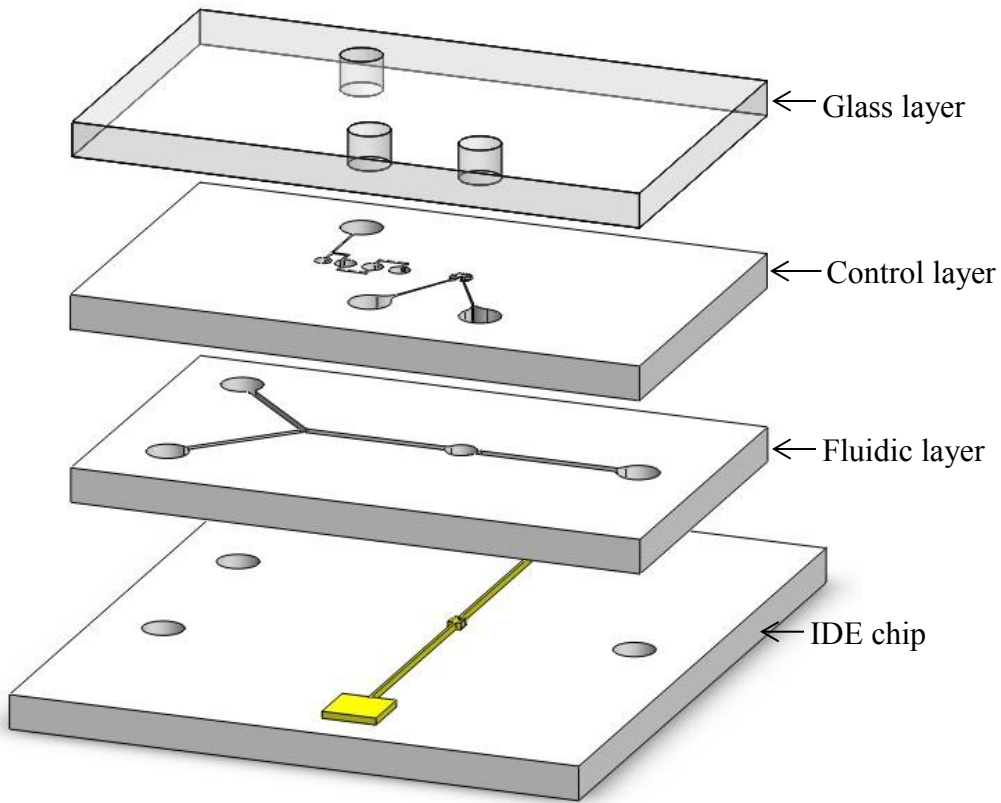


Figure 2.20 Different layers of the fully integrated device assembly

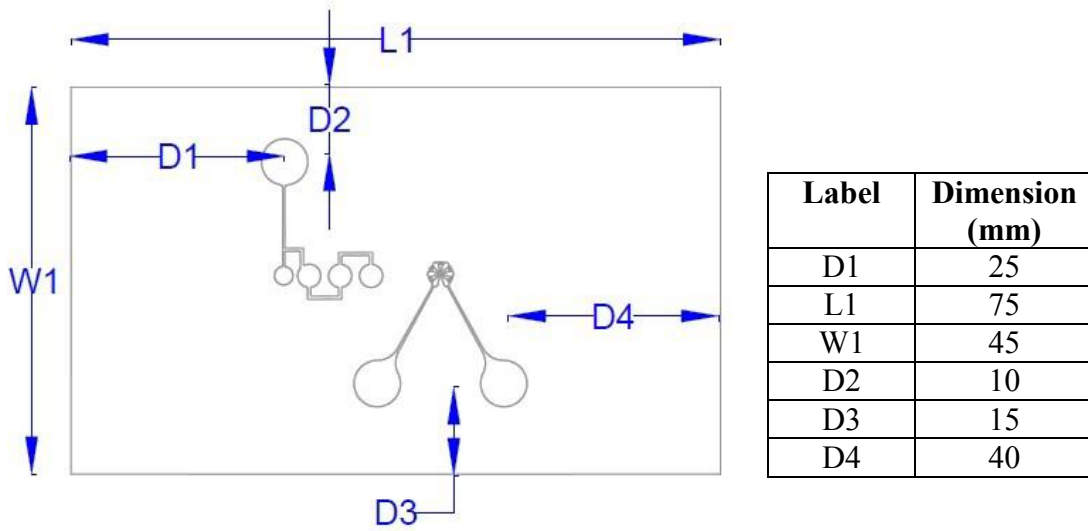


Figure 2.21 Outer dimensions of the control layer

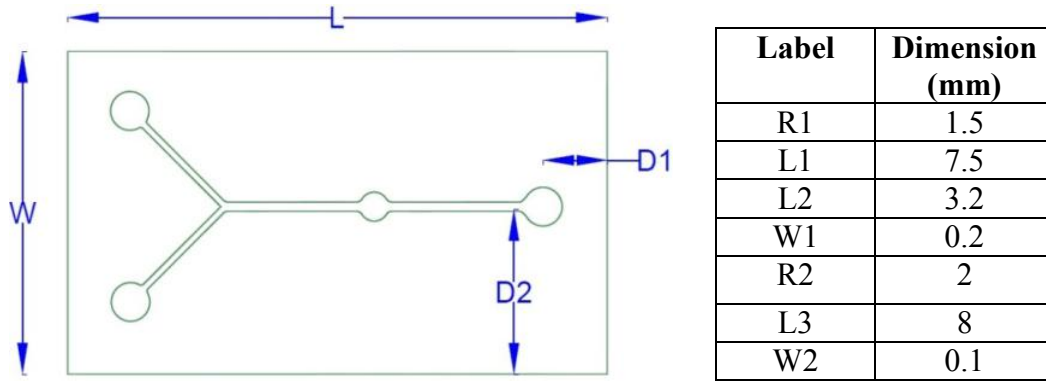


Figure 2.22 Outer dimensions of the fluidic layer

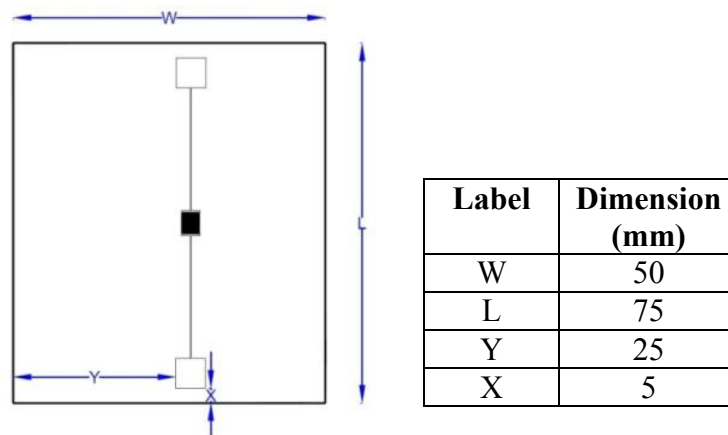


Figure 2.23 Outer dimensions of the IDE layer

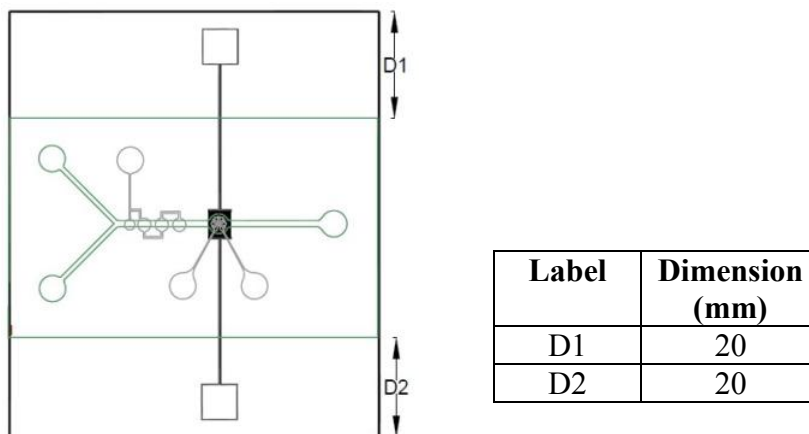


Figure 2.24 Outer dimensions of the alignment

## 2.7 Biotin-Streptavidin Interactions in Assay Systems

Streptavidin is a protein with four identical subunits, each containing a high affinity binding site for biotin (also known as vitamin H). The dissociation constant  $K_D$  of the biotin-streptavidin complex is on the order of  $\sim 10^{-15}$  which is among the strongest non-covalent interactions known in nature and about  $10^3$ - $10^6$  times greater than the interaction of ligands with their specific antibodies [162]. This high dissociation constant ensures that once a streptavidin-avidin complex is formed, the complex is not affected by any pH changes, presence of chaotropes, or any washing steps required for the protocol. The biotin-streptavidin interaction is a widely used affinity pair in molecular, immunological, and cellular assays. The specificity of biotin-streptavidin complex has been used as a basis for developing assay systems to detect or quantify analytes. A common application for biotin-streptavidin interaction is in immunoassays. The specificity of antibody molecules provides the targeting capability to recognize and bind particular antigen molecules. If biotin labels are attached to the antibody, and the streptavidin is in turn labeled with a signal generating substance such as an enzyme or fluorophore, then a very sensitive antigen detection system can be created based on the biotin-streptavidin reaction.

### 2.7.1 Biotin-Streptavidin Conjugation Reaction

The biotin-streptavidin conjugation reaction was utilized in the present study to determine the performance of the micromixer and also to test the fully integrated microfluidic system for the detection of biotin conjugated fluorescent (BCF) microbeads. In this study, two surface functionalized beads were used: BCF microbeads and streptavidin conjugated paramagnetic (SCP) microbeads. The details of the BCF and SCP microbeads are mentioned in Chapter 4. After mixing, the biotin-streptavidin complex can be magnetically separated as depicted in



Figure 2.25 and the fluorescence signal from the biotin coated fluorescent beads can be measured using a fluorometer to estimate the quantity of the biotin-streptavidin microbead conjugates. The intensity of the fluorescence signal indicates the extent of the binding reaction between the two functionalized beads and indirectly indicates the performance of the micromixer.

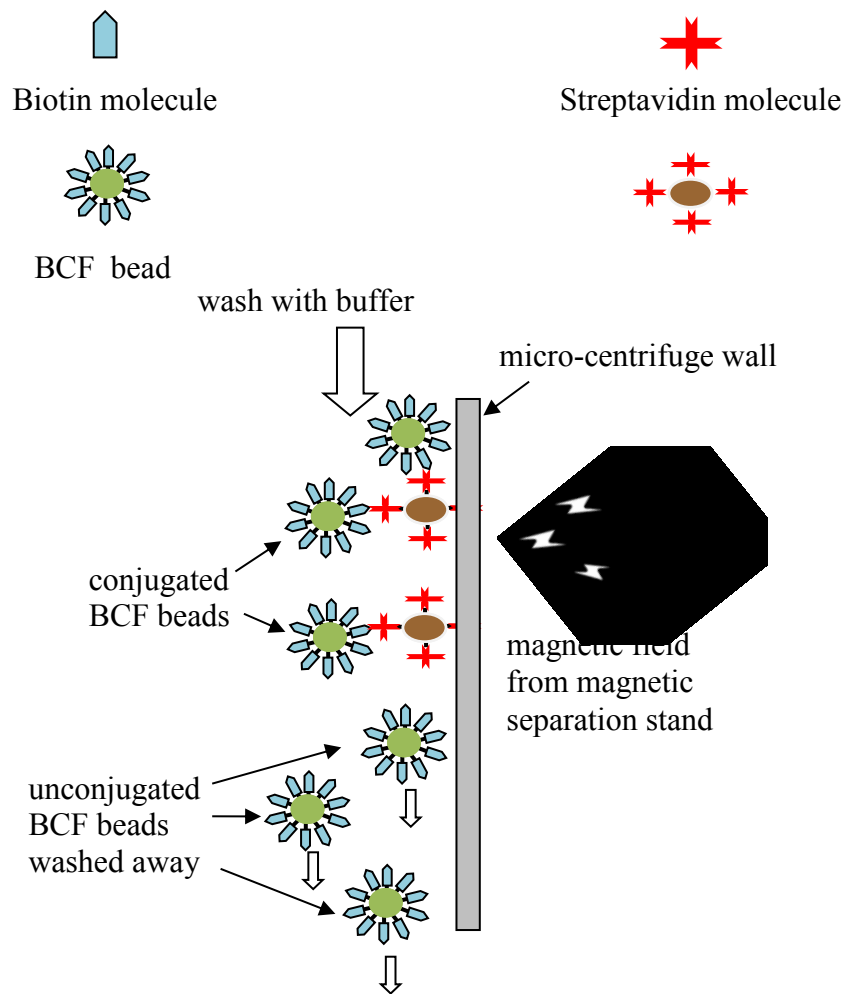


Figure 2.25 Biotin Streptavidin conjugation reaction

## 2.8 Insulin Detection

The fully integrated microfluidic system was tested for the immuno microbead based insulin detection. The details of all the chemicals, microbeads, type of insulin and insulin antibody used are mentioned in Chapter 4. Figure 2.26 shows the various steps used in preparation of samples and the insulin detection protocol used in the present study.

The carboxyl groups on the surface of the microbeads are first activated by combining with EDC. The activation of the carboxyl groups allows it to covalently attach to the amine groups on antibodies. The activated magnetic beads are combined with the unconjugated mouse anti-insulin (1G11) monoclonal antibody (MAI-Ab) to yield Magnetic Beads-Antibody Conjugate (MBAC). The prepared MBAC is then mixed with target insulin molecules to allow binding reaction between target insulin molecules and MAI-Ab. An external magnet is used to separate the MBAC-target insulin complex from the solution. The unbound target insulin molecules are removed by washing with a buffer solution. The wash step is followed by an impedance spectrum measurement.

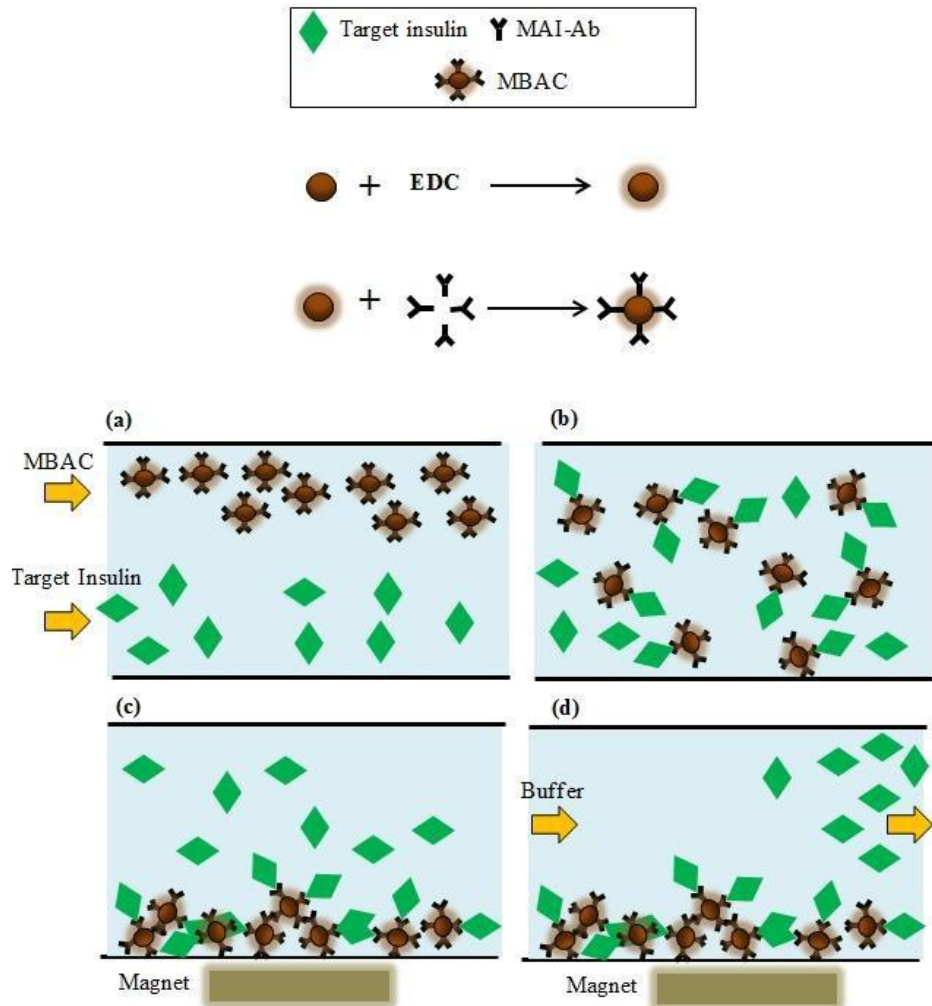


Figure 2.26 Basic steps in insulin sample preparation (a) Introduction of MBAC target insulin, (b) mixing and binding of the target insulin to MBAC (c) magnetic separation of the target insulin and MBAC complex, (d) washing of the unbound insulin by buffer

### 3. MICROFABRICATION

The microfabrication methods for the various components of the microfluidic system are described in detail in this chapter. The microfluidics components including the microchannel, microvalve, micropump and micromixer were fabricated by soft lithography rapid prototyping of PDMS and SU-8 photoresist. The microelectrodes for the impedance detection module were fabricated by traditional MEMS based micromachining of Chrome/Gold thin-film layer on a glass substrate.

#### 3.1 PDMS Soft Lithography

Figure 3.1 demonstrates the process flow used to fabricate the PDMS components. The actual fabrication was performed at the High Density Electronics Center (HiDEC) of the University of Arkansas and the Arkansas Micro and Nano Systems Laboratory. The details of the process flow shown in Figure 3.1 are provided in the following sections.

#### 3.2 Mask Design

All mask designs were drafted using AutoCAD. The mask size was designed to be compatible with 5 inch wafers. The AutoCAD designs were sent to Advance Reproductions (North Andover, MA) where transparency photo masks with a  $\frac{1}{4}$  mil resolution were manufactured. The transparency photo mask is suitable for designs at a resolution limit of about  $15\mu\text{m}$ . Each photo mask was cut into a 5" circle and fixed onto a 6" glass substrate using double-sided Scotch tape<sup>®</sup>.

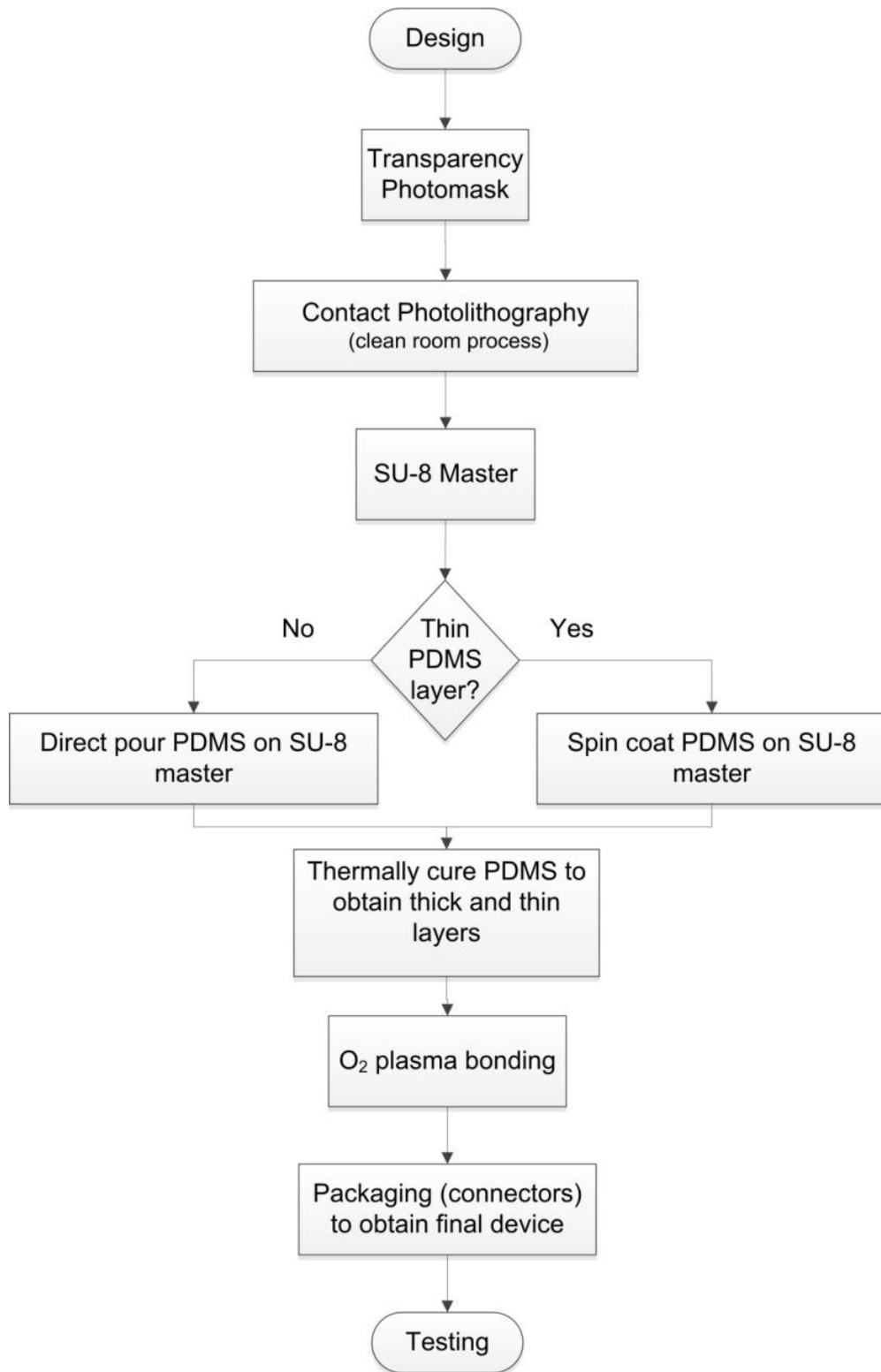


Figure 3.1 Soft lithography process flow for a PDMS component fabrication

### 3.3 Fabrication of SU-8 Master Mold

Using the transparency masks, SU-8 master molds were fabricated for casting PDMS. The process flow for the fabrication process is shown in Figure 3.2.

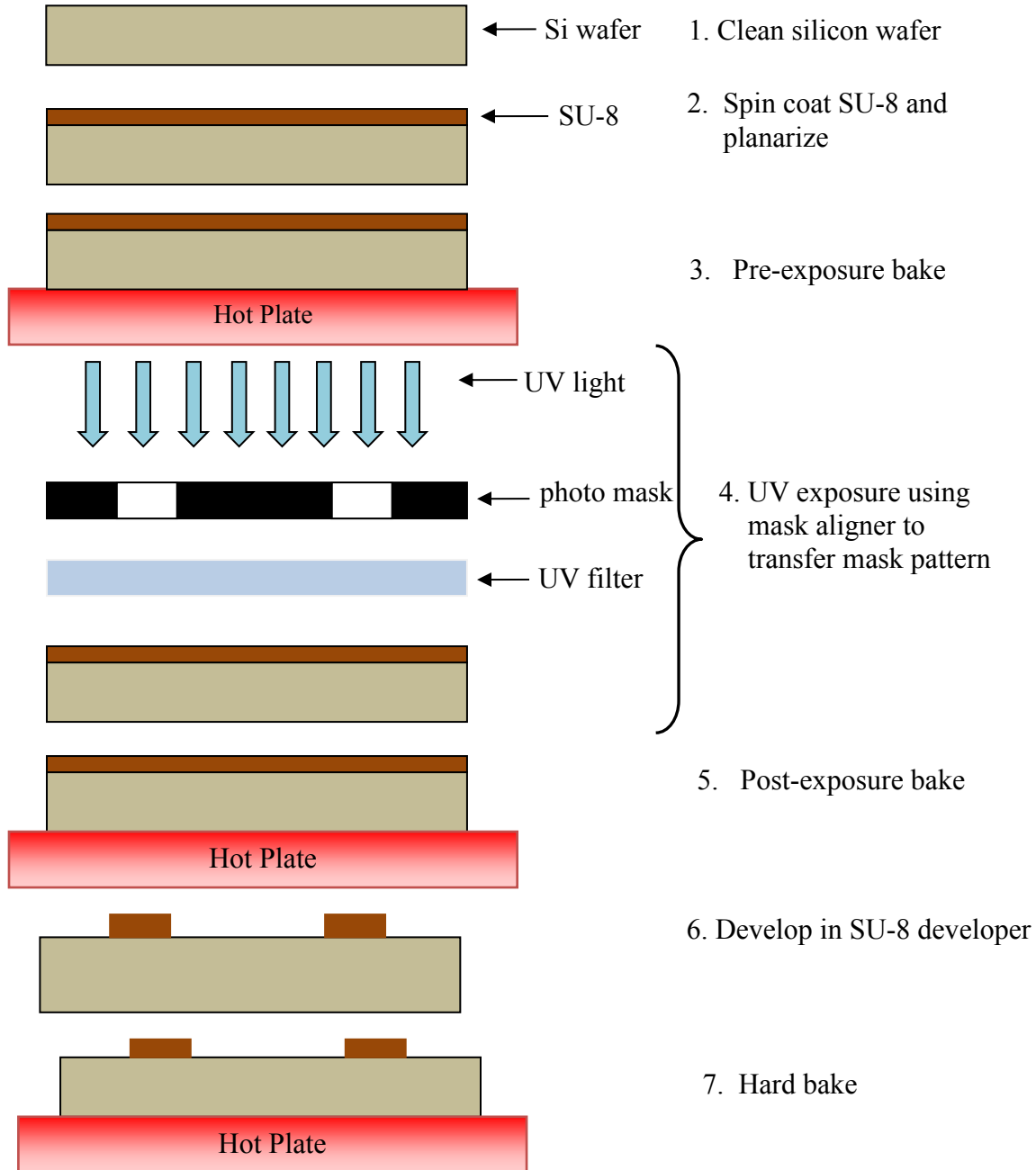


Figure 3.2 Fabrication of SU-8 mold

The details of the processing steps are described in the following sections.

1. A piranha solution was prepared by mixing  $\text{H}_2\text{SO}_4$  with  $\text{H}_2\text{O}_2$  at the ratio 3:1 and heated on a hotplate to a temperature of  $150^\circ\text{C}$ . Afterwards, the silicon wafer for the SU-8 mold was immersed in it for 15 min. Next, the silicon wafer was dump rinsed in DI water followed by spin rinse and drying. The silicon wafer was then placed in a buffered oxide etchant (BOE, HF:  $\text{NH}_4\text{F}$ = 1:6) solution to strip any silicon dioxide on the wafer. The silicon was dump rinsed again in DI water followed by spin rinse and drying. The silicon wafer was placed in an oven for 20 min at  $120^\circ\text{C}$  to remove any moisture on the wafer surface.
2. The cleaned silicon wafer was mounted on the vacuum chuck of the negative resist spin coating system. Then approximately 5 mL of liquid SU-8 2075 (MicroChem Corp., Newton, MA) was dispensed onto the center of the silicon wafer. The wafer was spun at 500 rpm for 10 seconds followed by 2000 rpm for 30 s to obtain a SU-8 thickness of 100  $\mu\text{m}$ . The spin speed and spin time information was obtained from the SU-8 2075 data sheet provided by the vendor. After spin coating the wafer was placed on a flat surface to allow the SU-8 to flow and planarize uniformly across the wafer surface. This step is very important especially with thin silicon wafers which bend because they are pulled at the center when placed on the high vacuum chuck of a spin coater. The absence of edge bead removal during the spin coating step will also require the planarization step.
3. The pre-exposure bake step was performed in two steps, first step at  $65^\circ\text{C}$  for 5 minutes followed by a second bake step at  $95^\circ\text{C}$  for 20 min. These temperatures and timings depend upon the thickness of the SU-8 and can information can be obtained from the data sheet. The hot plate was then turned off to allow the wafer to cool

- down slowly to room temperature. The slow cooling of the wafer is important to prevent resist cracking and possible delamination.
4. The wafer with SU-8 coating was mounted on a Karl Suss Mask aligner and a transparency mask with design pattern was placed and aligned on top of the wafer. In order to obtain vertical side walls in the SU-8 photoresist, a UV filter (PL-360-LP, Omega Optical, Inc., Brattleboro, VT) to filter out UV radiation below 350 nm, was placed between the UV light source and the transparency mask. The UV exposure energy value required for a 100  $\mu\text{m}$  thick SU-8 2075 is 240  $\text{mJ}/\text{cm}^2$  and was obtained from the SU-8 data sheet. The exposure time was calculated based on the intensity of the UV lamp source and was incremented by 20% to account for the presence of the UV filter.
  5. The post-exposure bake was performed on a hotplate in a two-step process to stabilize the transferred pattern and remove any extra solvents. The first bake step was performed at 65°C for 5 min, followed by a second bake step at 95°C for 10 min. The hot plate was then turned off to allow the wafer to cool down slowly to room temperature.
  6. The wafer was immersed in a SU-8 Developer (MicroChem Corp., Newton, MA), developed for 10 min (for 200  $\mu\text{m}$  thick SU-8) and gently moved back and forth to ensure uniform developing. The wafer was rinsed briefly with IPA and blown dry with nitrogen.
  7. The dried wafer is then hard baked on a hot plate at 150°C for a couple of minutes to complete the SU-8 patterning process.



### 3.4 Thick PDMS Casting

The process flow for casting a thick PDMS layer on a SU-mold is shown in Figure 3.3.

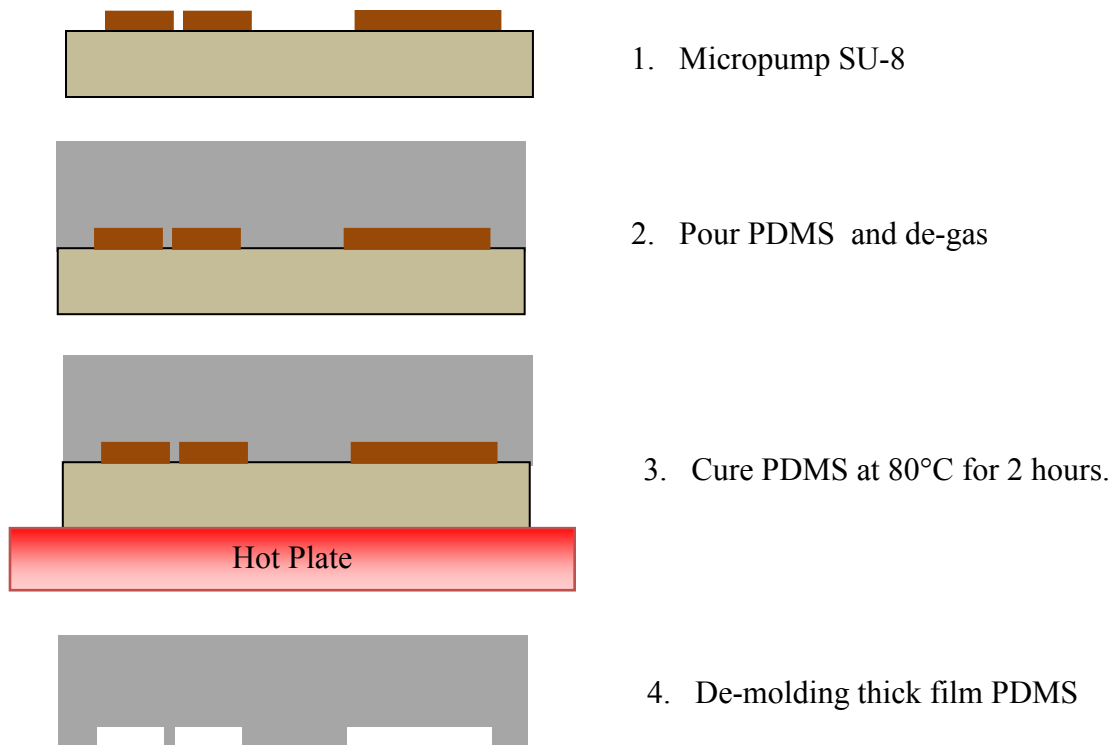


Figure 3.3 Thick PDMS casting process

The details of the thick PDMS casting process are as follows:

1. The PDMS base and curing agent were mixed in a ratio 10:1 by mass in a 2 inch petri dish. The PDMS mixture is left in the open petri dish for 15 min to get rid of the air bubbles. Alternatively, the petri dish with PDMS mixture can be left in a vacuum chamber for a few minutes to degas the air bubbles.

2. For the thick PDMS layer, the PDMS mixture is poured uniformly to cover the wafer with the SU-8 mold to a thickness of approximately 5 mm. Any air bubbles generated while pouring were removed by piercing the bubbles with a syringe needle.
3. The SU-8 mold was then placed on a hot plate at 80°C for 2 hrs.
4. The cured PDMS layer was diced using a razor blade and gently peeled off from the SU-8 mold to obtain the thick PDMS component.

Figure 3.4 (a) shows a typical SU-8 mold for a micropump fluidic layer. Figure 3.4 (b) shows a thick PDMS layer casted by SU-8 mold.

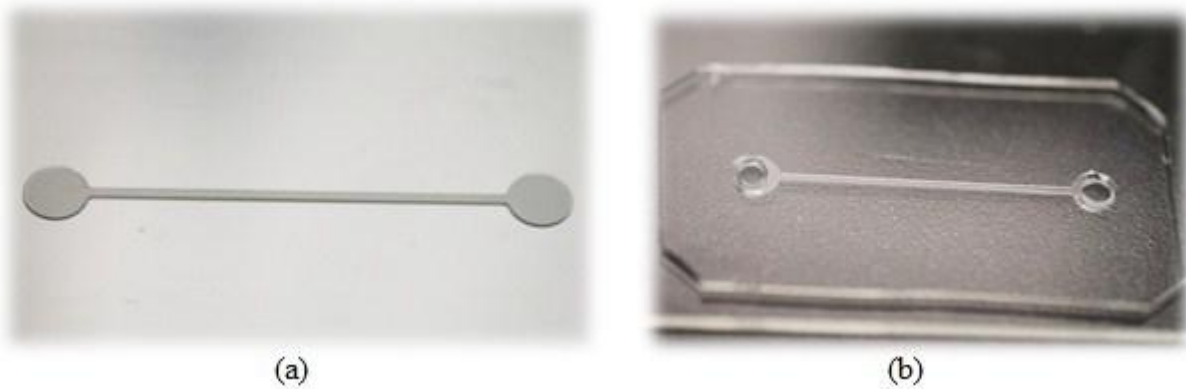


Figure 3.4 (a) Typical SU-8 mold on Si wafer (b) A thick PDMS fluidic layer

### 3.5 Thin PDMS Casting

The process flow for casting a thin PDMS layer on a SU-mold is shown in Figure 3.5.

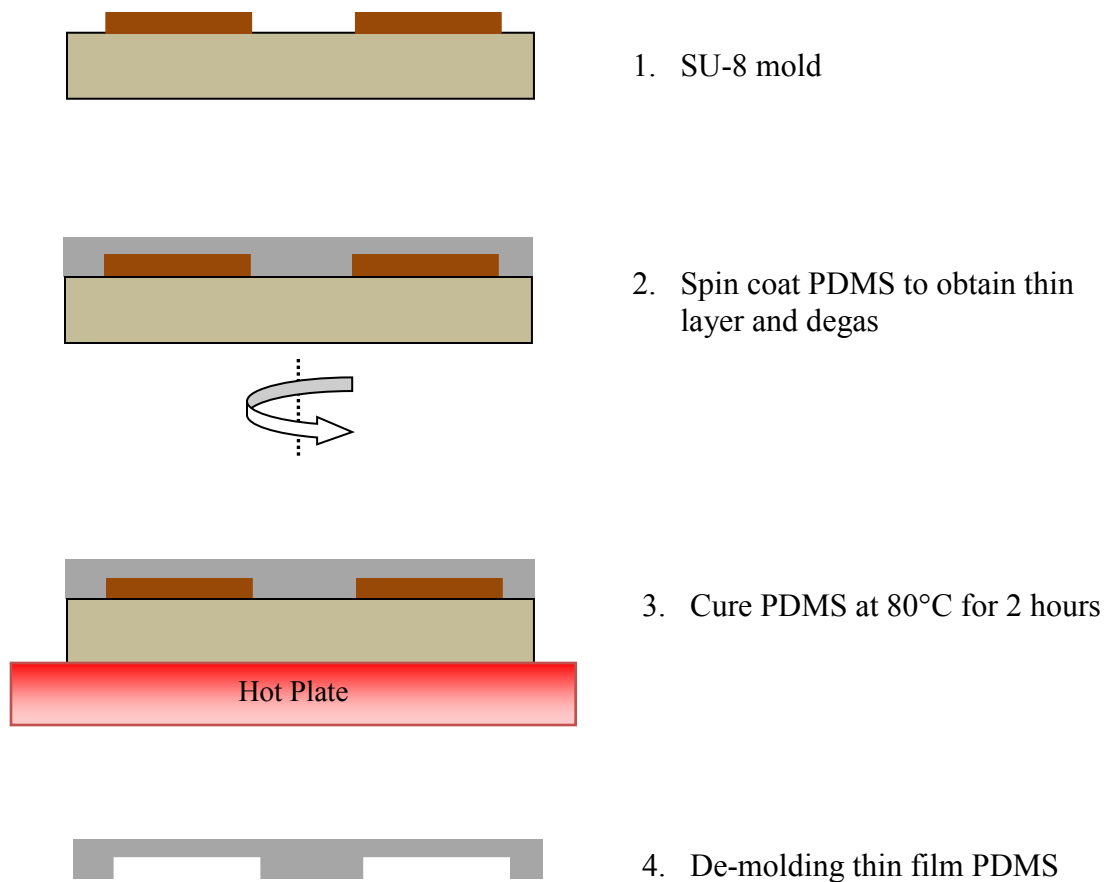


Figure 3.5 Thin PDMS casting process

The details of the thin PDMS casting process are as follows:

1. PDMS mixture was prepared as described in the previous section.
2. For the thin PDMS layers with membranes, the PDMS mixture was spin coated on the SU-8 mold at 450 rpm for 1 min to obtain a 100  $\mu\text{m}$  thick PDMS membrane. The required spin speed was determined from the spin speed vs. thickness plot [163] as shown in Figure 3.6.

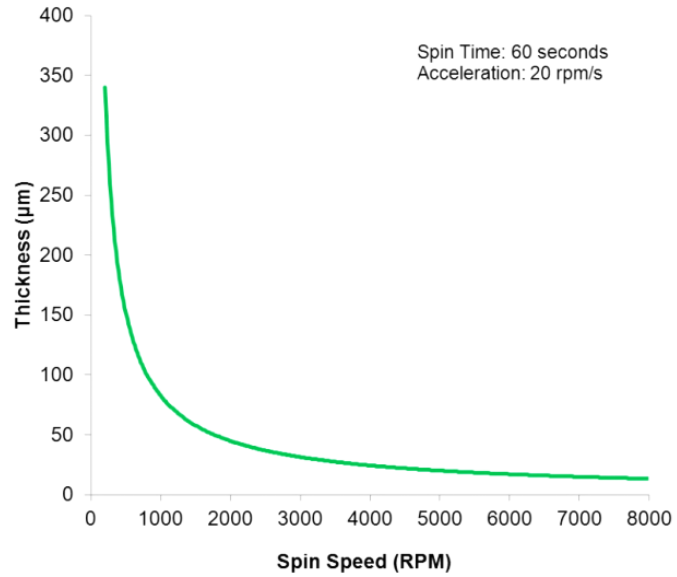


Figure 3.6 PDMS thickness as a function of spin speed

3. The SU-8 mold was then placed on a hot plate at 80°C for 2 hrs.
4. The cured PDMS layer was diced using a razor blade and gently peeled off from the SU-8 mold to obtain the thin PDMS component.

Figure 3.7 (a) shows a typical SU-8 mold for a thin PDMS control layer. Figure 3.7 (b) shows a thin PDMS layer casted by SU-8 mold.



Figure 3.7 (a) SU-8 mold on Si wafer for thin PDMS control layer (b) A thin PDMS control layer

### 3.6 Oxygen Plasma Bonding

The bonding of a PDMS layer to another PDMS layer or a PDMS layer to a glass substrate was achieved by oxygen plasma treatment of the bonding surfaces. The PDMS thin layer was first bonded to a glass slide which provides mechanical support. The PDMS thick layer was then bonded to the PDMS thin layer. A glass slide was then bonded to the PDMS thick layer. Figure 3.8 shows the process flow for assembling the device.

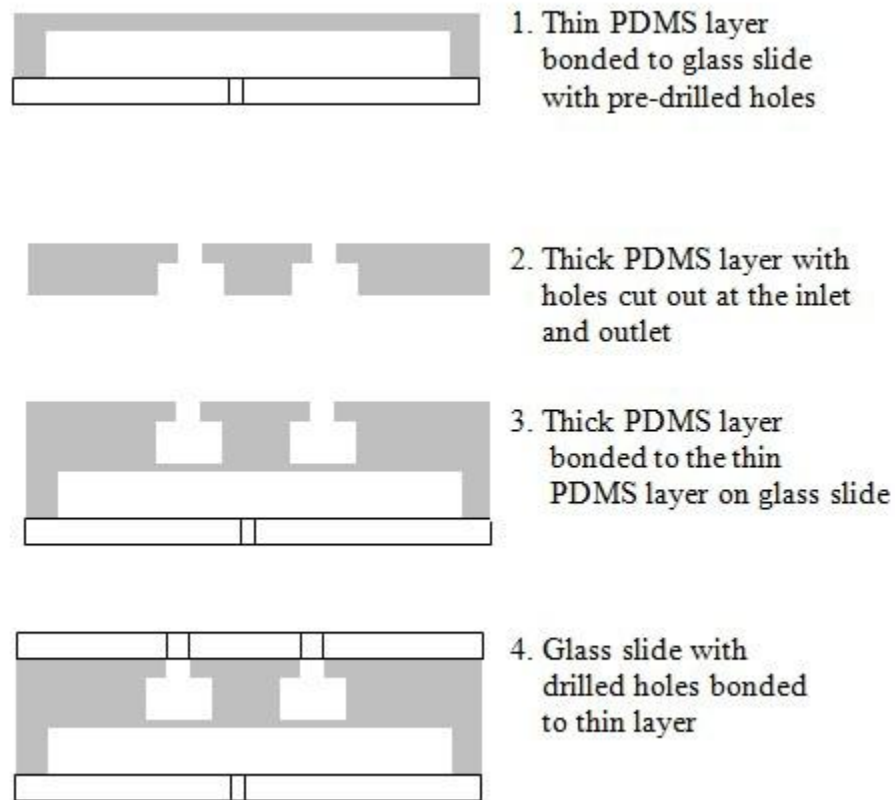


Figure 3.8 Process flow for assembling the device

The oxygen plasma bonding steps are as described below:

1. An abrasive diamond grinding mandrel (1.5 mm diameter, Wale Apparatus Inc., Hellertown, PA) was used to drill holes in the glass slides (75x38 mm, 1 mm

thick, Electron Microscopy Sciences, Hatfield, PA) for providing access to the inlets and outlets of the microchannels in the PDMS layer. The glass slides with drilled holes were cleaned using a Piranha solution to remove any organic contaminants, rinsed in DI water and blow dried with nitrogen. A 1.5 mm tip diameter micro coring tool (Harris uni-core, Ted Pella, Inc. Redding, CA) was used to punch holes in the PDMS layers at the microchannel inlet and outlet. The glass slide and the thin PDMS layer were placed inside the Oxygen plasma chamber (Model PC-150, South Bay Technology, Inc., San Clemente, CA) with their bonding sides facing up. The plasma chamber was operated at 20 W, 105 mTorr for 20 s. The exposure to oxygen plasma causes oxidation of the CH<sub>3</sub> groups on the PDMS surface to produce OH groups [164]. The –OH functional groups on the PDMS surface enable bonding to another PDMS surface or glass. The oxygen plasma treatment also temporarily makes the hydrophobic PDMS surface to a hydrophilic surface. The plasma treated PDMS layer was held by a pair of tweezers at the opposite corners, aligned and brought in contact with the glass slide on one edge of the glass slide first. The PDMS layer was then gently rolled on top of the glass slide to complete the bonding as shown in Figure 3.9. This rolling action reduces the trapping of air between the bonded layers and leads to a uniform bonding. The bonding process has to be completed within 3 minutes of exposure to oxygen plasma in order to ensure complete bonding.

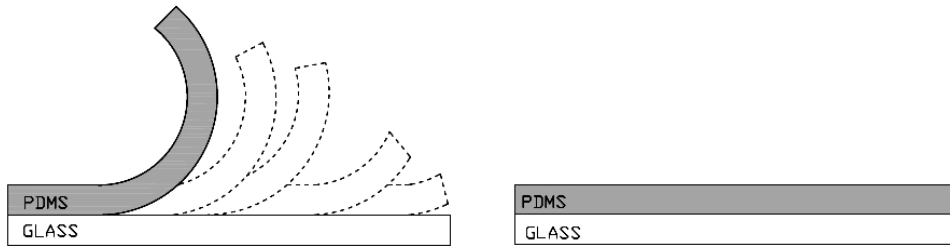


Figure 3.9 Roll PDMS layer to obtain uniform bonding

2. A 1.5 mm tip diameter micro coring tool was used to punch holes in the thick PDMS layers at the microchannel inlet and outlet.
3. A similar procedure as described in Step 1 was repeated to bond the thick PDMS layer to the thin PDMS layers.
4. A glass slide was then bonded to the thick PDMS layer to complete the oxygen plasma bonding process for the device. The assembled device was then packaged with fluidic connectors and tubing to obtain the final device.

Figure 3.10(a) shows typical thick and thin PDMS layers of a micropump assembled together and Figure 3.10(b) shows a close view of the alignment of the air chambers on top of the microchannel.

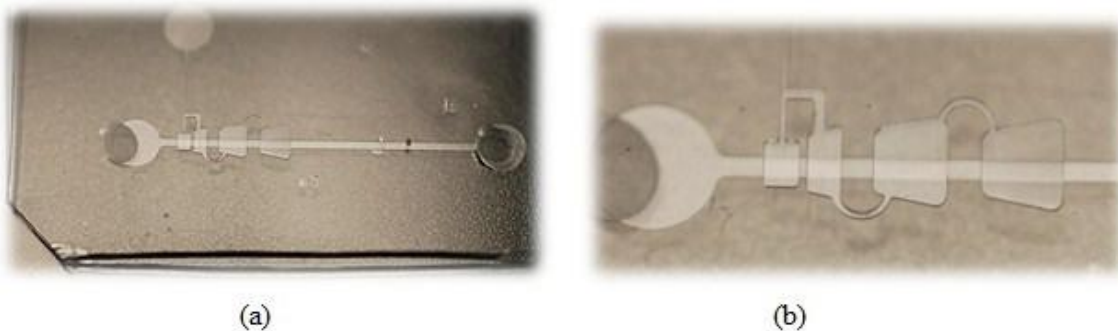


Figure 3.10 Thick and thin PDMS layers of a micropump bonded together (b) A close view of the alignment of the air chambers over the microchannel

### 3.7 Fabrication of IDE

Figure 3.11 shows the process flow for fabrication of the IDE.

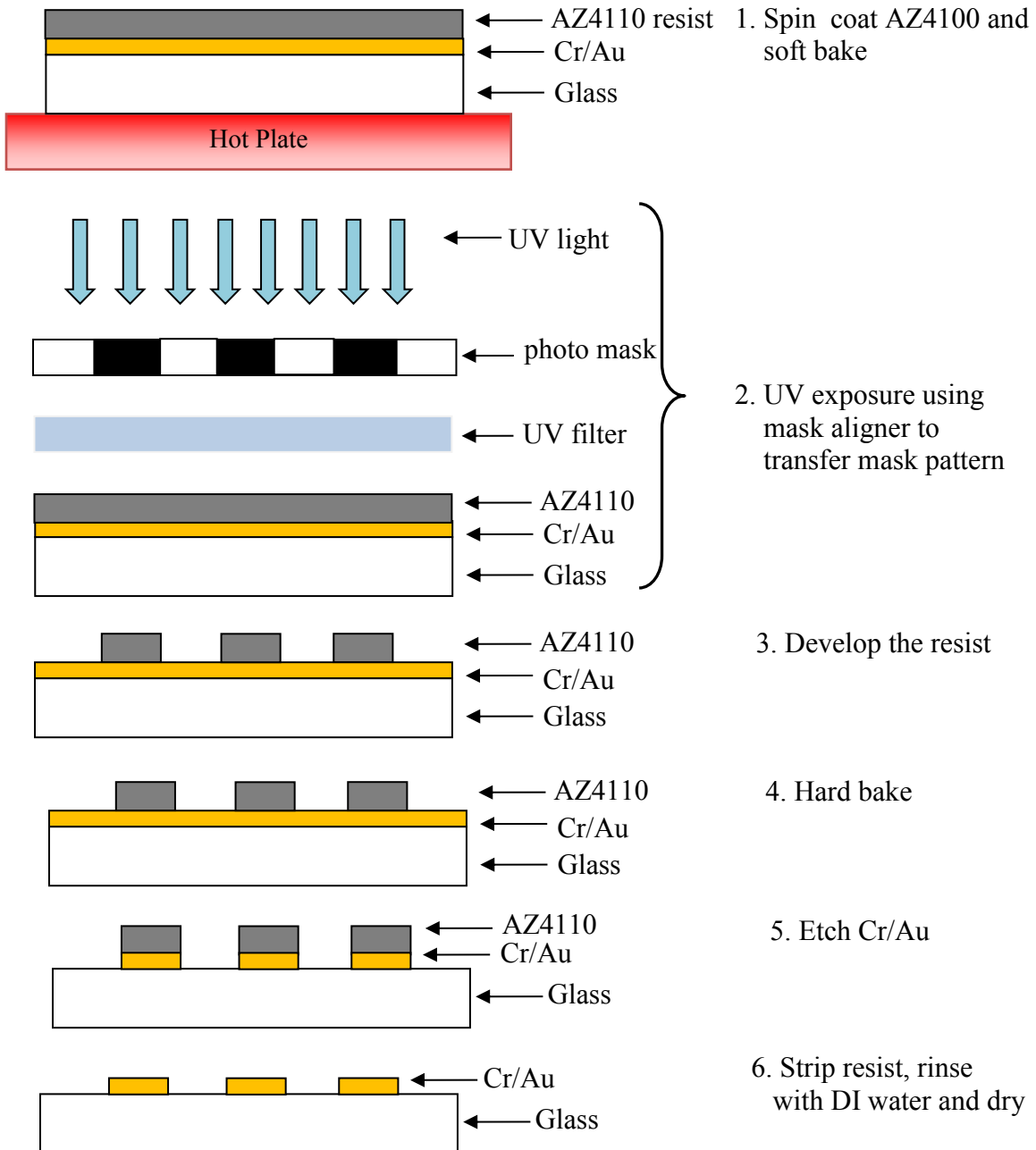


Figure 3.11 Fabrication steps for IDE



The AutoCAD designs were sent to Advance Reproductions (North Andover, MA) where transparency photo masks with a ¼ mil resolution were manufactured. The transparency photo mask is suitable for designs at a resolution limit of about 15 µm. The wafers used were 500 µm thick, 5 in. Glaverbel float soda lime glass wafers (Precision Glass and Optics, Santa Ana, CA).

The details of the processing steps are as described below.

1. The wafers were cleaned in a Piranha solution, rinsed in DI water and spin dried. The cleaned wafers were then sputtered with Cr/Au (250Å/5000Å, UHV Sputtering, Inc., Morgan Hill, CA). The glass wafers with Cr/Au were rinsed with Acetone, rinsed in DI water and spin dried. The wafers were then left in an oven at 120°C to dry the wafer surface. The cleaned wafers were spin coated with a 1.25 µm thick layer of AZ4110 photoresist. After the spin coating, the resist may contain up to 15% solvent and may have built-in stress. To remove the solvent and reduce the stress, the spin coated resist was soft baked at 110°C for 4 min.
2. Following this, a Karl Suss mask aligner was used to align and expose the resist coated wafer to transfer the pattern from the photomask onto the photoresist.
3. Afterwards a development process was used to selectively dissolve the photoresist. AZ4110. Following development, the wafer was examined visually to ensure that the development process was complete. A final inspection was made under a microscope to ensure that the pattern obtained was as expected.
4. Hard bake or post bake removes any residual developer solution and also anneals the photoresist to promote the interfacial adhesion of the photoresist weakened by developer entering the resist-wafer interface. Hard baking also improves the hardness

of the film which is required during further etching steps. The hard bake was carried out by placing the wafer in an oven at 120°C for 15 min.

5. The wafer was immersed in a gold etchant solution (gold etchant TFA, Transene, Inc, Danvers, MA) to remove the gold from the exposed regions on the wafer. The etch rate was 28Å/second at 25°C when the etchant was fresh. This was followed by a Cr etch using the chromium etchant (1020AC, Transene, Inc.) to remove the chrome layer. The etch rate was 32Å/s at 40°C.
6. The etched wafers were rinsed with DI water and spin dried.

Figure 3.12 shows a typical IDE chip with holes drilled for access to the inlet and outlet of the fluidic layer microchannel. Also shown is a close view of the IDE fingers with 10 μm width and spacing.

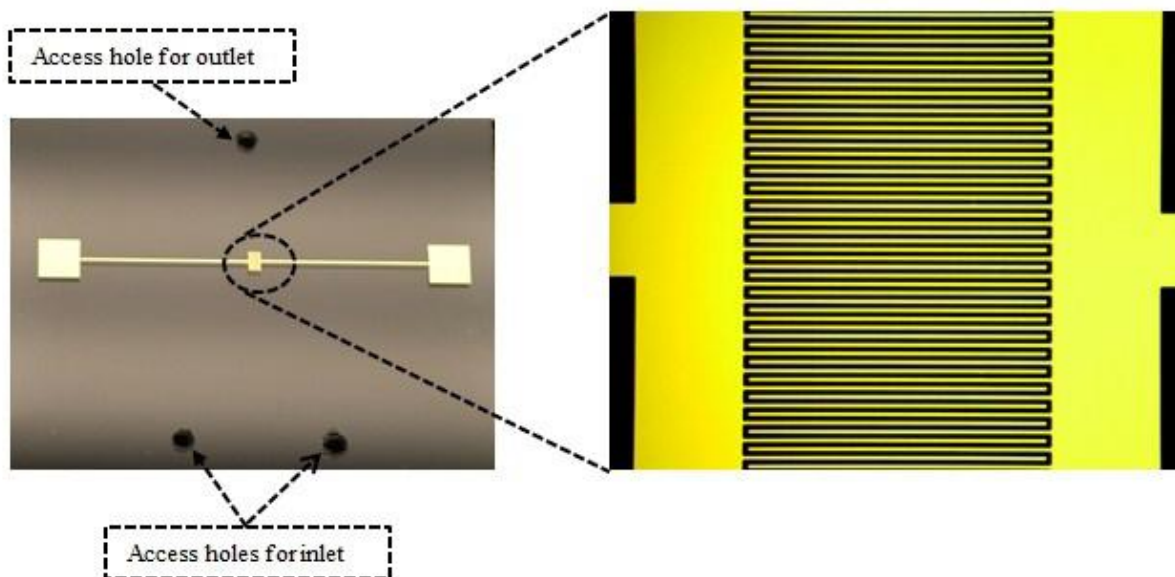


Figure 3.12 A typical IDE chip with a close view of the IDE fingers

### 3.7.1 PDMS bonding with IDE

The etched wafers were then diced using a wafer dicing machine to obtain the individual electrode chips. Figure 3.13 shows the process flow.

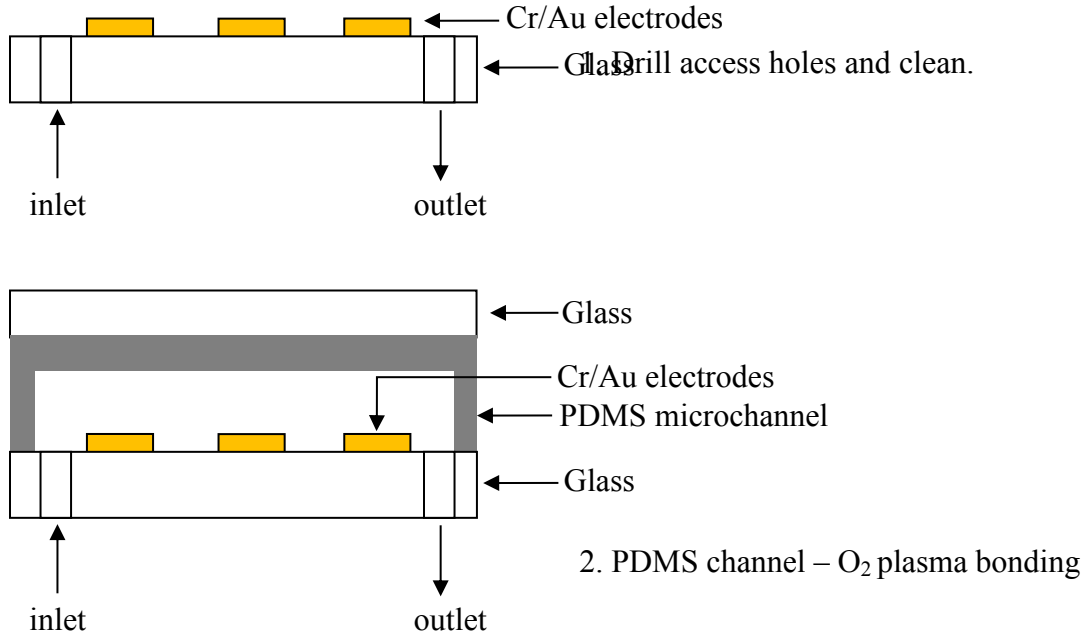


Figure 3.13 PDMS bonding to IDE

The details of the processing steps are as described below:

1. An abrasive diamond grinding mandrel was used to drill holes in the electrode chip to provide inlet and outlet access. The electrode chips were rinsed in DI water and blow dried with Nitrogen to remove the glass debris produced during the drilling process. The electrode chips were then rinsed in Acetone and blow dried with Nitrogen. A PDMS microchannel was bonded to the electrode chip by using oxygen plasma bonding method as described in the previous section.

2. A glass layer was bonded to the PDMS layer to provide mechanical stability.

### 3.8 PDMS – Glass Thermal Bonding

An alternate method to oxygen plasma bonding is thermal bonding. Thermal bonding provides a temporary bond unlike the permanent bond achieved through oxygen plasma bonding. Figure 3.14 shows the process flow for PDMS-Glass thermal bonding.

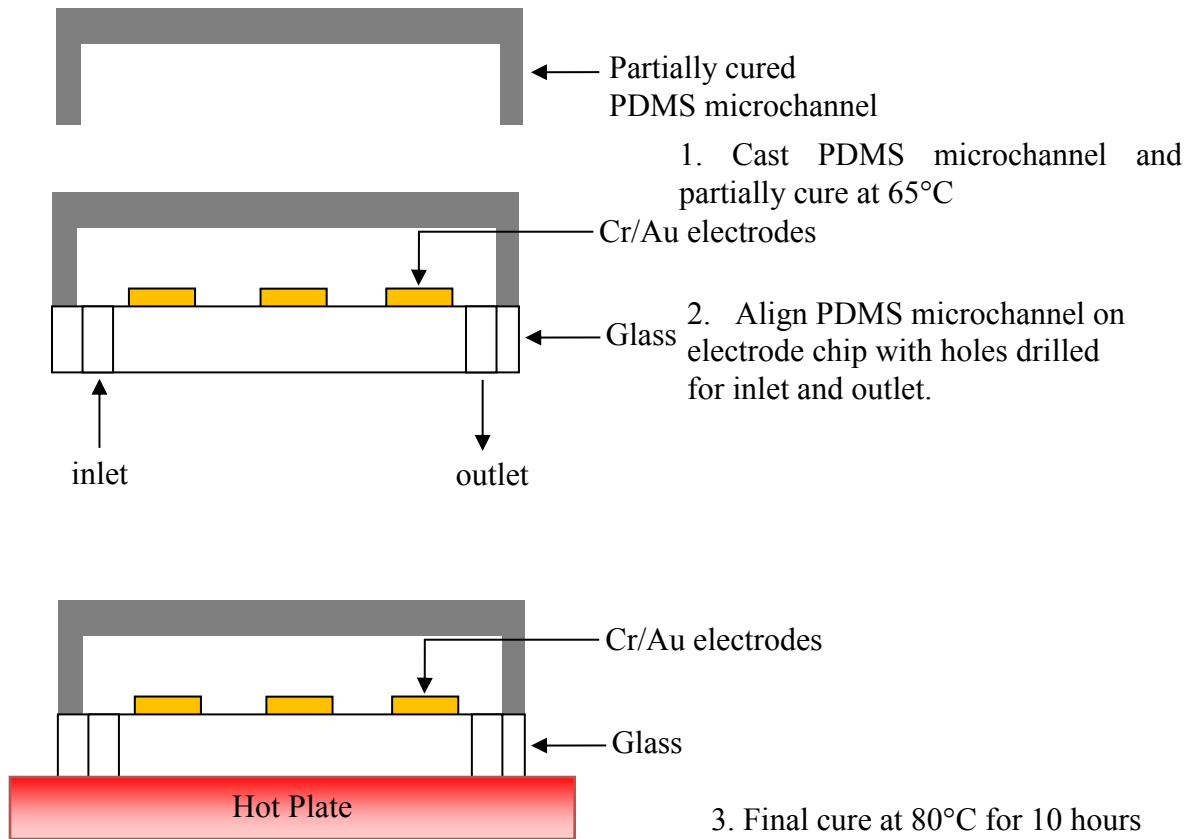


Figure 3.14 PDMS – Glass thermal bonding process

The details of the processing steps are as described below:

1. The PDMS microchannels were casted on a SU-8 mold as described in the previous sections. The PDMS layer was first partially cured at 65°C for 45 min.

2. An abrasive diamond grinding mandrel was used to drill holes in the electrode chip to provide access to the inlet and outlets of the PDMS microchannel. The electrode chips were rinsed in DI water to remove the glass debris produced during the drilling process. The electrode chips were then rinsed in acetone to remove the photoresist. After the acetone rinse most of the photoresist from the electrode surface is removed. To further clean the electrode surface, a soft cotton swab dipped in acetone was used to gently clean the electrodes without scratching the gold surface. The partially cured PDMS is peeled off the SU-8 mold, aligned with electrode chip and aligned on top of the electrode chip.
3. The electrode chip with PDMS is then place on a hot plate at 80°C for 10 hrs to completely cure the PDMS layer. After the final curing, a glass slide is attached to the exposed back side of the PDMS channel to provide mechanical support.

The thermal bonding method, unlike the oxygen plasma treatment bonding method, is reversible. Therefore, the PDMS layer can be removed and replaced with a fresh PDMS layer when PDMS surface is contaminated after repeated use or when it is required to clean the electrode surface.

### **3.9 Fully Integrated Microfluidic System**

Figure 3.15 shows a fully integrated microfluidic system. Figure 3.16 shows a close view of the micropump and micromixer from the fully integrated microfluidic system shown in Figure 3.15.

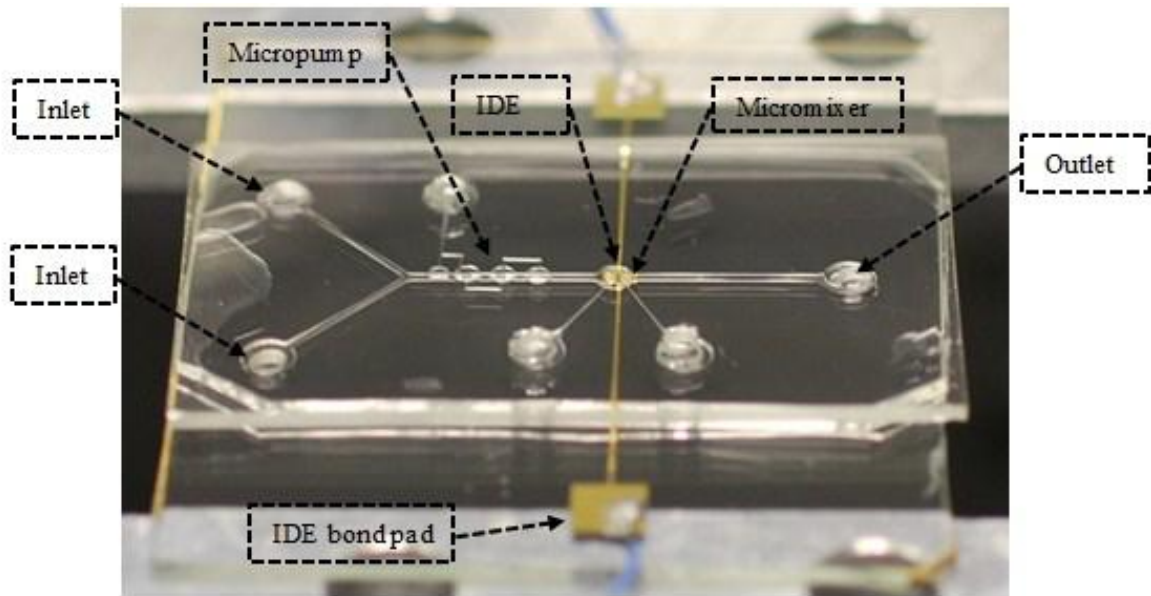


Figure 3.15 A fully integrated microfluidic system

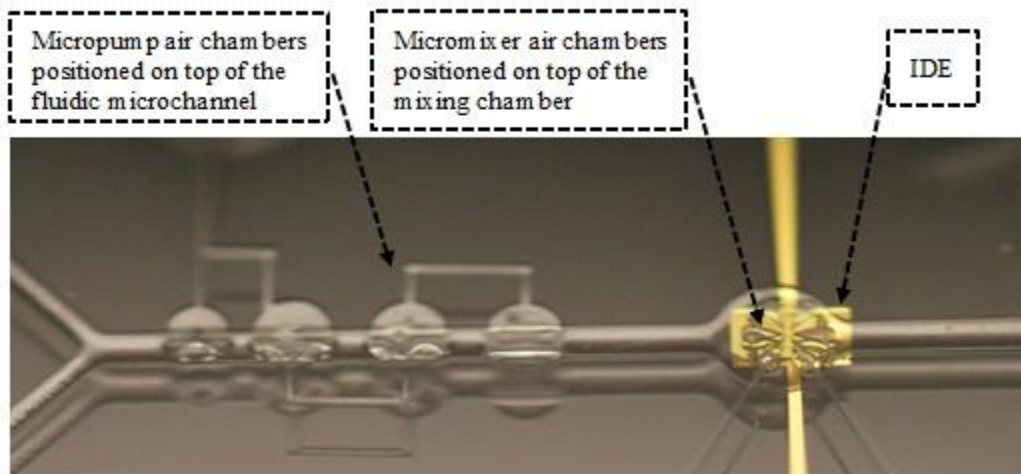


Figure 3.16 A close view of the various components on the fully integrated system

## 4. EXPERIMENTAL SETUP AND TESTING

The following sections describe the material selection and design of experimental methods used to test the various microfluidic system components used in this study. The focus will be on individual testing of various microfluidic components and the integration of various components to achieve a fully integrated microfluidic system.

### 4.1 Surface Modification of PDMS

The use of PDMS for microfluidic devices has many advantages as discussed in the previous section. However, PDMS has a hydrophobic surface and tends to adsorb organic macromolecules such as protein and causes non-specific protein adsorption which can interfere with biological applications performed within a PDMS microfluidic system [165]. The hydrophobic surface of PDMS also leads to formation of air bubbles within a PDMS microchannel. One of the methods commonly used to modify the hydrophobic surface of PDMS by exposure to oxygen plasma. An exposure to oxygen plasma oxidizes the surface of the PDMS and makes it hydrophilic. However, when exposed to air later, the hydrophobic surface recovers with time. With oxygen plasma treatment, a useful lifetime for quantitative electrophoresis is 3 hrs [166]. In the present study, the PDMS surfaces were treated with Pluronic F108 surfactant (#F018, BASF, Florham Park, New Jersey) to modify the PDMS surface to make it hydrophilic and reduce non-specific protein adsorption. Pluronic belongs to a group of triblock copolymers with poly(propylene oxide) (PPO) centers with poly(ethylene oxide) (PEO) side chains with the general composition of  $(PEO)_m(PPO)_n(PEO)_m$ , which has been proven to have extremely low toxicity and immunogenic response and is widely used in many biotechnological applications [167]. In this approach, the PDMS microchannels were filled with Pluronic F108 surfactant solution and allowed to incubate for at least 1 hour. The concentration of Pluronic F108 solution used was 1%

weight in water, prepared by mixing 1 g of Pluronic F108 in 100 mL of DI water. This surface modification reduced the hydrophobic forces and enhanced the fluid movement through the microchannels. The surface modification also reduced the formation of air bubbles within the microfluidic channels. The surface modification lasted for a few days when compared to oxygen plasma treatment method with a lifetime of only 3 hrs.

#### **4.2 Micropump Performance Testing**

The control system for operating the micropump consists of a mini air compressor (BTC-IIS, part# D730A-23-01, Hargraves, Mooresville, NC) to supply compressed air and a 3-port ultra-miniature solenoid valve (S070C-5BG-32, SMC Pneumatics, Noblesville, IN) to control the supply of compressed air. Figure 4.1 shows the mini air compressor and 3-port ultra-miniature solenoid valves used. A pressure regulator with a gauge was used to regulate the compressed air supply to the micropump. The mini air compressor is 3 x 3 x 1 in size and weighs only 170 grams. The ultra-miniature solenoid valve is 7 x 30 x 11 mm in size and weighs only 5 g. Both the mini air compressor and the solenoid valve are compact, lightweight and these are desirable characteristics for portable devices. A DC power supply was used to power the mini air compressor with a voltage of 24 V DC. A function generator (HP 3325B) was used to power the solenoid valve with a square wave form AC signal of 12 V peak to peak with 6V DC offset. The outlet of the micropump was connected to tubing with 1/8" ID. Figure 4.2 shows a schematic of the experimental setup layout for micropump performance testing.





Figure 4.1 (a) 3-port ultra-miniature solenoid valve (SMC part# S070C-5BG-32) (b) Mini Air Compressor (Hargraves part# D730A-23-01)

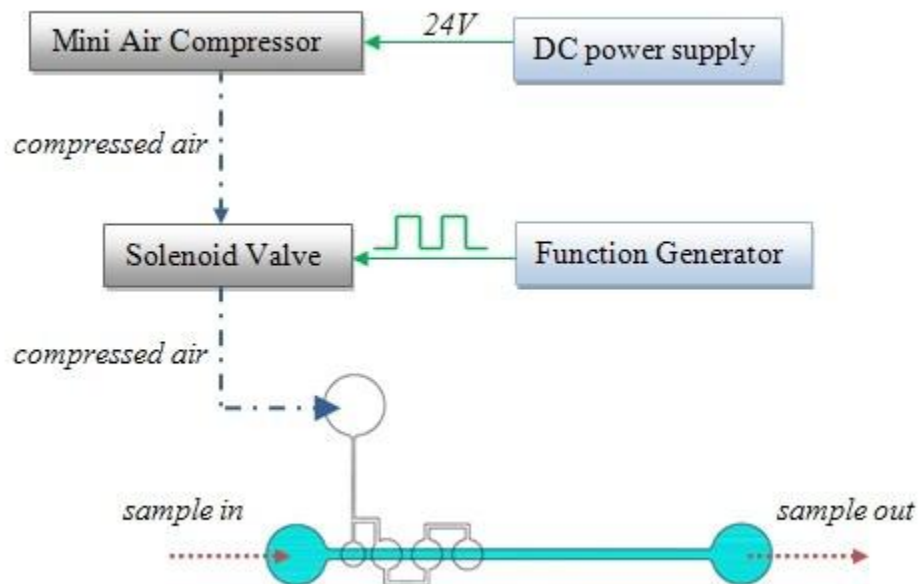


Figure 4.2 Schematic of experimental setup layout for micropump performance testing

The two main control parameters that affect the performance of the micropump are the pressure of the compressed air and the actuation frequency of the solenoid valve. The micropumps were tested with three compressed air pressures, 10, 20 and 30 psi. For each pressure, the frequency of operation of the solenoid valve was varied and six frequencies were used, namely, 5, 10, 15, 20, 25 and 30 Hz. Figure 4.3 shows the experimental setup on an optical table for micropump

performance testing. Figure 4.4 shows the test fixture with various components. Figure 4.5 shows the various tubing connections on the 3-port solenoid valve. The microfluidic channel of the micropump was first treated with Pluronic F108 solution for 2 hrs. The micropump was then primed with DI water and the initial position of the water front in the outlet tubing was noted on the ruler placed next to the tubing. Figure 4.6 shows the micropump clamped on the test fixture. The micropump was operated for 3 minutes and the final position of the water front within the outlet tubing was noted on a ruler. Figure 4.7 shows the initial and final positions of the DI water front (shown with a green dye for better visibility). The change in position of the water front within the tubing ( $\Delta L$ ) was used to compute the volume of the fluid displaced ( $\Delta L \times$  cross-sectional area of tube based on inner diameter) by the micropump. All three micropump designs were tested using this method.

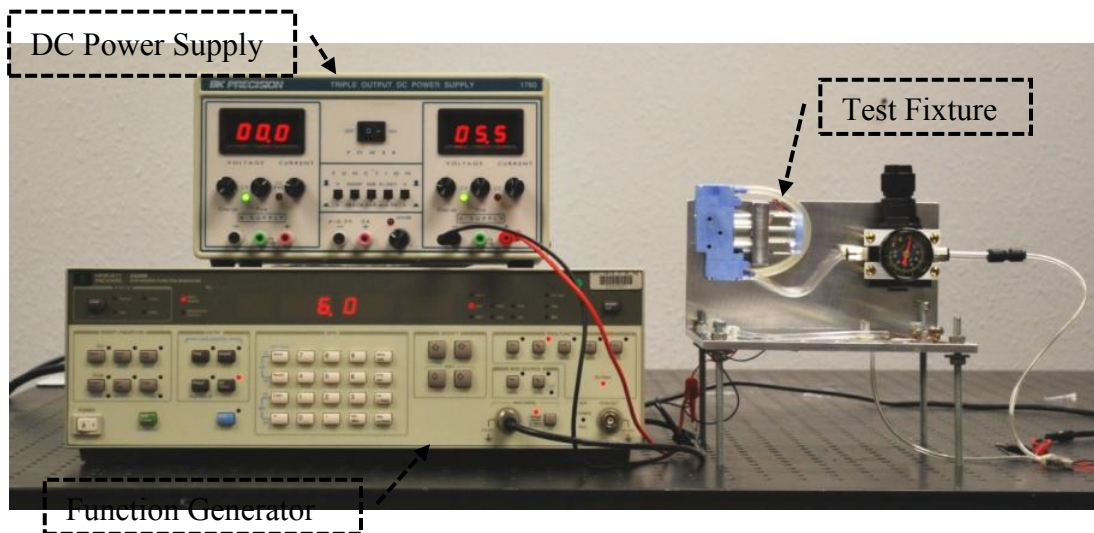


Figure 4.3 Experimental setup for micropump performance testing

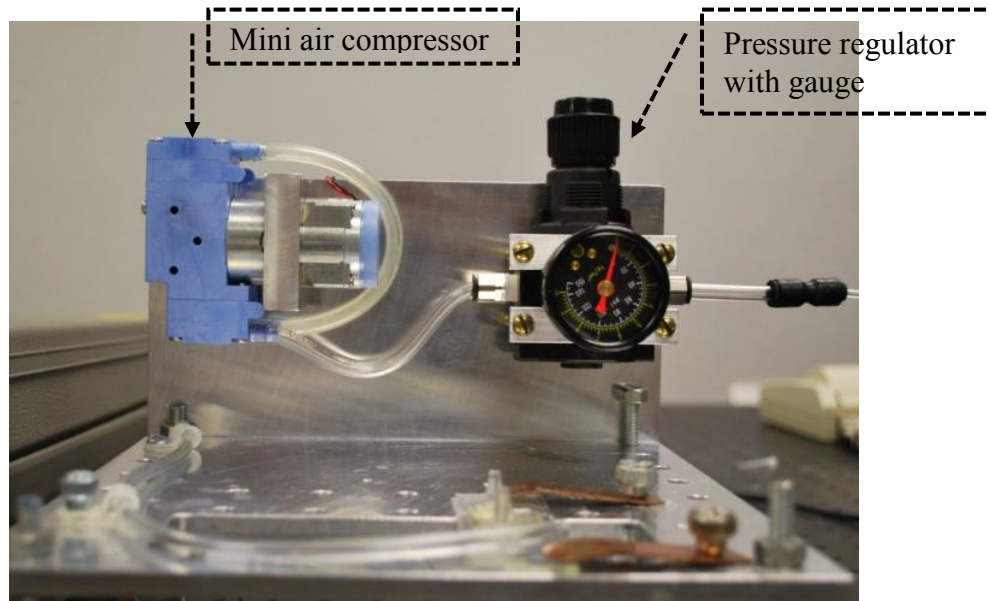


Figure 4.4 Test fixture for micropump testing with various components

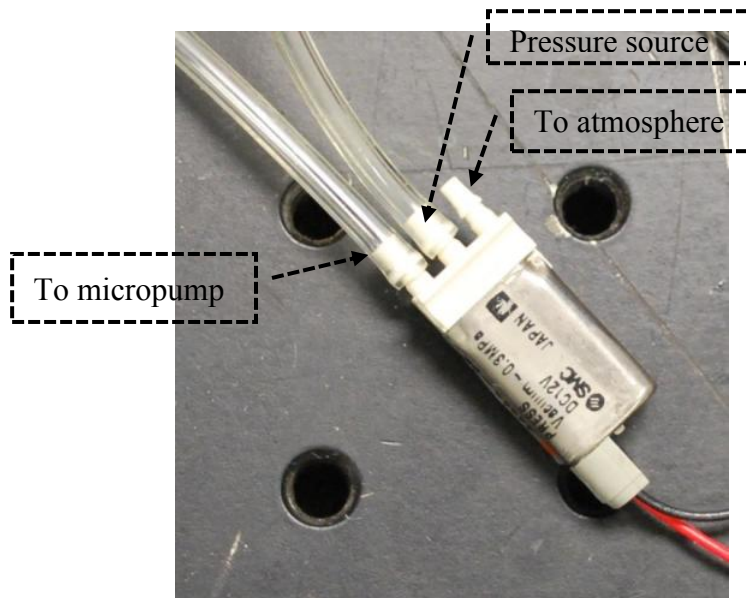


Figure 4.5 3-port solenoid valve with tubing connected to pressure source and micropump

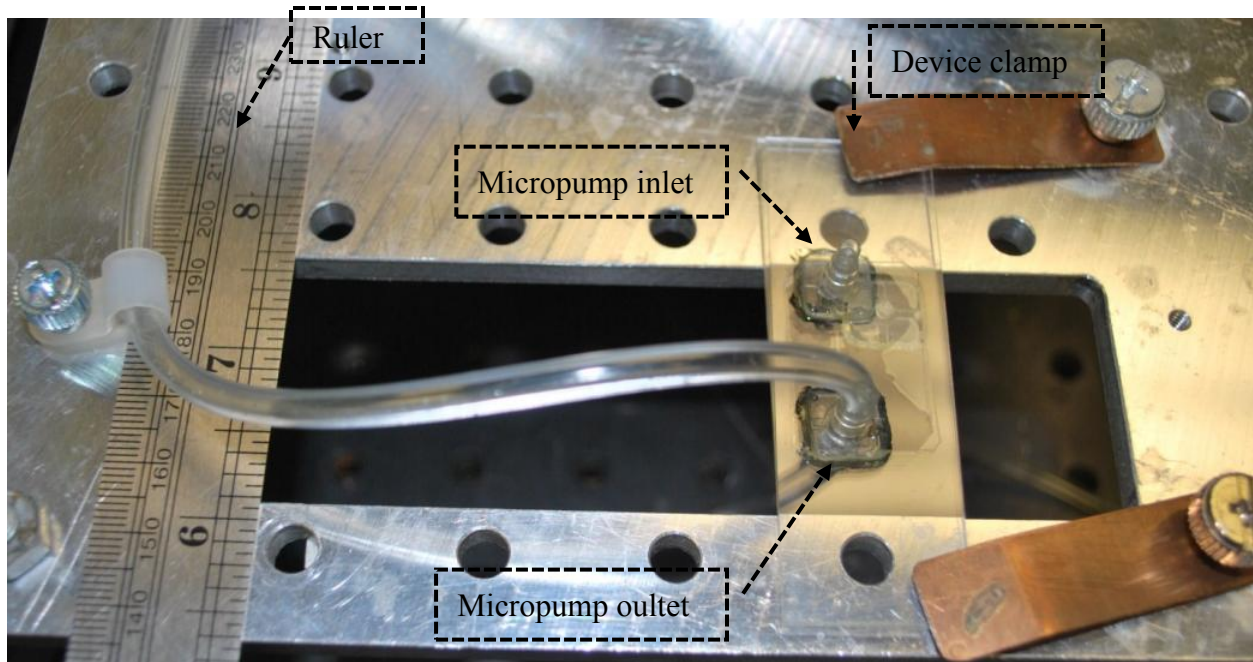


Figure 4.6 A micropump clamped on the test fixture

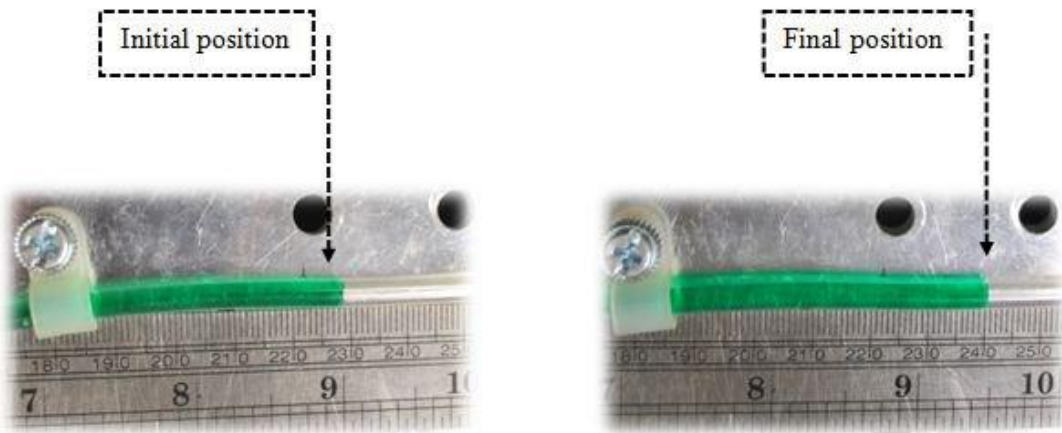


Figure 4.7 (a) Initial position of DI water front (b) Final position of DI water front

### 4.3 Micromixer Performance Testing

The experimental setup layout for micromixer performance testing is very similar to that of the micropump. The micromixer fluidic layer has two inlets to the mixing chamber and one outlet for collecting the mixed sample. Three micromixer designs were tested and the performances of the micromixers are investigated with respect to actuation frequency of the solenoid valve and



sample flow rate. Figure 4.8 shows a schematic of the experimental setup layout for micromixer performance testing. Figure 4.9 shows the experimental set up on an optical table for micromixer performance testing.

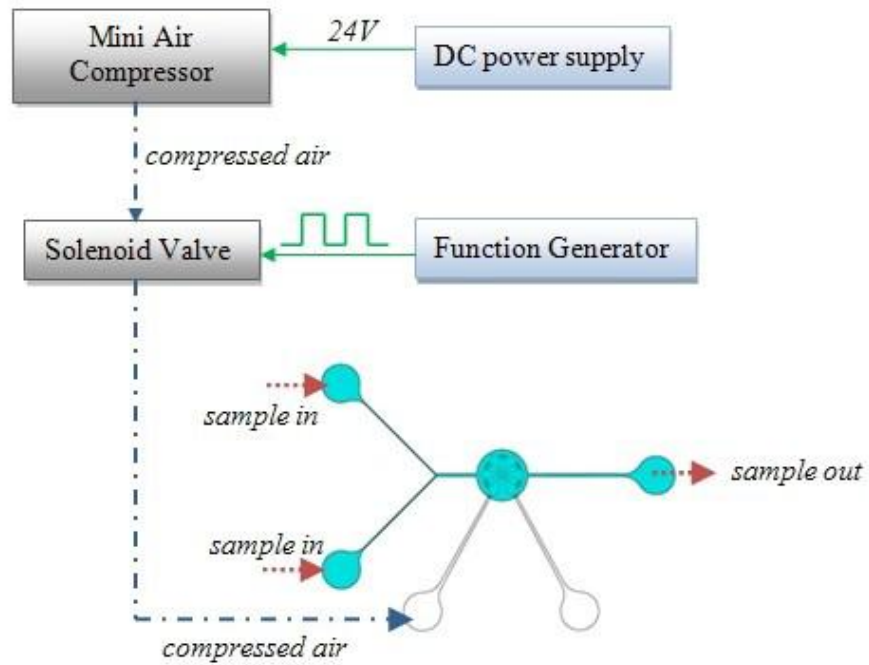


Figure 4.8 Schematic of an experimental setup layout for micromixer performance testing

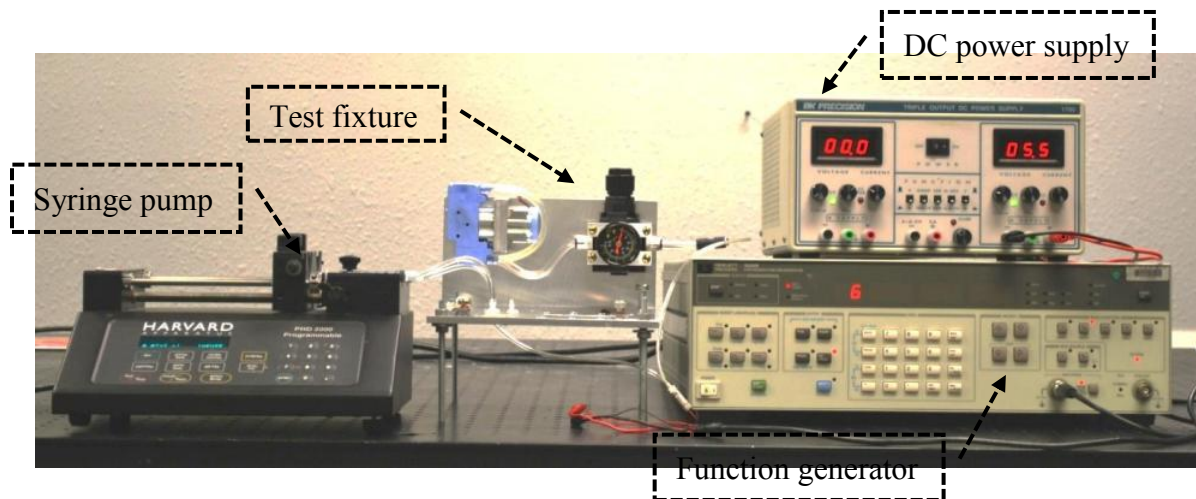


Figure 4.9 Experimental setup for micromixer performance testing

Figure 4.10 shows a test fixture with various components. Figure 4.11 shows a micromixer clamped on the test fixture.

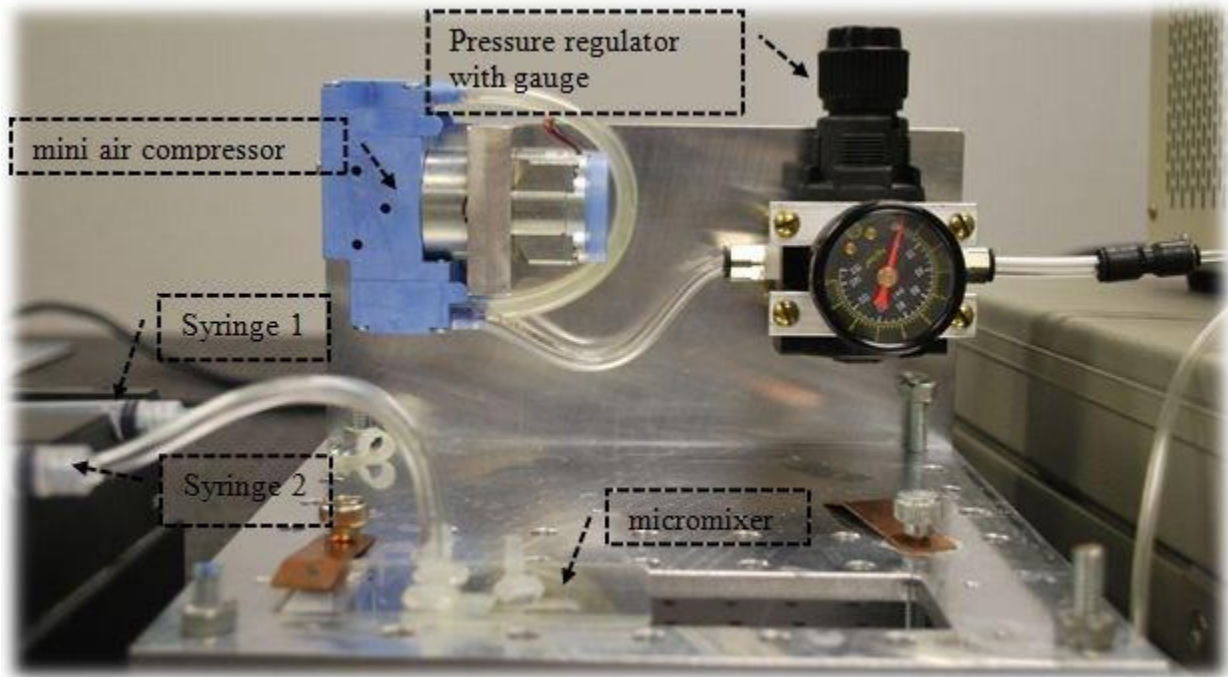


Figure 4.10 Test fixture with various components

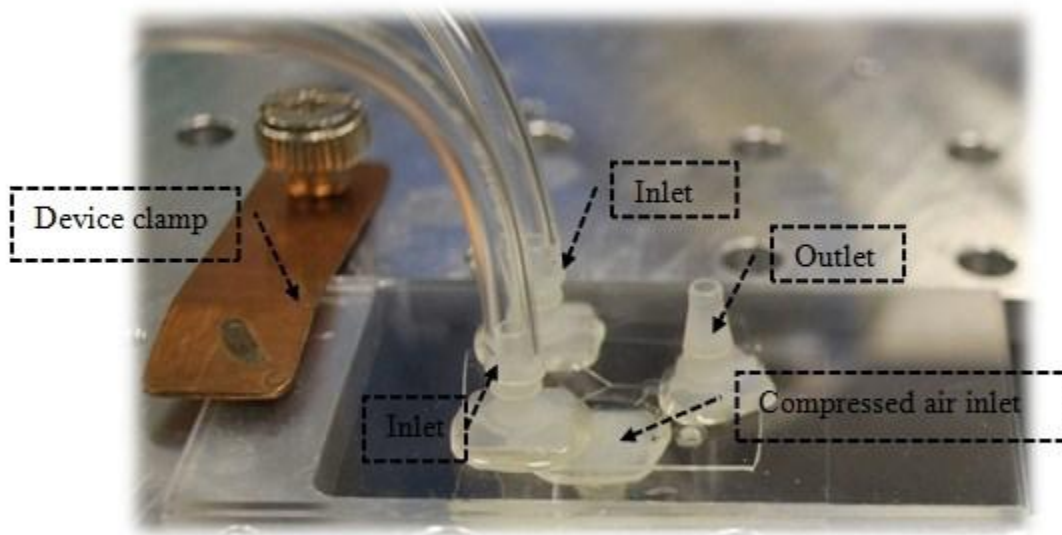


Figure 4.11 Micromixer clamped on the test fixture

### 4.3.1 Materials

Streptavidin-biotin conjugation reactions were used to characterize the mixers' performance and also test the fully integrated microfluidic system. BCF microbeads (Catalog# 24173-1, Fluoresbrite® Yellow Green fluorescent 2.0  $\mu\text{m}$  diameter,  $2.41 \times 10^9$  beads/mL) were purchased from Polysciences, Inc (Warrington, PA). The fluorescent yellow green BCF beads have an excitation maximum wavelength of 441 nm and an emission maximum wavelength of 486 nm, similar to FITC. SCP microbeads (Dynabeads® M-270 Streptavidin, 2.8  $\mu\text{m}$  diameter,  $6.7 \times 10^8$  beads/mL, Catalog# 653-05) were purchased from Life Technologies (Grand Island, NY)

### 4.3.2 Sample Preparation

A 150  $\mu\text{L}$  sample of BCF microbeads was dispensed into a microcentrifuge tube and centrifuged at 10,000G for 5 min in a table top centrifuge. The supernatant was then removed and discarded. The BCF microbeads were resuspended in phosphate buffered saline (PBS) with pH 7.4. This step was repeated three times to wash the BCF beads. After the last wash, a 1.5 mL BCF sample was prepared by mixing 150  $\mu\text{L}$  of BCF beads with 1350  $\mu\text{L}$  of PBS buffer. At this dilution, the number of BCF microbeads was calculated to be  $2.4 \times 10^8$  microbeads/mL. A 100  $\mu\text{L}$  of SCP microbeads was mixed with 1400  $\mu\text{L}$  of PBS in a microcentrifuge tube and placed in a magnetic separation stand (MagneSphere®, Promega Corp., Madison, WI) for 2 minutes. After 2 minutes the supernatant was aspirated with a pipette while the microcentrifuge tube was still held in the magnetic separation stand. The microcentrifuge tube was then removed from the magnetic separation stand and 1500  $\mu\text{L}$  of PBS buffer was added along the inside of the microcentrifuge tube where the microbeads are collected. The washing procedure was repeated three times. At this dilution, the number of SCP beads was calculated to be  $4.5 \times 10^7$  microbeads/mL.

Streptavidin is a tetramer with four binding sites. The ratio of BCF microbeads to SCP microbeads is 5.4 and this ensures that the SCP microbead binding sites for biotin are saturated.

### **4.3.3 Micromixer and Table Top Mixer Comparison**

The effect of mixing on streptavidin-biotin conjugation reaction was studied using both a table top mixer (Thermomixer®R, Eppendorf, NY) and a Design1 micromixer. For table top mixer, a 30  $\mu$ L BCF microbead sample was added to a 30  $\mu$ l SCP microbead sample in a centrifuge tube. The centrifuge tube was then mounted on the table top mixer and the sample was mixed for 15 min at 600 rpm. For micromixers, a syringe pump (PHD 2000 Programmable, Harvard Apparatus, MA) was used to continuously inject the BCF microbeads and SCP microbead samples into their respective inlets in the micromixer. The flow rate was 1  $\mu$ L/min and the solenoid valve was actuated at a frequency of 10 Hz. A 20  $\mu$ L mixed sample from the micromixer outlet was collected in a centrifuge tube for fluorescence measurement.

### **4.3.4 Performance Testing**

For the frequency test, the flow rate of the samples was held constant at 2  $\mu$ L/min, while the fluorescence measurements were made for various solenoid actuation frequencies in the range of 5 to 15 Hz. For the flow rate test, the solenoid actuation frequency was held constant at 10 Hz, while the sample flow rates were varied in the range of 1.2 - 4.0  $\mu$ L/min. The BCF microbeads and SCP microbead samples were injected simultaneously into the micromixer using a syringe pump and the mixed sample was collected at the outlet for fluorescence measurements.



### 4.3.5 Fluorescence Measurements

A VersaFluor benchtop Fluorometer (BIO-RAD Hercules, CA) was used for all fluorescence measurements. Figure 4.12 shows the VersaFluor fluorometer and the interior section with microcuvette and excitation and emission filters. The excitation and emission filters used in the fluorometer were EX 490/10 nm and EM 520/10 nm respectively. The fluorometer was turned ON for 30 min before any measurements were made.

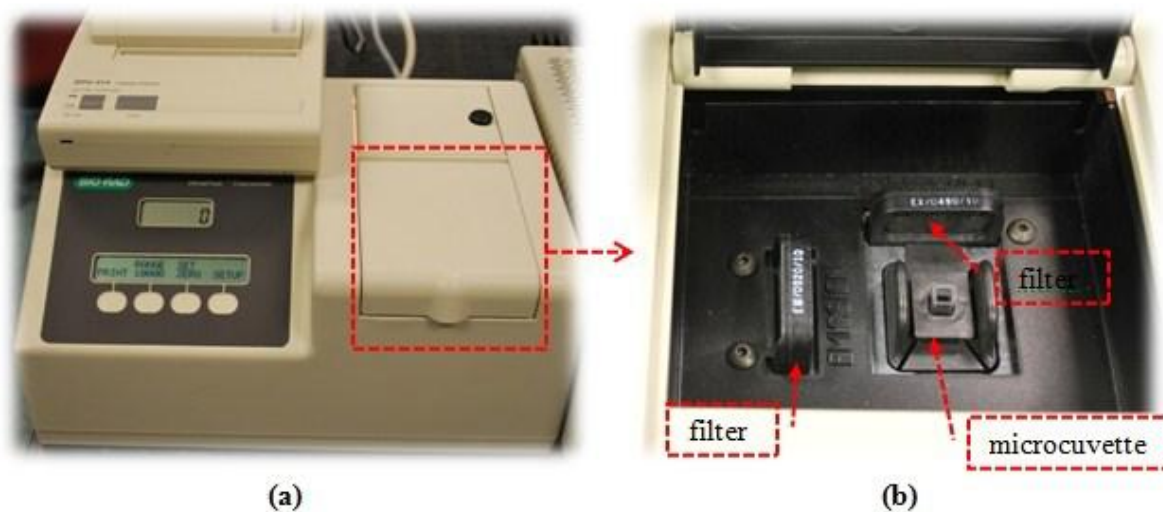


Figure 4.12 (a) VersaFluor Fluorometer (b) a microcuvette with test sample inserted in the cuvette holder and also shown are the excitation and emission filters

A 20  $\mu\text{L}$  BCF microbead sample was diluted with 200  $\mu\text{L}$  PBS buffer in a microcuvette and labeled as the pre-coupling BCF microbead sample. The microcuvette was placed in the fluorometer and fluorescence signal was recorded. The BCF-SCP conjugated microbeads solution was transferred to a microcuvette and labeled as the post-coupling sample. The microcuvette was inserted into the microcuvette holder of the fluorometer to measure the fluorescence signal intensity of the sample in RFU. Because of the magnetic separation, only

those BCF beads which bonded with the SCP beads remain to give off a fluorescence signal. The concentration of the fluorescent beads is directly proportional to the intensity of the fluorescence signal. The pre-coupling RFU values were compared with the post-coupling RFU values to estimate the coupling efficiency. Therefore, the fluorometer reading in RFU is a good indicator of the binding efficiency of the biotin-streptavidin beads conjugation reaction.

#### **4.4 Integrated System of Micromixer and Micropump**

The integrated micropump-micromixer system was first treated with Pluronic solution for 2 hours. The performance of the micropump was characterized by a method as described in the previous section. Figure 4.13 shows a schematic of the experimental setup layout for testing the integrated micropump-micromixer system for streptavidin-biotin conjugation reactions. Figure 4.14 shows the experimental setup on an optical table for testing integrated micropump-micromixer. integrated micropump-micromixer clamped on a test fixture. The two solenoid valves were separately controlled using individual function generators. Figure 4.15 (a) shows the test fixture with various components. Figure 4.15 (b) shows an integrated micropump-micromixer system clamped on the test fixture. The test samples for BCF and SCP microbeads were prepared as described in the previous section. The BCF and SCP microbead samples were introduced into their respective inlets with the micropump and micromixer in operation. A 20  $\mu\text{L}$  sample collected from the outlet was transferred via a pipette to a 100  $\mu\text{L}$  PBS buffer in a centrifuge tube. The centrifuge tube was then placed in a magnetic separation stand for 2 min. After 2 min, the supernatant was aspirated and discarded while the centrifuge tube was still in the magnetic separation stand. The centrifuge tube was removed from the magnetic separation stand and 100  $\mu\text{L}$  of PBS was added along the insides of the centrifuge tube where the separate microbeads are collected. This washing step was repeated three times. After the washing step,

BCF-SCP microbead conjugates were resuspended in 200  $\mu\text{L}$  of PBS for fluorescence measurements. The micromixer mixing performance based on streptavidin-biotin conjugation reaction was tested with respect to solenoid actuation frequency, compressed air pressure and flow rate of the samples.

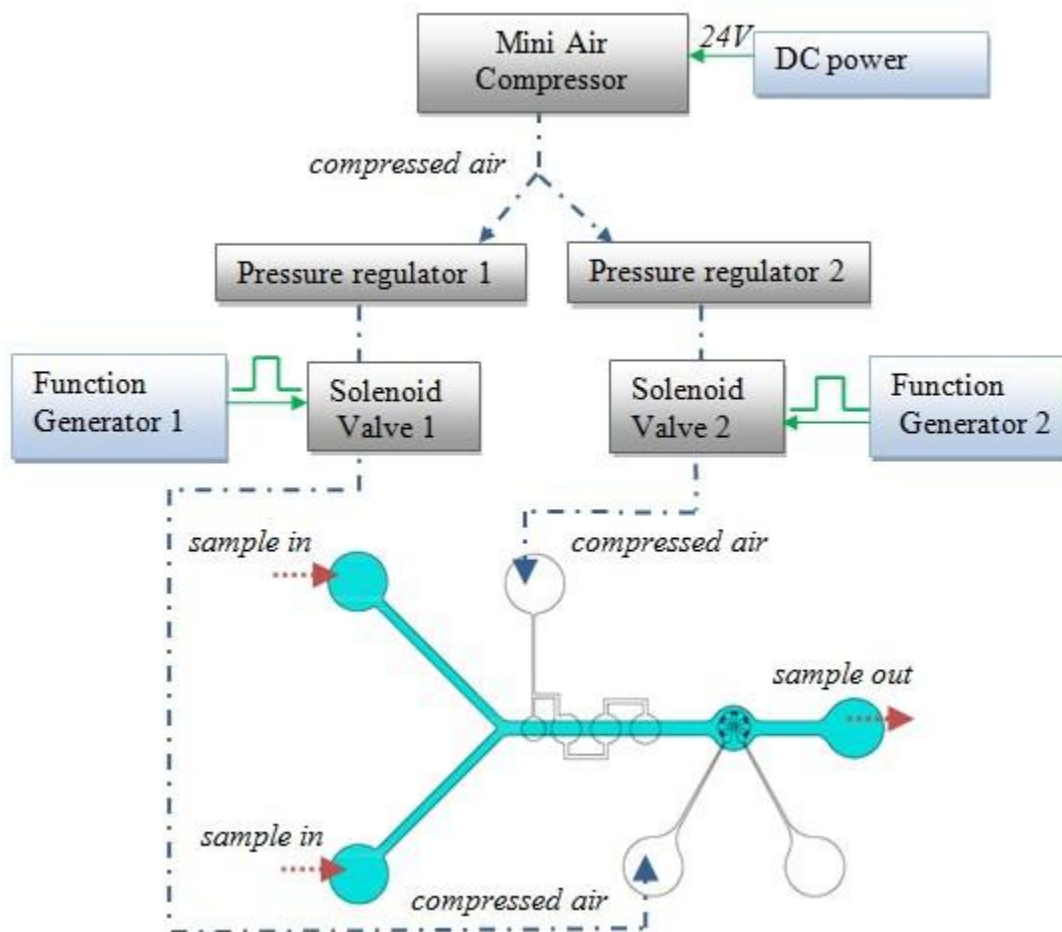


Figure 4.13 Schematic of an experimental setup for integrated micropump-micromixer testing

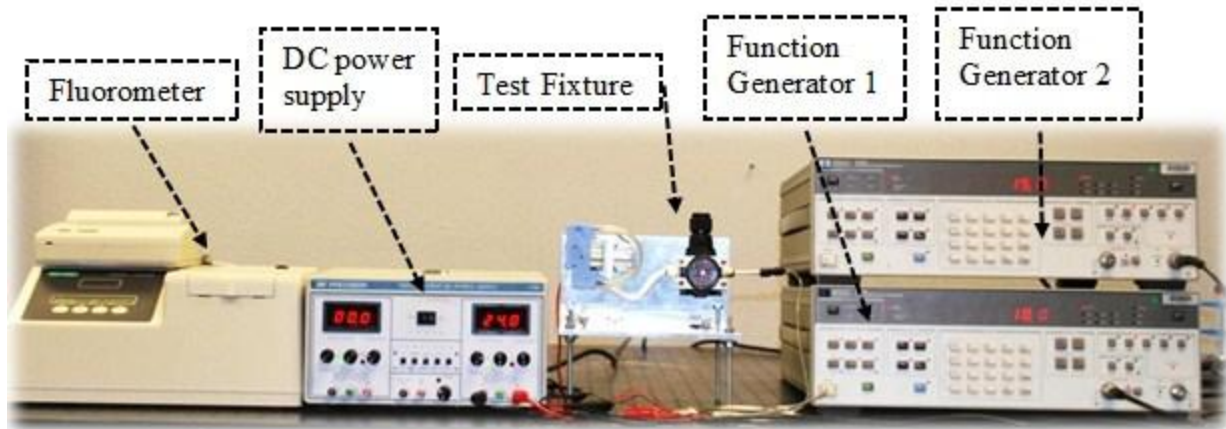


Figure 4.14 Experimental setup on an optical table for micropump-micromixer testing

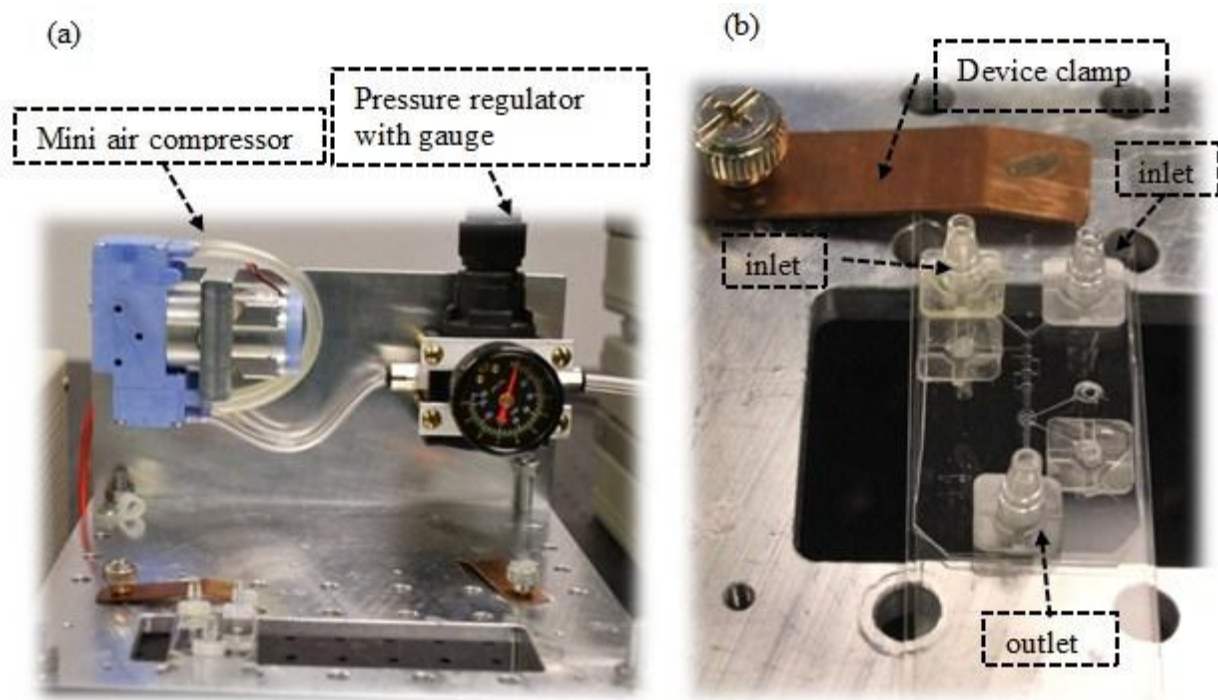


Figure 4.15 (a) A test fixture for integrated micropump-micromixer testing (b) An integrated micropump-micromixer clamped on the test fixture

## 4.5 Impedance Spectrum Measurement

Impedance spectrum measurements were performed using a HP 4192A LF impedance analyzer. For all impedance measurements, a sine modulated AC potential of 100 mV was applied across the interdigitated electrodes and the magnitude and phase angle of impedance were recorded for a frequency sweep from 10 Hz to 10 MHz. The impedance analyzer was controlled using a LabVIEW program (LabVIEW 8.0) installed on a laptop and interfaced with the impedance analyzer via a GPIB connection. A LabVIEW plug and play instrument driver for HP4192A was downloaded from National Instruments website and modified to perform a log sweep. The downloaded driver was originally designed for performing a linear scan. In order to perform a log scan, the block diagrams of “HP4192A Example.vi” and “Measure.vi” components of the downloaded driver was modified. The screenshots of the block diagram of the modified VI’s are shown in Figure 4.16 and Figure 4.17 respectively. The data acquired from the impedance analyzer was stored in an excel file format for further processing.

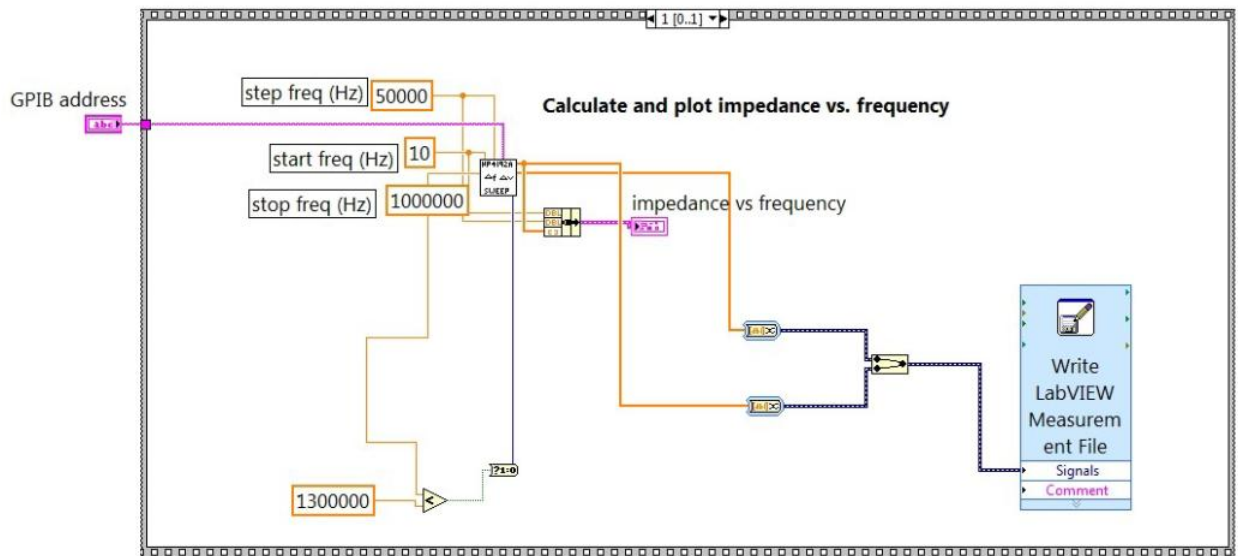


Figure 4.16 Modified block diagram of Example.vi

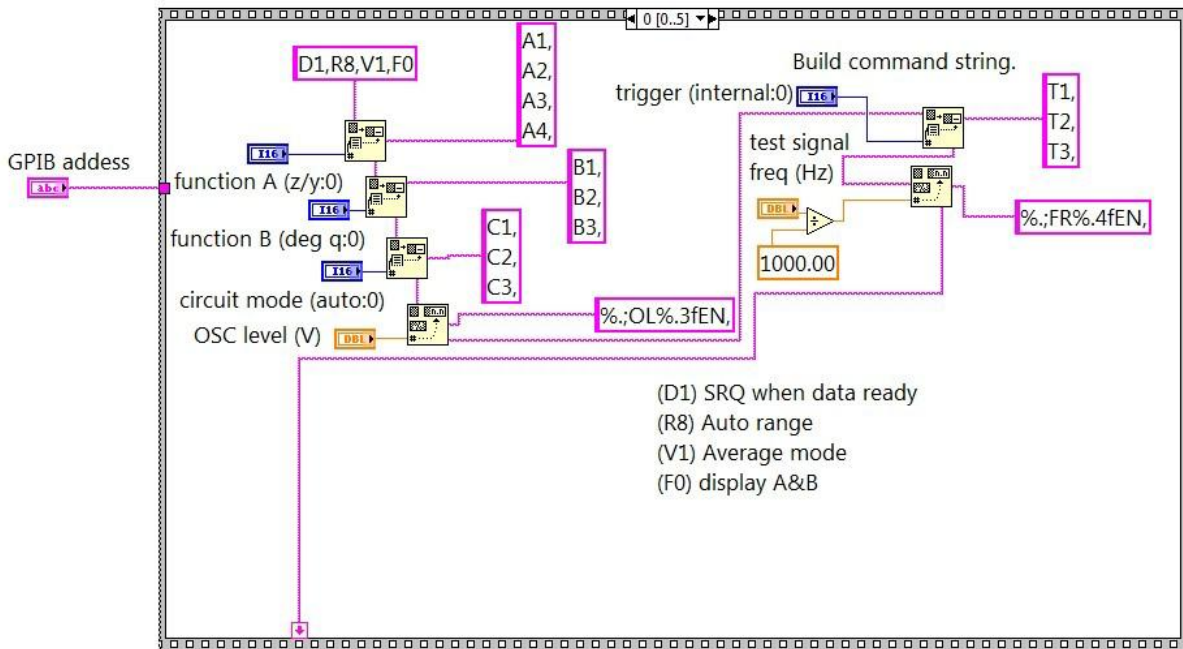


Figure 4.17 Modified block diagram of Measure.vi

## 4.6 Magnetic Microbead Separation

### 4.6.1 Magnet Selection

Two approaches for magnetic separation of paramagnetic beads were studied. The first approach was to use an electromagnet. Electromagnets of three different sizes and magnetic strength were purchased from Rochester Magnet Co. (East Rochester, NY). The second approach was to use permanent magnets. Neodymium disc permanent magnets of three different sizes and magnetic strength were purchased from Rochester Magnet Co. Table 4.1 and Table 4.2 show the list of permanent magnets and electromagnets respectively with their dimensions and magnetic field strength ratings. Figure 4.18 shows the various electromagnets and permanent magnets listed in Table 4.1 and Table 4.2





Figure 4.18 (a) to (c) Permanent magnets (d) to (f) Electromagnets for magnetic separation of SCP beads

Magnet	Diameter × Thickness (in)	Magnetic Field Strength (mT)
PM1	0.190 x 0.125	480
PM2	0.220 x 0.100	400
PM3	0.500 X 0.060	140

Table 4.1 Specification of permanent magnets

Magnet	Diameter × Height (in)	Magnetic Field Strength (mT)
EM1	1.25 x 1.25	70
EM2	1 x 1.25	120
EM3	0.500 x 1.5	80

Table 4.2 Specification of electromagnets

#### 4.6.2 Magnetic Separation Testing

Figure 4.19 shows a schematic of the experimental setup used to test the magnetic separation of SCP microbeads. The microfluidic system was mounted on the test fixture and the magnet to be tested was positioned below in contact with the microfluidic system. A syringe pump was used to inject SCP beads sample at a steady flow rate and was collected at the outlet for inspection. Figure 4.20 shows the experimental setup on an optical table for testing the magnetic separation of SCP microbeads using an electromagnet. The flow rate of the SCP bead sample was varied in the range of 1 - 20  $\mu\text{L}/\text{min}$ . A CCD camera mounted on the microscope was used to capture the video of SCP microbeads captured within the microfluidic system. Figure 4.21 (a) shows the test fixture with an electromagnet placed on a lab jack and in contact with the microfluidic system and Figure 4.21 (b) shows the the top view of the electromagnet in contact with the device. In case of electromagnets, a 12 V DC voltage was applied to activate the microfluidic system. The applied DC voltage was varied in the range 3 – 12 V to obtain different magnetic field strength from the electromagnet. Figure 4.22 (a) and (b) shows the experimental set up used for testing the permanent magnets and the top view of the microfluidic system with permanent magnet positioned on top.



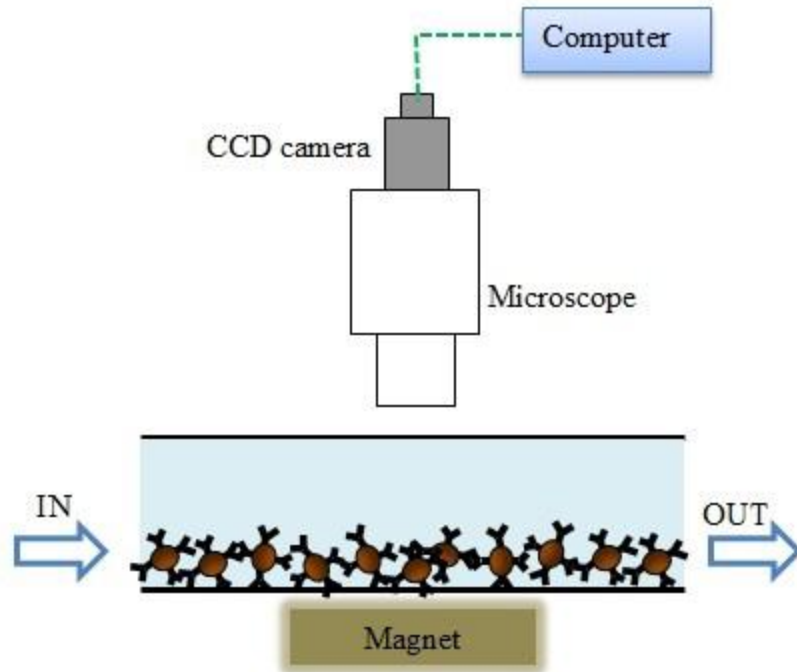


Figure 4.19 Schematic of a setup for testing magnets for magnetic separation of SCP beads

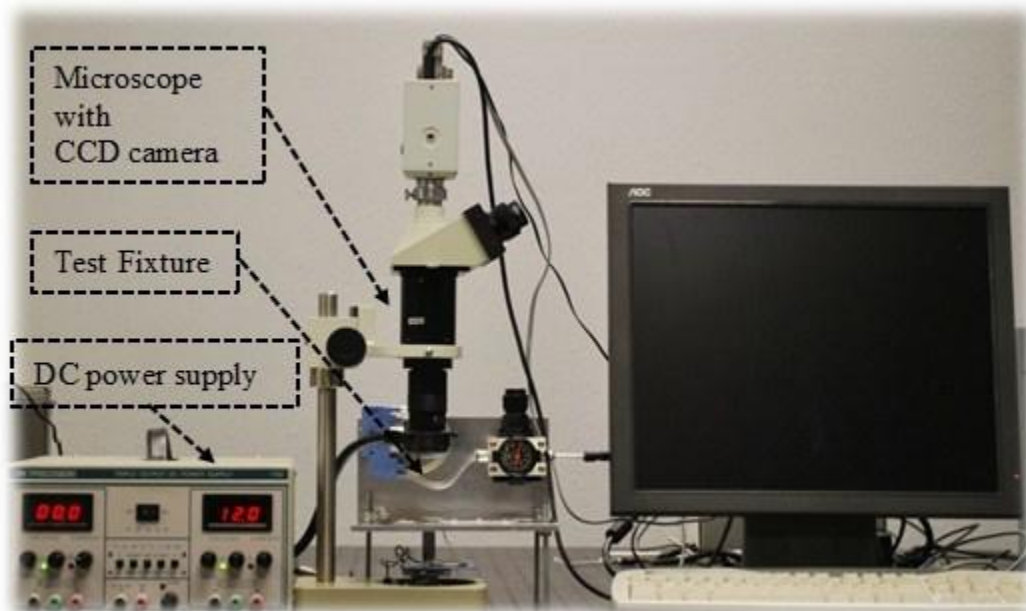


Figure 4.20 Experimental test setup on an optical table for magnetic separation of SCP microbeads using an electromagnet

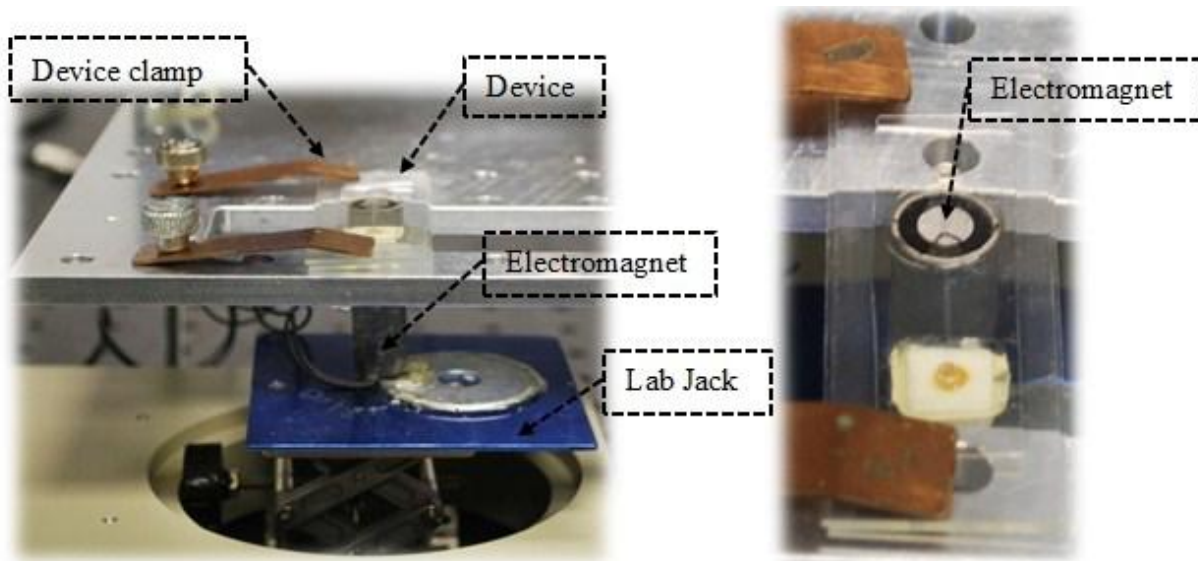
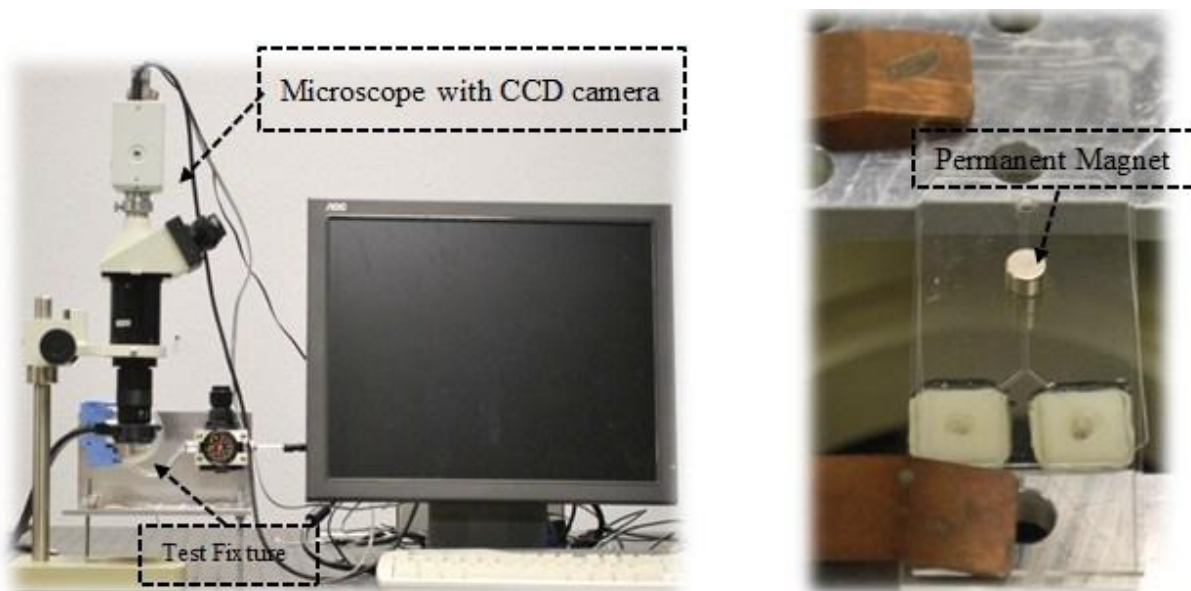


Figure 4.21 (a) Close view of the test fixture showing the electromagnet placed on a lab jack and in contact with the microfluidic device (b) Top view showing the electromagnet in contact with the device



(a)

(b)

Figure 4.22 (a) Test setup for magnetic separation of SCP beads with a permanent magnet (b) Top view of the device with a permanent magnet positioned on top

## 4.7 Fully Integrated System Testing

The fully integrated system was first tested for impedance detection for various BCF microbead concentrations. The fully integrated system was then tested for detecting insulin based on a bead based immunoassay to separate insulin from a test sample followed by impedance detection. Figure 4.23 shows the schematic of an experimental setup for testing a fully integrated system.

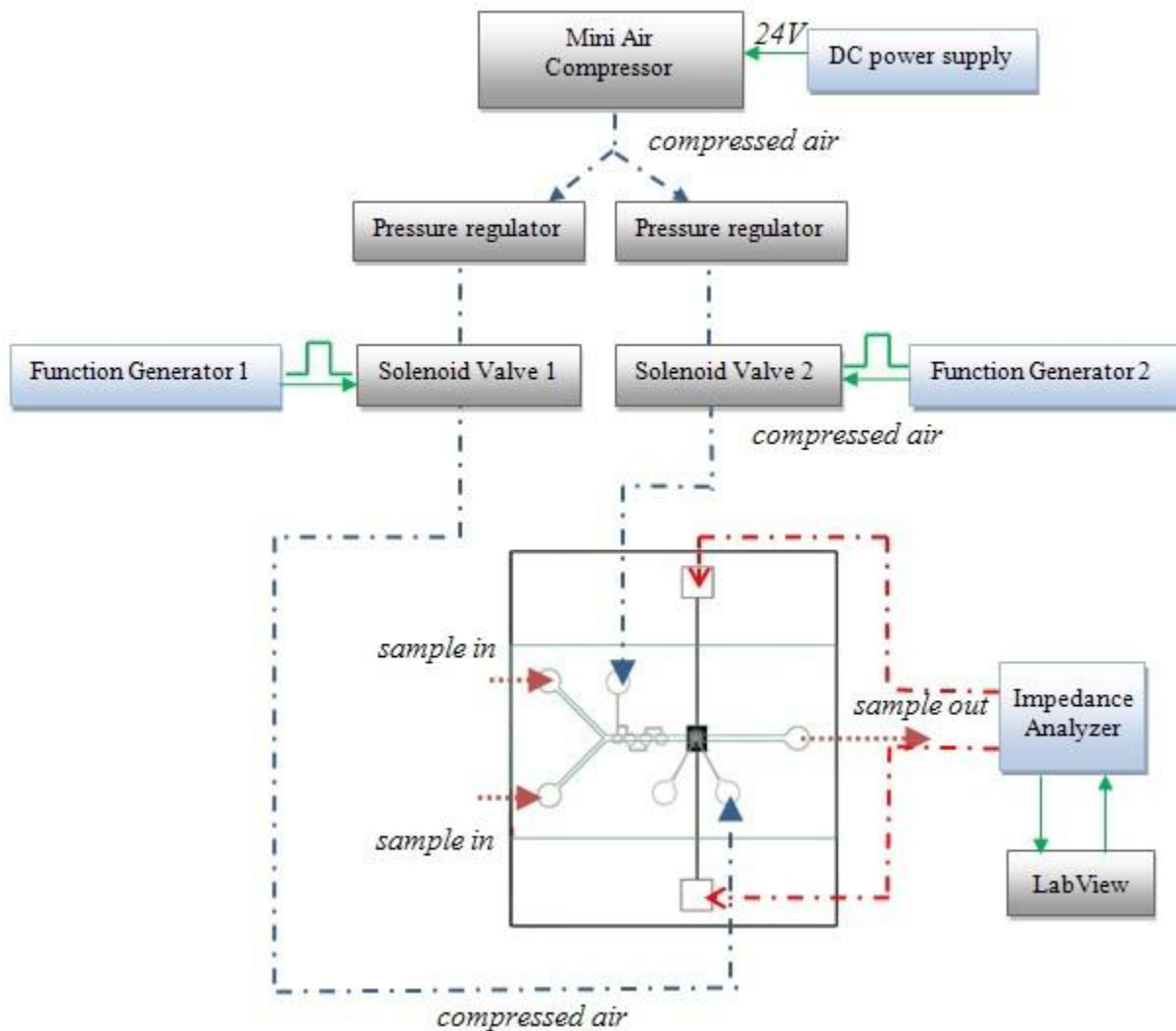


Figure 4.23 Schematic of an experimental setup layout for testing a fully integrated device

Figure 4.24 shows an experimental setup on an optical table for fully integrated system testing. Figure 4.25 shows the test fixture with various components and Figure 4.26 shows the fully integrated system clamped on a test fixture.

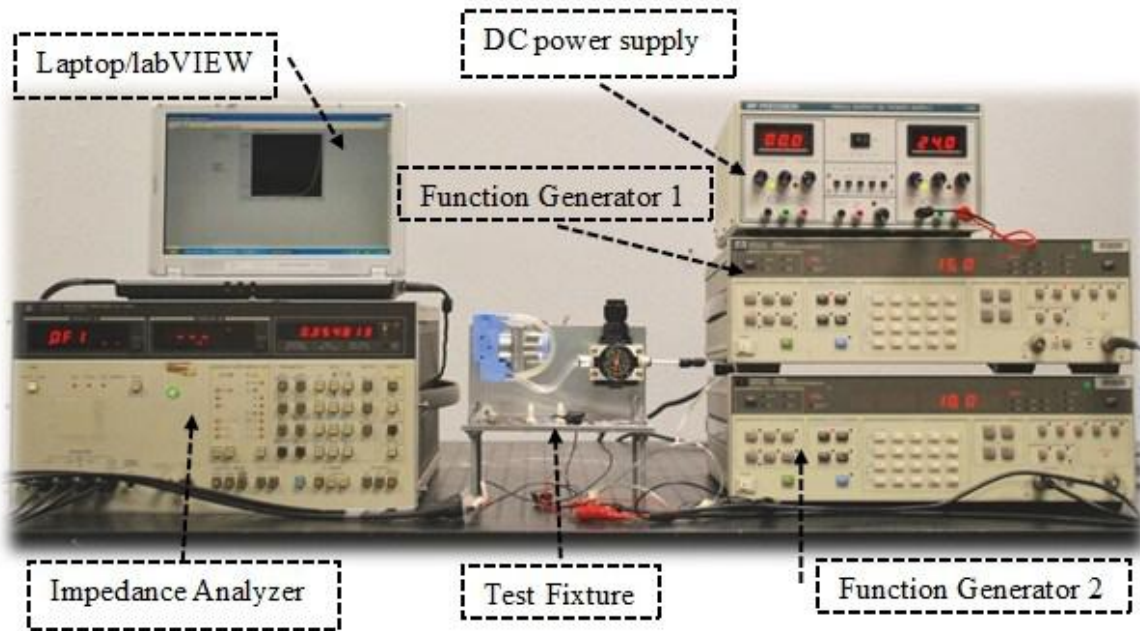


Figure 4.24 Experimental test setup for fully integrated microfluidic system

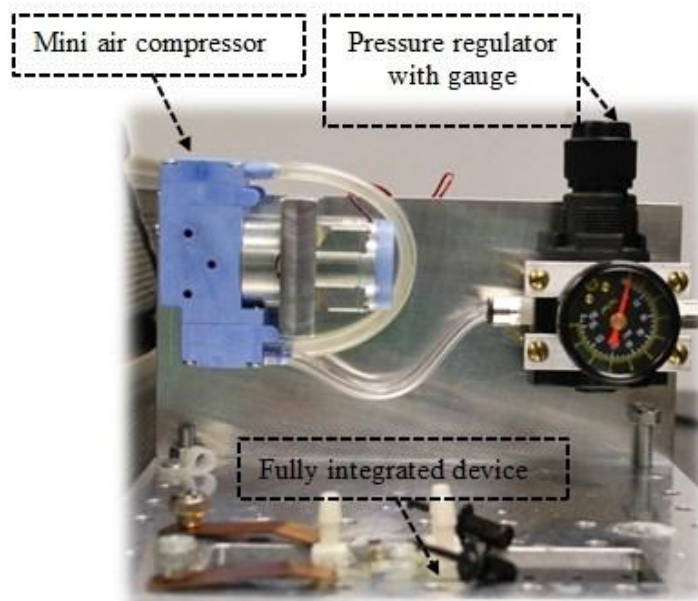


Figure 4.25 Test fixture with various components for fully integrated system testing

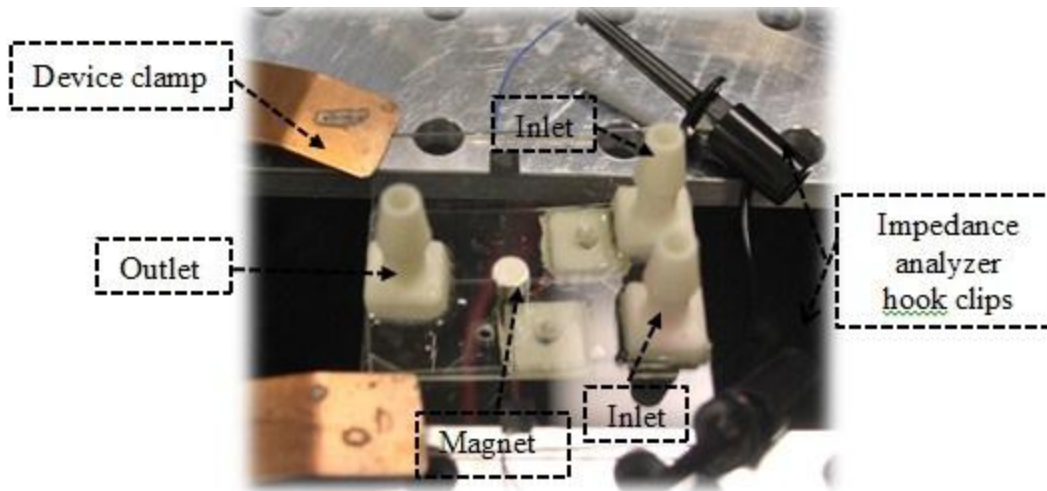


Figure 4.26 Fully integrated microfluidic system clamped on the test fixture

#### 4.8 BCF Microbeads Detection

The fully integrated microfluidic system was treated with Pluronic solution to make the PDMS surface hydrophilic and also reduced any non-specific protein binding. Figure 4.27 shows the process flow for testing streptavidin-biotin conjugation followed by impedance measurement of BCF microbeads. The micropump was operated at a flow rate of 2  $\mu\text{L}/\text{min}$  and the micromixer was operated at 10 Hz, 20 psi conditions. A 20  $\mu\text{L}$  sample of BCF microbead solution and 20  $\mu\text{L}$  of SCP microbead solution were introduced in their respective inlets and pumped to the mixing chamber. A permanent magnet placed below the IDE was used to attract the SCP microbeads and hold them close to the surface of the electrodes. A 20  $\mu\text{L}$  solution of MES buffer was introduced at the inlet and a flow rate of 10  $\mu\text{L}/\text{min}$  was used to wash away any unbound BCF microbeads within the mixing chamber. The wash step was repeated twice. After the wash step, impedance measurement was performed by following a procedure as described in the impedance measurement section.



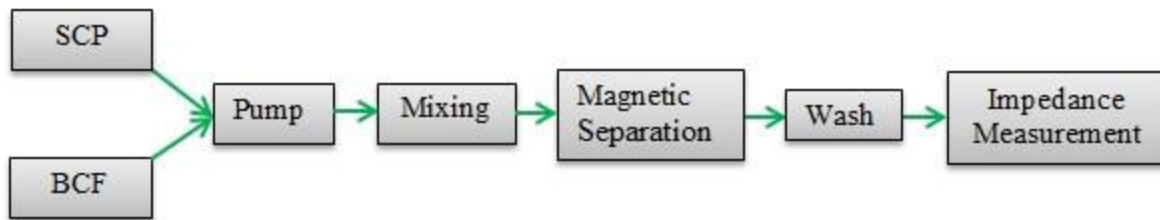


Figure 4.27 Process flow for BCF microbead detection using the fully integrated microfluidic system

## 4.9 Insulin Detection

### 4.9.1 Preparation of Magnetic Beads-Antibody Conjugate (MBAC)

A protein coupling kit (BioMag® Plus Carboxyl Protein coupling starter kit, Catalog# 86010-1) was purchased from Polysciences, Inc. (Warrington, PA). The kit includes magnetic microbeads (BioMag® Plus Carboxyl terminated particles, 2.5 mL, 20 mg/mL, Catalog# 860111-10) functionalized with carboxyl group, 0.1 g of EDC (1-ethyl-3-(3-dimethylaminopropyl) carbodiimide), 15 mL conical centrifuge tubes, a magnetic separator (MultiStep® Biomag separator), 25 mL quenching solution, 175 mL MES buffer (pH 5.2, 0.05 M) and 125 mL wash buffer. Unconjugated Mouse Anti-Insulin (1G11) monoclonal antibody (MAI-Ab) (Catalog# bsm-0855mm, 100 µg lyophilized) was obtained from Bioss, Inc. (Woburn, MA). The carboxyl groups on the surface of the microbeads are first activated by carbodiimide which allows the amine groups on antibodies to be covalently attached.

### 4.9.2 Activation of Carboxyl Groups

A 0.5 ml (10.0 mg) sample of magnetic microbeads was transferred to a 15 mL conical centrifuge tube. The centrifuge tube was inserted into the magnetic separator stand for 3 min to allow magnetic separation. The supernatant was then aspirated and discarded. The centrifuge

tube was removed from the magnetic separator and a 5 mL MES buffer solution was added. The centrifuge tube was then vigorously shaken to mix. The centrifuge tube was inserted into the magnetic separator for 3 min to allow magnetic separation. The supernatant was then aspirated and discarded. The washing step with MES buffer was repeated three times. After the final wash the magnetic beads were resuspended in 5 ml of MES buffer. The EDC was removed from the freezer and allowed to thaw for a minimum of 30 min. The required mass of EDC (1.6 mg EDC/mg of magnetic beads) was measured, added to the magnetic beads in solution and mixed vigorously on a table top shaker for 30 s. The centrifuge tube was then placed in a shaker (Orbit Environ-Shaker model 3527, Lab-Line) at 250 rpm for 30 min at room temperature. It is important to not allow the beads to settle during mixing. After mixing the activated magnetic beads were magnetically separated on the magnetic separator and the supernatant was aspirated and discarded. After the magnetic separation 5 mL of MES buffer was added to the activated magnetic beads and shaken on a table top shaker (Touch Mixer model 232, Fisher Scientific, Pittsburgh, PA) for 30 s. The activated magnetic beads were magnetically separated on the magnetic separator, supernatant was aspirated and discarded. This wash step with MES buffer was repeated three times.

### **4.9.3 Antibody Coupling**

A 100  $\mu\text{g}$  sample of MAI-Ab in the lyophilized form was reconstituted with 100  $\mu\text{L}$  sterile DI water to obtain a stock concentration of 1  $\mu\text{g}/\mu\text{L}$ . A 100  $\mu\text{L}$  sample of MAI-Ab solution was diluted with 0.5 mL MES buffer. A 50  $\mu\text{L}$  sample of diluted MAI-Ab solution was removed and added to 950  $\mu\text{L}$  of MES buffer to obtain a 1:20 dilution “pre-coupling sample” for coupling efficiency determination. The remaining MAI-Ab was added to the activated magnetic beads and mixed in a shaker (Orbit environ-shaker model 3527, Lab-line) at 250 rpm for 24 hrs at room

temperature to obtain MBAC. After coupling, the MBAC were magnetically separated on a magnetic separator. The supernatant was aspirated and saved as the “post-coupling sample” for coupling efficiency determination. The MBAC were resuspended in 0.5 mL MES buffer and mixed using a table top shaker (Touch Mixer odel 232, Fisher Scientific, Pittsburgh, PA). After mixing the MBAC were magnetically separated and the supernatant was aspirated and discarded. A 0.5 mL quenching solution was added to the MBAC and mixed in a shaker at room temperature for 30 min. After mixing, the MBAC was magnetically separated and the supernatant was aspirated and discarded. A 0.5 mL wash buffer was added to the MBAC and mixed on a table top shaker. After mixing, the MBAC was magnetically separated and the supernatant was aspirated and discarded. This wash step was repeated three times. After the last wash, the MBAC were resuspended to 0.2 mL in wash buffer. The MBAC were stored at 4°C as a suspension in wash buffer.

#### **4.9.4 Coupling Efficiency Determination**

In order to determine the coupling efficiency of MAI-Ab and magnetic microbeads, a Quant-iT™ Protein Assay kit (Life Technologies, Carlsbad, CA) was used. The kit included a protein reagent (component A), eight BSA standards of known concentrations (component B) and a protein buffer solution (component C). A protein working solution was prepared by diluting 30 µL of protein reagent in 5970 µL protein buffer solution to obtain a 1:200 dilution. A 10 µL sample of each BSA standard was added to 190 µL of protein buffer solution in a separated centrifuge tube to obtain BSA standard test solution and labeled with respective standard number. This sample preparation step was performed three times to obtain triplicates of each BSA standard test solution and protein working solution. All of the centrifuge tubes with BSA standard test solution were shaken on a table top shaker for 3 seconds and then incubated at room



temperature for 15 min. After 15 min of incubation, 200  $\mu\text{L}$  of the BSA standard test solution were transferred to a microcuvette to perform fluorescence measurements using the Fluorometer. This step was performed to obtain three fluorescence readings for each of the eight BSA standard test solution. The fluorescence reading of the BSA standard solutions was plotted against their respective known concentrations to obtain a standard calibration curve. A 20  $\mu\text{L}$  solution of the “pre-coupling sample” was mixed with 180  $\mu\text{L}$  of protein working solution in a centrifuge tube to obtain a pre-coupling test solution. This step was repeated three times to obtain a triplicate of the pre-coupling test sample. A 20  $\mu\text{L}$  solution of the “post-coupling sample” was mixed with 180  $\mu\text{L}$  of protein working solution in a centrifuge tube to obtain a post-coupling test sample. This step was repeated three times to obtain a triplicate of the post-coupling test sample. All of the centrifuge tubes were shaken on a table top shaker for 3 seconds and then the samples were incubated at room temperature for 15 min. After 15 min of incubation, 200  $\mu\text{L}$  of each sample was transferred to a microcuvette to perform fluorescence measurements using the Fluorometer. The coupling efficiency was calculated based on the RFU values of the “pre-coupling sample” and “post-coupling sample”.

#### **4.9.5 Insulin Detection**

A 1 M, 100 mL solution of 2-Morpholinoethanesulphonic acid (MES) was purchased from Sigma-Aldrich (St. Louis, MO) and was diluted with DI water to obtain a 100 mM MES solution. Insulin, Recombinant Human (Catalog# 91077C-100MG) was purchased from Sigma-Aldrich (St. Louis, MO). A 1 L standard solution of 0.1M Hydrochloric Acid (HCl) (Catalog# 38280-1EA) was purchased from Sigma-Aldrich (St. Louis, MO) and diluted with DI water to obtain a 0.01 M HCl solution. A 10 mg sample of insulin was mixed in a 20 ml solution of 0.01 M HCl in a centrifuge tube to obtain an insulin stock solution. The stock solution was serially

diluted with MES buffer solution to obtain insulin samples of concentrations ranging from  $10^{-11}$  to  $10^{-5}$  M. The concentration of insulin antibody was calculated based on the coupling efficiency of MAI-Ab and magnetic microbeads. For MAI-Ab, with molecular weight 160 kDa, and a mass of 100  $\mu\text{g}$ , with 85% coupling efficiency:

$$\text{Concentration of insulin antibody} = \frac{(100 \times 10^{-6}) \text{g} \times (0.85)}{160 \times 10^3 \frac{\text{g}}{\text{mol}}} = 5.31 \times 10^{-10} \text{ mol} \quad (4.1)$$

For a 20  $\mu\text{L}$  insulin sample with a concentration of  $10^{-5}$  mol:

$$\text{Concentration of insulin} = (20 \times 10^{-6}) \text{L} \times 10^{-5} \frac{\text{mol}}{\text{L}} = 2 \times 10^{-10} \text{ mol} \quad (4.2)$$

The concentration of insulin antibodies used was 2.65 times more than the highest insulin concentration that was tested. Figure 4.28 shows the process flow for insulin detection.

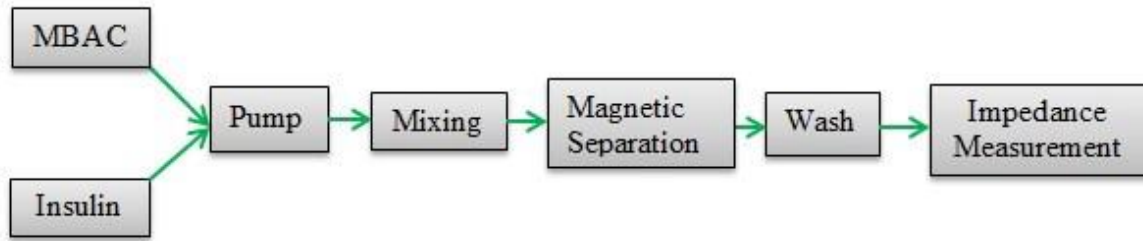


Figure 4.28 Process flow for insulin detection using the fully integrated microfluidic system

The fully integrated device was first treated with Pluronic solution for 2 hours to make the PDMS surface hydrophilic and also reduced any non-specific protein binding. The micropump was operated at a flow rate of 2  $\mu\text{L}/\text{min}$  and the micromixer was operated at 10 Hz, 20 psi conditions. A 20  $\mu\text{L}$  sample of MBAC and 20  $\mu\text{L}$  of insulin sample were introduced simultaneously in their respective inlets and pumped to the mixing chamber. A permanent

magnet placed below the IDE was used to attract the MBAC and hold them close to the surface of the electrodes. A 20  $\mu\text{L}$  solution of MES introduced at the inlet and a flow rate of 10  $\mu\text{L}/\text{min}$  was used to wash away any unbound insulin within the mixing chamber. The wash step was repeated twice. After the wash step, impedance measurement was made by following a procedure as described in the impedance measurement section.

## 5. RESULTS AND DISCUSSIONS

This chapter presents and analyzes the experimental results and numerical simulation. The first section presents the results of the performance testing for the three pump designs. Specifically, the variation of flow rate with respect to actuation frequency and compressed air pressure is analyzed. The experimental results are compared with the results of a 2D COMSOL simulation of the micropump. The second section discusses the qualitative and quantitative performance of the micromixer. The qualitative testing was based on mixing of two colored dyes with respect to time. The quantitative testing was based on mixing efficiency determination for biotin-streptavidin bead conjugation reaction with respect to actuation frequency, flow rate and compressed air pressure. The third section discusses the magnetic microbead separation scheme using permanent magnets and electromagnets of various sizes and magnetic strengths. The fourth section discusses the testing of the integrated microfluidic system for detection of biotin coated beads and insulin.

### 5.1 Performance of Micropumps

The performance characteristics of the three micropump designs were experimentally determined. The two main control parameters that affect the performance of the micropump are the compressed air pressure and the actuation frequency of the solenoid valve.

#### 5.1.1 Repeatability of Flow Rate

For each design, the variation of flow rate within an individual micropump when tested three times and variation of flow rates between three separate micropumps was determined. Figure 5.1 shows the variation in average flow rate within a single Design1 micropump when tested three times. Figure 5.2 shows the variation in average flow rate between three micropumps of

Design1, each tested three times. The mean variation in flow rate for a micropump of Design 1 was 4.6%, with a maximum variation of 6.5% and a minimum variation of 1.54%. The mean variation in flow rates between three micropumps of Design1 was determined to be 8.25%, with a maximum variation of 19.7% and a minimum variation of 1.3%.

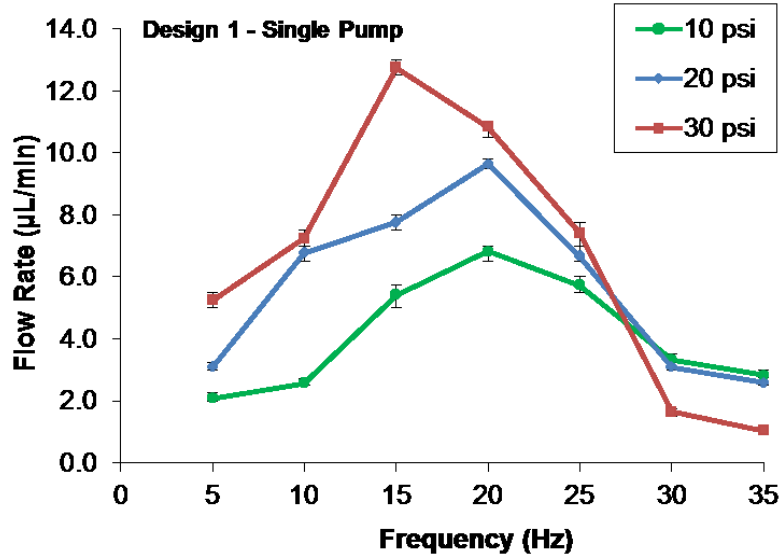


Figure 5.1 Flow rate variations within a single Design1 micropump

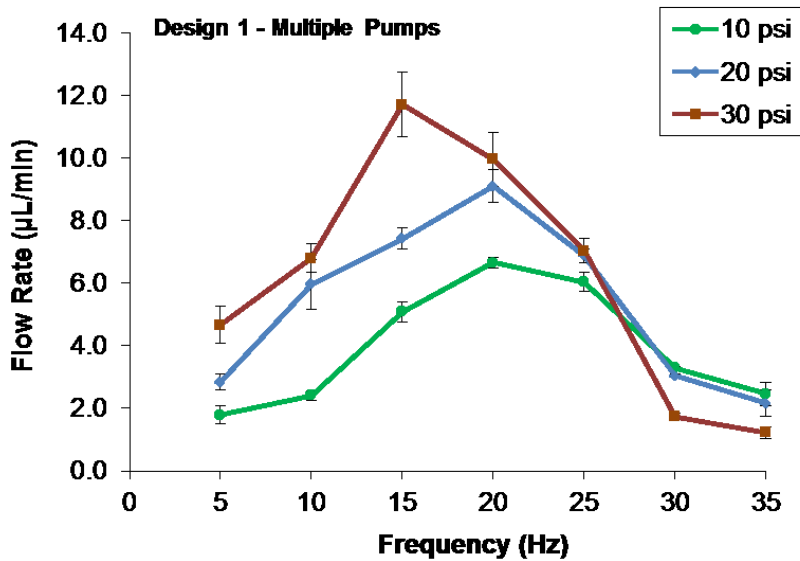


Figure 5.2 Flow rate variations between three different micropumps of Design1

Figure 5.3 shows the variation in average flow rate within a single Design2 micropump when tested three times. Figure 5.4 shows the variation in average flow rate between three micropumps of Design2, each tested three times.

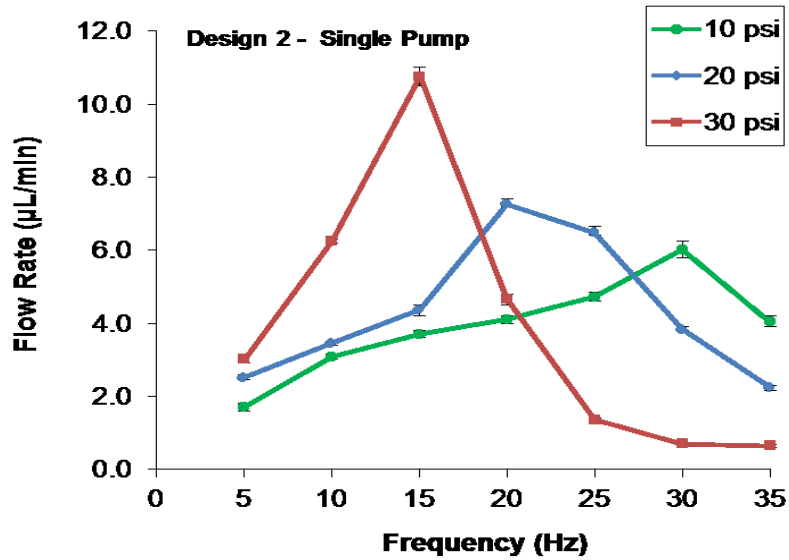


Figure 5.3 Flow rate variations within a single Design2 micropump

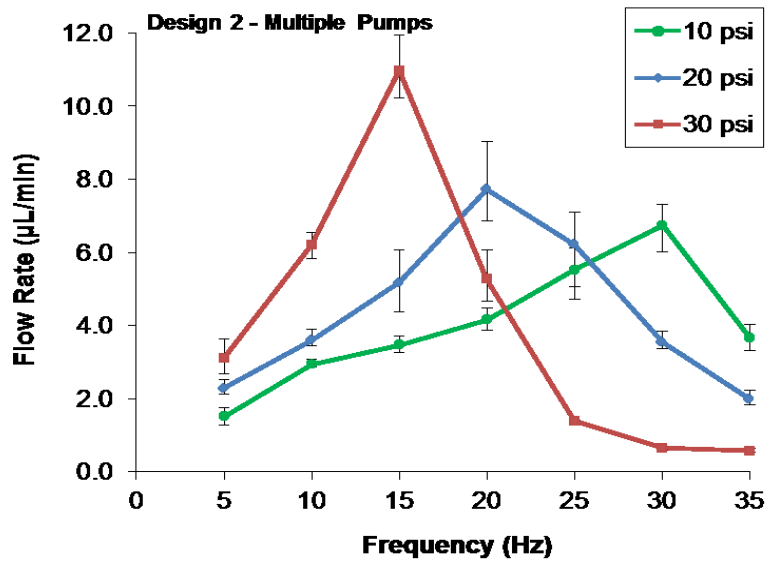


Figure 5.4 Flow rate variations between three different micropumps of Design2

The mean variation in flow rate for a micropump of Design2 was 2.9%, with a maximum variation of 6.0% and a minimum variation of 0.75%. The mean variation in flow rates between three micropumps of Design2 was determined to be 10.6%, with a maximum variation of 17.4% and a minimum variation of 1.75%. Figure 5.5 shows the variation in average flow rate within a single Design3 micropump when tested three times. Figure 5.6 shows the variation in average flow rate between three micropumps of Design3, each tested three times. The mean variation in flow rate for a micropump of Design3 was 1.9%, with a maximum variation of 5.4% and a minimum variation of 0.8%. The mean variation in flow rates between three micropumps of Design3 was determined to be 10.3%, with a maximum variation of 17.3% and a minimum variation of 1.57%.

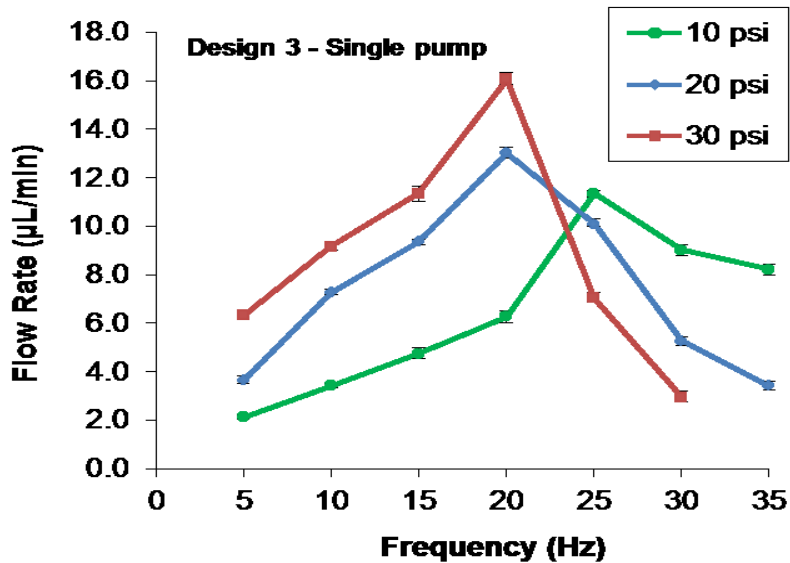


Figure 5.5 Flow rate variations within a single Design3 micropump

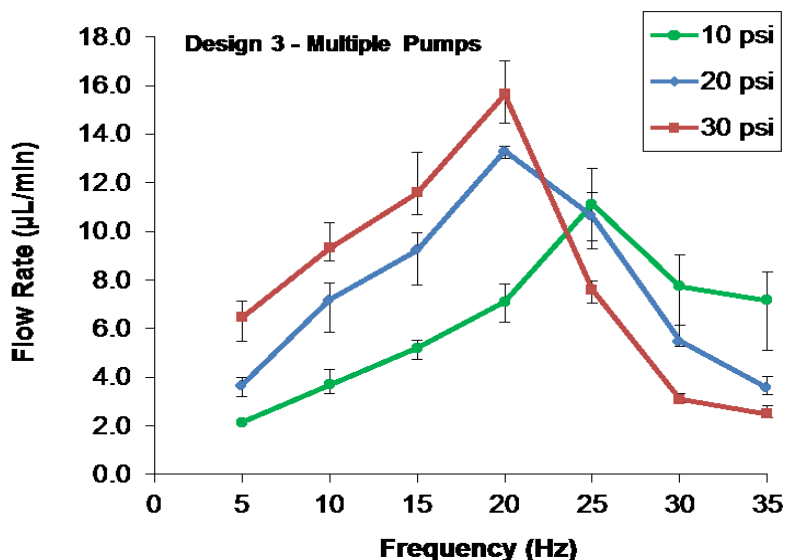


Figure 5.6 Flow rate variations between three different micropumps of Design3

The variation in flow rates from one pump to another of the same design can also be attributed to variations in the thickness of the PDMS membrane between micropumps. The variation in thickness of the PDMS membrane is due to the non-uniformity of the SU-8 film thickness obtained by the spin coating process step in fabrication of the SU-8 mold used for casting PDMS. A DekTak profilometer measurement indicated that the SU-8 film thickness varied between 90 – 100  $\mu\text{m}$  at different locations on the wafer.

After the completion of the micropump performance testing for all three designs, Design 3 was selected to be incorporated into the fully integrated microfluidic system. Among the three micropump designs, Design 3 was observed to have the highest flow rate (16  $\mu\text{L}/\text{min}$  at 20 Hz, 30 psi operating conditions) with the lowest mean variation in flow rate. The fabrication yield with Design 3 was also observed to be higher than other designs. The circular air chamber geometry used in Design3 provides an advantage over the rectangular air chamber geometry with sharp corners used in Design1 and Design2. The circular geometry of Design 3 air chambers



enables an easier release of the cured PDMS without any tear while being removed from the SU-8 mold during the fabrication process. In case of Design1 and Design2, the cured PDMS tends to tear at the corners causing a reduction in the yield per wafer.

### **5.1.2 Peak Flow Rate**

The micropump performance test results indicate that at a constant pressure, the flow rate increases with an increase in actuation frequency until a peak flow rate is reached and is followed by a drop in flow rate at higher frequencies. The frequency at which the peak flow rate is observed is referred to as the optimal frequency. The average peak flow rates observed with Design1, Design2 and Design3 micropumps are 12.75  $\mu\text{L}/\text{min}$  (at 30 psi, 15 Hz), 10.75  $\mu\text{L}/\text{min}$  (at 30 psi, 15 Hz) and 16.0  $\mu\text{L}/\text{min}$  (at 30 psi, 20 Hz) respectively. The maximum flow rate at a constant pressure depends on the fill and release time of the compressed air within the air chambers. The actuation frequency used to cycle the compressed air pressure controls the time available for the pressure inside the air chambers to change with time. If the frequency of operation is too high, there is not enough time for the air chambers to be completely filled and released and the flow rate decreases. If the operation frequency is too low, the number of pump cycles would also be low with idle time in between cycles, leading to lower flow rates even though the air chambers would have enough time to reach the actuation pressure. It was observed that the peak flow rate for the various designs increased with pressure. For Design3, the peak flow rate increased by 30% when the pressure was increased from 10 psi to 20 psi. The deflection of a PDMS membrane is directly proportional to the applied pressure. As the applied pressure is increased the deflection of the PDMS membrane increases and causes more fluid volume to be displaced, resulting in an increased flow rate.

These results of flow rate variation with respect to actuation frequency, with a peak flow rate at an optimal frequency, are similar to some of the previously reported peristaltic micropumps. A peristaltic micropump with piezoelectric actuation [168] has been reported to have a similar flow rate dependency on frequency. The flow rate was observed to increase with frequency until a peak flow rate of 25  $\mu\text{L}/\text{min}$  was attained at an optimal frequency of 200 Hz, followed by a drop in flow rates for all higher frequencies. Similarly, a single stroke peristaltic PDMS micropump has been reported [169] with the flow rate increasing with frequency until a peak flow rate of 4  $\mu\text{L}/\text{min}$  was observed at an optimal frequency of 15 Hz, followed by a drop in flow rate for all higher frequencies. The micropumps were tested over a period of three months without any failure. The durability of the micropump would mainly depend on the fracture of the PDMS membranes. However, PDMS is a highly resilient polymer material [170] and the performance of the micropump is satisfactory as long as the operating conditions are well regulated.

## 5.2 Micropump Simulation - Equivalent Circuit Analysis

In order to better explain the results of the micropump performance with the existence of a peak flow rate, an equivalent circuit simulation and COMSOL simulation was carried out. The purpose of the equivalent circuit analysis is to determine the time delay between the sequential actuation of the four PDMS membranes. The micropump system was converted into an equivalent electrical circuit and then analyzed using the SPICE analog circuit simulation software.

The equation governing a mechanical system [171] can be written as

$$F = m \frac{dv}{dt} + \alpha v + k \int v dt \quad (5.1)$$

where  $F$ ,  $v$ ,  $m$ ,  $\alpha$  and  $k$  are the force, velocity, mass, friction coefficient and stiffness respectively.

Equation 5.1 can be rewritten [171] as

$$P = \left(\frac{m}{S^2}\right) \frac{d\phi}{dt} + \left(\frac{\alpha}{S^2}\right) \phi + \left(\frac{k}{S^2}\right) \int \phi dt \quad (5.2)$$

where  $P$ ,  $\phi$  and  $S$  are the pressure, flow rate and area normal to flow direction respectively.

Equation 5.2 is similar to a series RLC circuit with an equation [171] as below

$$e = L \frac{di}{dt} + Ri + \frac{1}{C} \int idt \quad (5.3)$$

where  $e$ ,  $L$ ,  $i$ ,  $R$ ,  $C$  are voltage, inductance, current, resistance and capacitance respectively.

Comparing equations 5.2 and 5.3, an analogy between fluidic system and an electrical system can be obtained as shown in Table 5.1 [171]

Mechanical/Fluidic Parameters		Equivalent Electrical Parameters	
$\Phi$	flow rate	$i$	Current
$P$	pressure	$e$	Voltage
$m/S^2$	(where $m$ is mass)	$L$	Inductance
$\alpha/S^2$	(where $\alpha$ is friction coefficient)	$R$	Resistance
$k/S^2$	(where $k$ is the stiffness)	$C$	Capacitance

Table 5.1 Mechanical/Fluidic parameters and their electrical analogues.

Hydraulic resistance ( $R_{hyd}$ ) represents energy dissipation due to fluid's viscous friction against component's wall and is calculated by integrating the velocity profile over the cross-sectional area of the channel such that flow rate as a function of pressure drop is known [172]. Hydraulic resistance depends on the channel geometry. For a channel with rectangular cross-section,  $R_{hyd}$  is calculated as [172]

$$R_{hyd} = \frac{4\mu l}{ab^3} \left( \frac{16}{3} - 3.36 \frac{b}{a} \left( 1 - \frac{b^4}{12a^4} \right) \right)^{-1} \quad (5.4)$$

where  $l$  is channel length,  $a$  is half channel width,  $b$  is half channel height and  $\mu$  is fluid viscosity. The hydraulic capacitance ( $C_{hyd}$ ) represents the elastic behavior of the microfluidic component and relates the pressure difference to volume variation [173]. This variation is due to both the deformation of the structure and the elastic property of the fluid [173].  $C_{hyd}$  for a polymer membrane is given by

$$C_{hyd} = \frac{(1-\nu^2)a^4S}{65.8Et^3} \quad (5.5)$$

where  $a$  is the side length of the membrane,  $S$  is the shape factor,  $\nu$  is the Poisson's ratio,  $t$  is the membrane thickness, and  $E$  is the Young's modulus of the membrane. A compressed air source applying pressure on the PDMS membrane is equivalent to applying a voltage to a node on the equivalent circuit. The compressed air pressure can be represented by a voltage source in the equivalent circuit.

### 5.2.1 Transient Response of the Equivalent Circuit

The time-phased sequential deflection of the PDMS membranes with interconnecting microchannels when actuated by a single compressed air source can be modeled by a parallel RC circuit. The RC circuit can be modeled by replacing the chambers and the membranes with electrical capacitors ( $C_1$ ,  $C_2$ ,  $C_3$  and  $C_4$ ) and the interconnecting microchannels with the electrical resistors ( $R_1$ ,  $R_2$ ,  $R_3$  and  $R_4$ ). The compressed air source connected to the inlet of the air chambers through a solenoid valve controlled by square wave voltage signal can be replaced by a square pulse voltage source  $V_{in}$ . Table 5.2 shows the calculated values of resistances and the capacitances for all components of the equivalent circuit as shown in Figure 5.7.

Resistor	Value (Nsm <sup>-5</sup> )	Capacitor	Value (m <sup>5</sup> N <sup>-1</sup> )
R1	3.4 x 10 <sup>10</sup>	C1	1.4 x 10 <sup>-14</sup>
R2	1.5 x 10 <sup>10</sup>	C2	5.0 x 10 <sup>-14</sup>
R3	9.0 x 10 <sup>9</sup>	C3	5.0 x 10 <sup>-14</sup>
R4	9.0 x 10 <sup>9</sup>	C4	5.0 x 10 <sup>-14</sup>

Table 5.2 Equivalent circuit component values for Design 3

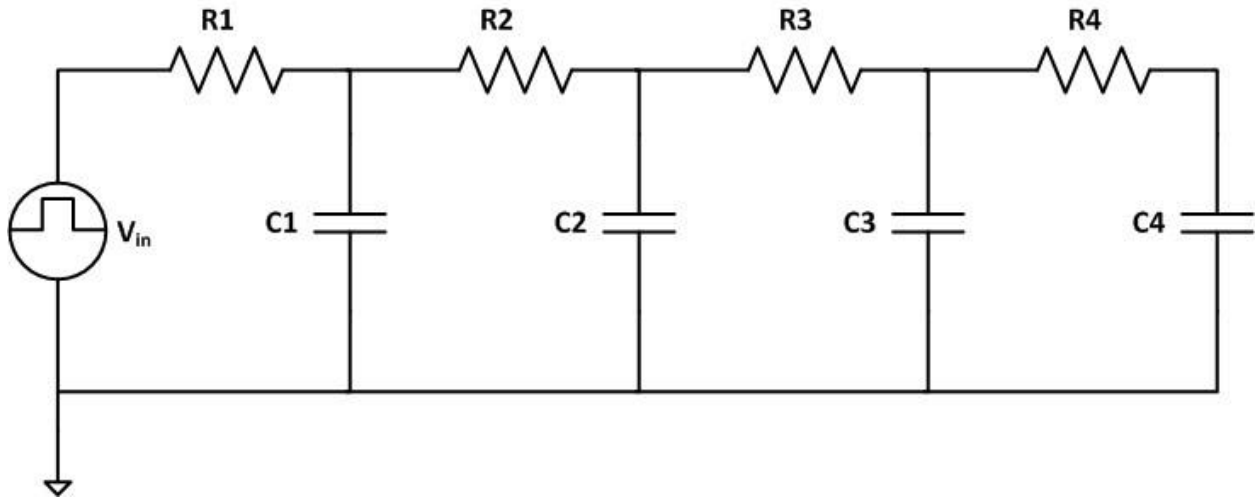


Figure 5.7 Equivalent circuit representation of a micropump with four PDMS membranes

Each of the four air chambers of the micropump have a different time constant because of the pressure loss of the compressed air along the interconnecting microchannel and the deflection of the membranes. According to the equivalent circuit analogy described in the previous sections, the PSPICE solution for voltage across each capacitor in the equivalent circuit is analogous to the actual pressure inside the corresponding air chamber. The results of the PSPICE transient response analysis of the equivalent circuit for 10 psi, 20 Hz operating conditions is shown in Figure 5.8. The plot is normalized against the source voltage and the period of the cycle. The first half of the plot (from  $t=0$  to  $t=0.025$  s) represents the charging of the capacitor (analogous to air pressure increasing within air chamber) and the second half of the plot represents the discharging of the capacitor (analogous to air pressure reducing within the air chamber). During

the first half of the plot (upstroke), the air pressure within each chamber rises from atmospheric pressure and gradually approaches the source pressure. It can be seen from the upstroke pressure curves that the air chambers fill up in a sequence, air chamber 1 filling up first, followed by air chambers 2, 3 and 4, leading to a peristaltic motion. At one time constant, which is the time taken by the capacitor to charge to 63% of its fully charged voltage, the time delay between the first, second and third air chambers is 3 ms, 1ms and 1ms respectively. The deflection of the PDMS membrane is directly proportional to the pressure inside the chamber and therefore the deflection curves for the membraness would have a similar trend as the pressure curves. Since the Chamber 1 has a much higher time constant than the rest of the chambers, the membrane in the Chamber 1 would deflect first and therefore also function as a valve that reduces any backflow. During the second half of the plot (downstroke), the pressure within the air chamber gradually drops from the source pressure to the atmospheric pressure. It can be seen from the downstroke pressure curves that the air chambers empty in a sequence.

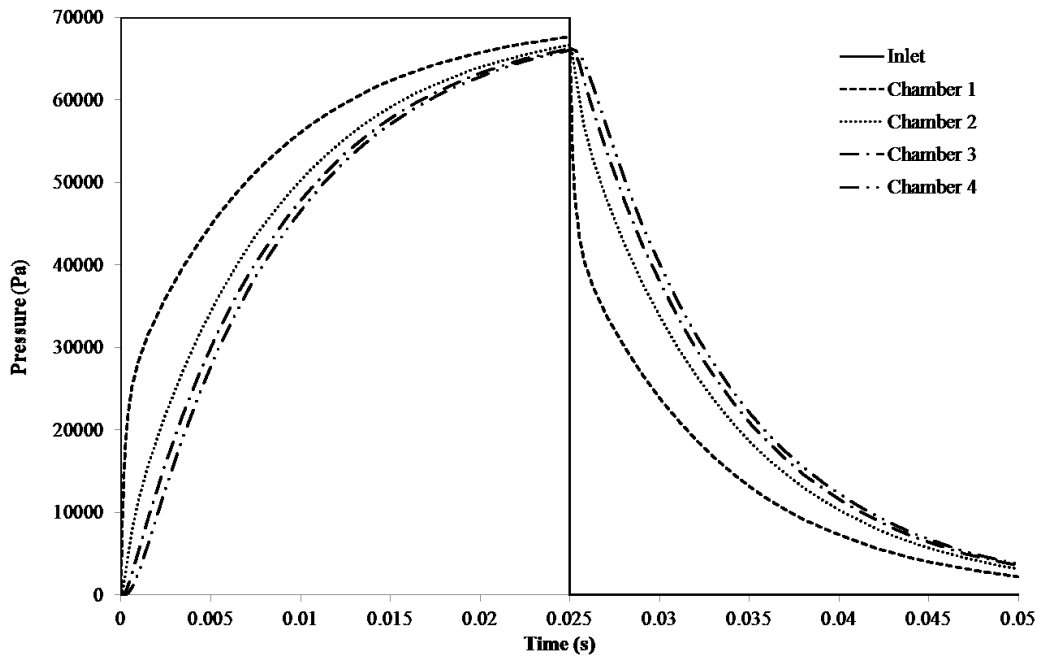


Figure 5.8 PSPICE transient response of the equivalent circuit

### 5.3 Micropump Simulation - COMSOL

The time delay obtained from the equivalent circuit simulation was used in performing a COMSOL simulation to verify the flow rate trend of the micropump. A 2D finite element simulation of the micropump was performed using the MEMS module of COMSOL Multiphysics™. The MEMS module includes a fluid-structure interaction (FSI) interface. The FSI interface couples fluid flow and solid mechanics using arbitrary Lagrangian-Eulerian (ALE) method to study the interaction between the fluid and the solid structure.

The fluid flow is described by the Navier Stokes equations to solve for velocity field,  $\mathbf{u} = (u, v)$ , and the pressure  $p$ , in the spatial (deformed) moving coordinate system:

$$\rho \frac{\partial \mathbf{u}}{\partial t} - \nabla \cdot [-p\mathbf{I} + \eta(\nabla \mathbf{u} + (\nabla \mathbf{u})^T)] + \rho((\mathbf{u} - \mathbf{u}_m) \cdot \nabla) \mathbf{u} = 0 \quad (5.6)$$

$$-\nabla \cdot \mathbf{u} = 0 \quad (5.7)$$

In the above equations,  $\mathbf{I}$  represents the unit diagonal matrix. The Navier Stokes equations are solved on a freely moving deformed mesh. The co-ordinate system velocity is  $\mathbf{u}_m = (u_m, v_m)$ . The structural deformations are solved using an elastic, non-linear geometry formulation to allow large deformations. The total force exerted on the fluid-solid boundary is given by:

$$\mathbf{F}_T = \mathbf{n} \cdot \{-p\mathbf{I} + (\eta(\nabla \mathbf{u} + (\nabla \mathbf{u})^T))\} \quad (5.8)$$

where  $\mathbf{n}$  is the normal vector to the boundary and  $\mathbf{F}_T$  represents a sum of pressure and viscous forces.

The 2D model of the micropump consists of three layers as shown in Figure 5.9. The lower most layer (shown in red) represents the rigid glass layer. The top most layer consists of a combination

of flexible PDMS membranes (M1, M2, M3 and M4 shown in blue) and rigid PDMS (shown in grey) layer. The middle layer represents the fluidic layer (shown in green). The width and the thickness of the four PDMS membranes were set to be 1500  $\mu\text{m}$  and 100  $\mu\text{m}$  respectively. The height of the glass layer and fluidic layer were set to 100  $\mu\text{m}$ . The fluidic layer was assigned the material properties of water with density, dynamic viscosity as 1000  $\text{kg/m}^3$  and 0.001  $\text{Ns/m}^2$  respectively. The glass layer was assigned material properties that include Young's modulus, Poisson's ratio, density equal to 72 GPa, 0.3 and 2500  $\text{kg/m}^3$  respectively.

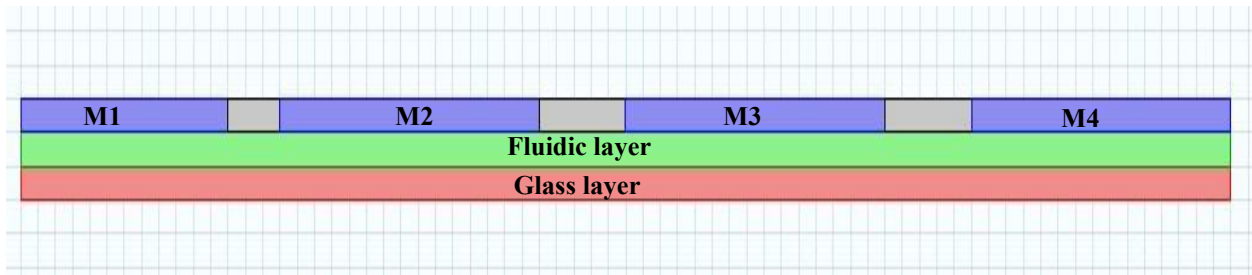


Figure 5.9 2D view of the micropump model with multiple layers

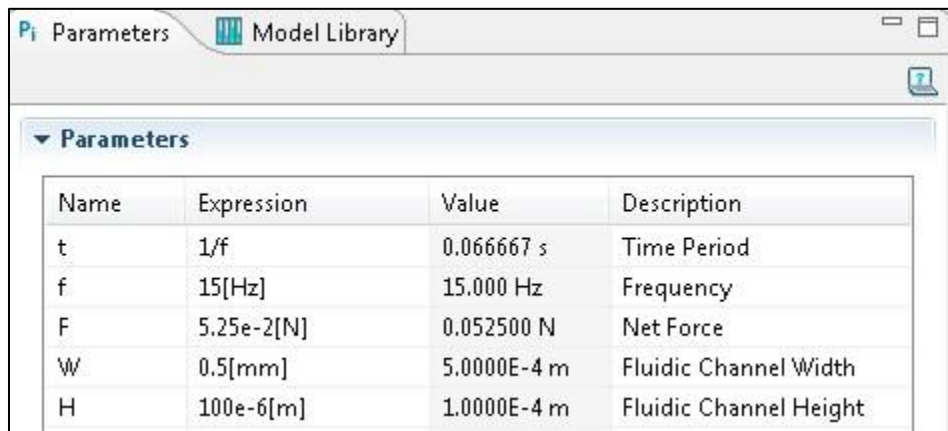
The PDMS layers were assigned material properties [174] that include Young's modulus, Poisson's ratio, and density equal to 75 MPa, 0.49, and 920  $\text{kg/m}^3$  respectively. Figure 5.10 shows a snapshot of the properties tab in COMSOL for defining material properties.

Material Contents				
Property	Name	Value	Unit	Property group
✓ Young's modulus	E	7.5e5	Pa	Basic
✓ Poisson's ratio	nu	0.49	1	Basic
✓ Density	rho	920	$\text{kg/m}^3$	Basic

Figure 5.10 Material properties of PDMS



The boundaries of fluid layer in contact with the PDMS and glass layers were assigned a fluid-solid interface boundary condition. The fluid layer domain was assigned a free deformation boundary condition. The boundaries of the PDMS membrane along the y-axis were assigned a fixed constraint. The boundaries of the rigid PDMS layers were assigned a fixed constraint. All the parameters including time period (t), frequency (f), fluidic channel width (W), fluidic channel height (H) and net force (F) were defined in the parameters settings under the global settings menu. Figure 5.11 shows a snapshot of the user input parameters tab in COMSOL.



The screenshot shows the 'Parameters' window in COMSOL. It contains a table with the following data:

Name	Expression	Value	Description
t	1/f	0.066667 s	Time Period
f	15[Hz]	15.000 Hz	Frequency
F	5.25e-2[N]	0.052500 N	Net Force
W	0.5[mm]	5.0000E-4 m	Fluidic Channel Width
H	100e-6[m]	1.0000E-4 m	Fluidic Channel Height

Figure 5.11 Definition of global parameters

Three square waveform functions, namely  $wv1$ ,  $wv2$ ,  $wv3$  and  $wv4$  were defined under the definitions menu. Figure 5.12 shows a screen shot of the definition of the waveform  $wv1$ . These square waveform functions can be invoked with angular frequency, phase and amplitude as variable parameters. Four boundary loads, namely Boundary Load 1, Boundary Load 2, Boundary Load 3 and Boundary Load 4 were defined on the PDMS membranes M1, M2, M3 and M4 respectively. The boundary loads were defined as time-dependent forces with total force defined as a product of the force and the respective square waveform function. For example, Boundary Load 1 was defined as  $-F \times wv1$ . The negative sign indicates that the force acts in

the negative y direction. Figure 5.13 shows an example of boundary load definition. The mesh settings were defined to be free triangular with a default fine element size set for fluid dynamics.

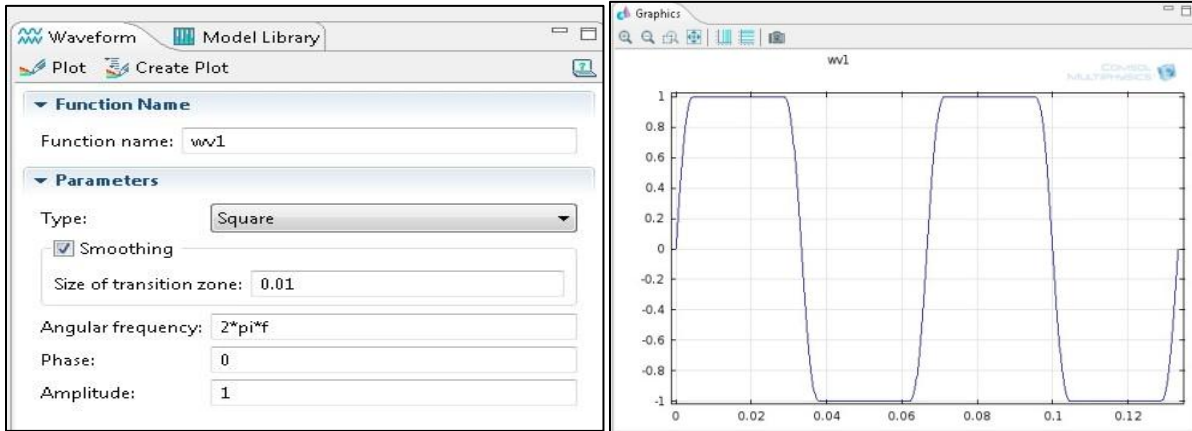


Figure 5.12 Waveform wv1 definition parameters and plot of waveform wv1

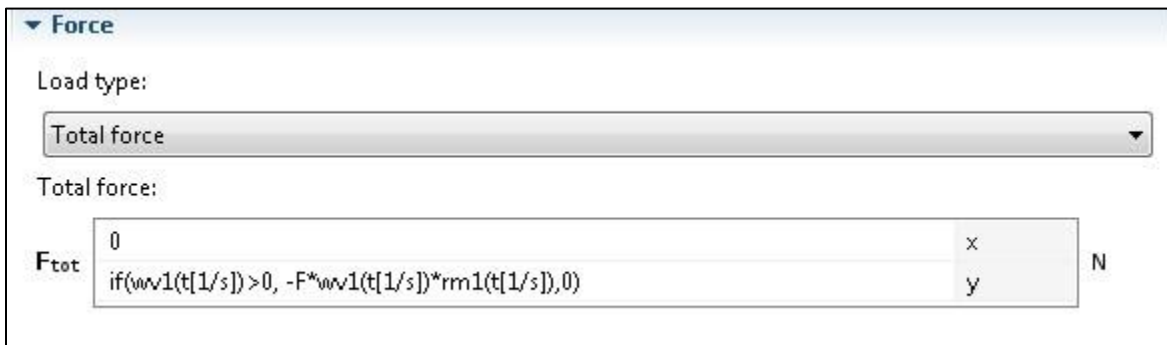
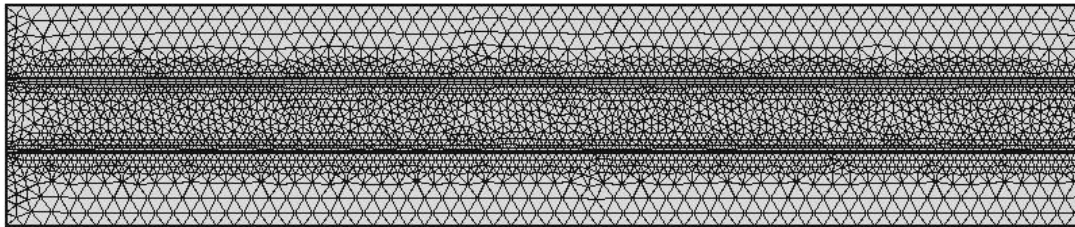
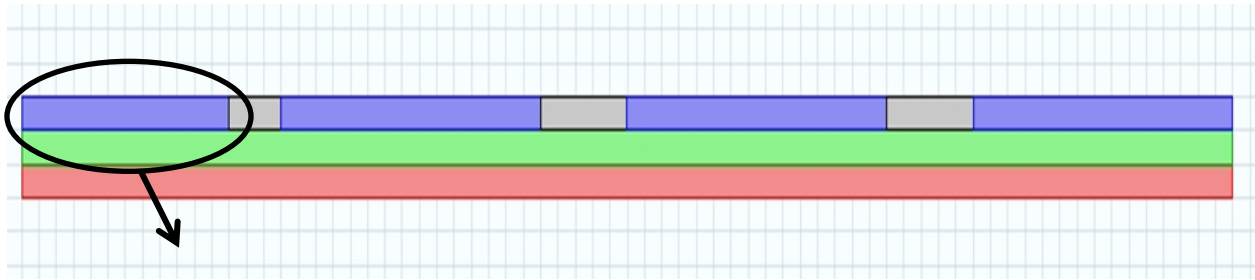
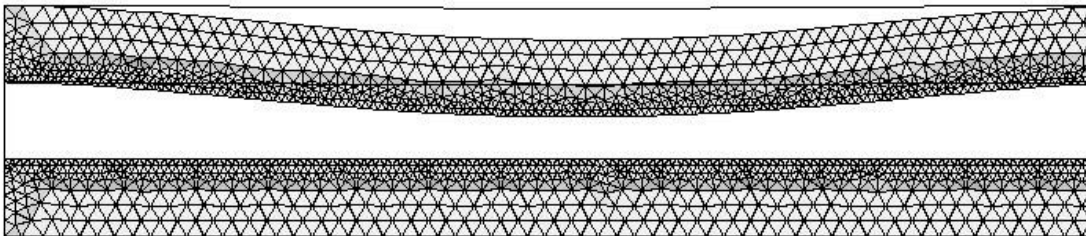


Figure 5.13 Boundary load definition

Figure 5.14 shows a close-up view of the mesh for the circled part of the model before and after deformation. A time dependent solver with 1 ms time stepping was used to obtain the solution for one time period. Figure 5.15 shows the change in displacement of the PDMS membrane plotted against the arc length of the PDMS membrane for various time instances, at 10 psi, 5 Hz operating conditions.



(a) Before deformation



(b) After deformation

Figure 5.14 Mesh diagram of membrane M1 before and after deformation

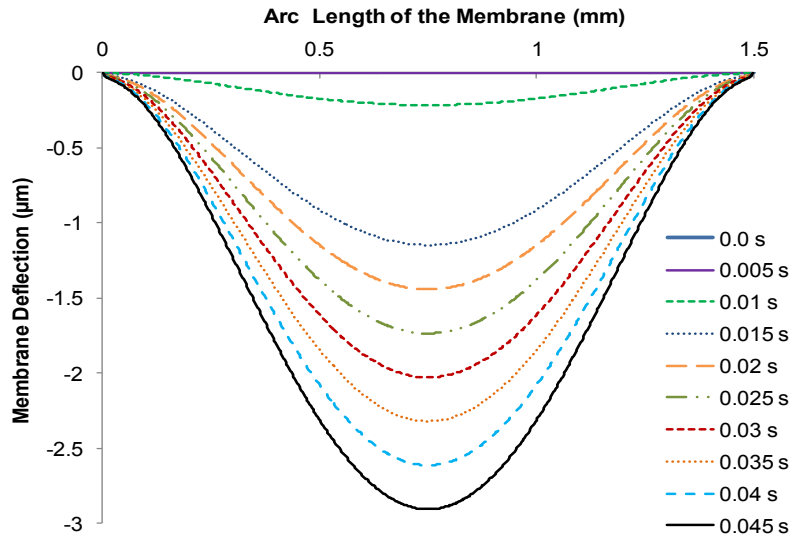


Figure 5.15 Membrane displacements vs. arc length of the membrane for various time instances

Figure 5.16 shows the change in displacement of all four PDMS membranes (M1, M2, M3 and M4) plotted against the arc length of the PDMS membrane at time  $t=0.01s$ , at 10 psi, 20 Hz operating conditions. It can be seen from the Figure 5.16 that there is a time delay between the deflections of the membranes.

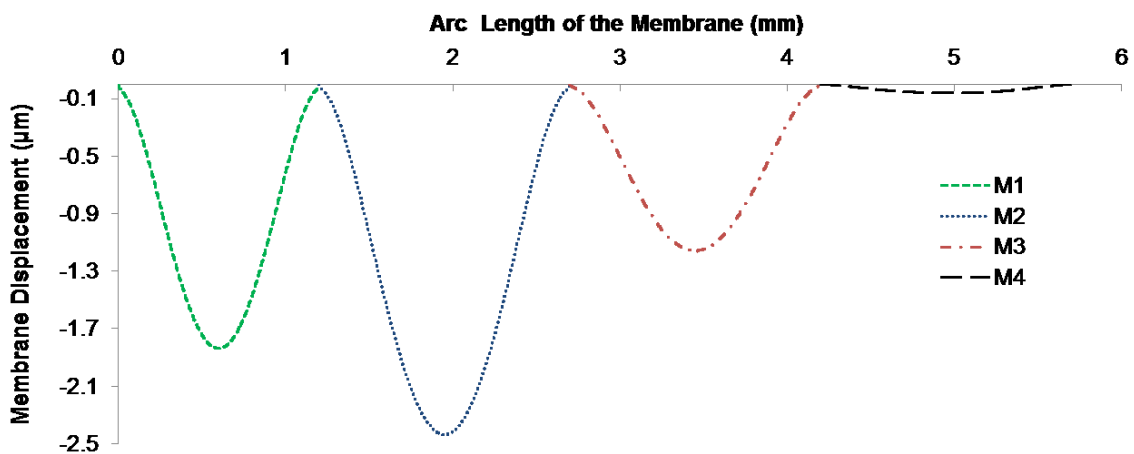


Figure 5.16 Membrane displacements vs. arc length of four membranes at  $t=0.01s$

At  $t = 0.01s$ , membrane displacement of M1, M2, M3 and M4 are  $1.8 \mu m$ ,  $2.4 \mu m$ ,  $1.15 \mu m$  and  $0.06 \mu m$  respectively. Membrane M1 deflects first and functions as a valve to reduce the back flow. The membranes M2, M3 and M4 have the same dimensions and are subjected to the same compressed air pressure of 20 psi. However, they show different membrane displacements due to the time delay between the actuation of the three membranes. This sequential deflection of the PDMS membranes leads to peristalsis causing the fluid underneath to flow. The flow rate was calculated in the post-processing by defining boundary integral to integrate velocity at the outlet boundary. Figure 5.17 shows a comparison of the average experimental flow rate and simulation flow rate obtained at 10 psi for a frequency ranging from 5 to 35 Hz.

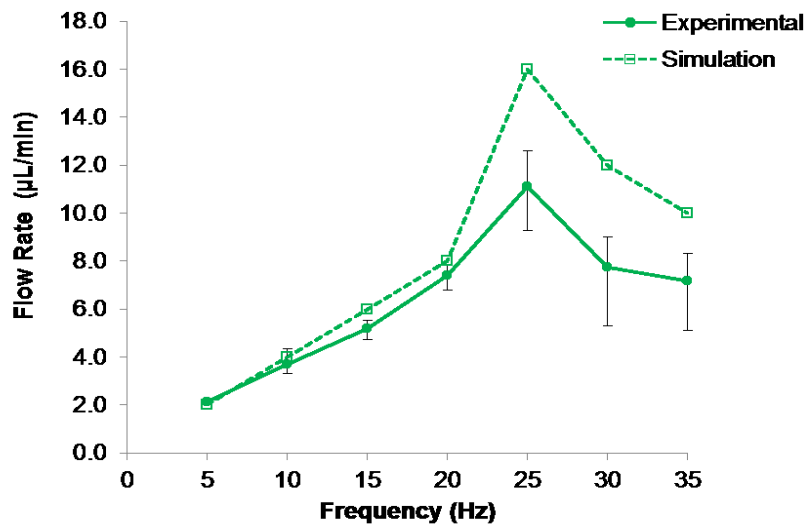


Figure 5.17 Experimental and simulation flow rates variation with frequency

The simulation flow rate with respect to frequency has a similar trend as that of the experimental results. The flow rate increases with frequency to reach a peak value at an optimum frequency, followed by a drop in flow rate for all frequencies higher than the optimum frequency. It can be observed from Figure 5.17 that in general the simulation flow rate results are higher than the experimental results. Also, the difference in simulation and experimental flow rates depends on

the frequency. The simulation model did not include the effects of pressure drop caused by the microfluidic connectors and external tubing connected to the outlet of the micropumps. The simulation model also does not include the pressure drop caused by the air bubbles generated within the fluidic layer of the micropump. The fluidic layer of the micropump was surface treated with Pluronic F108 which helps to reduce the generation of air bubbles but not completely eliminate them. It was also observed during the micropump performance testing that more air bubbles were generated at higher frequencies. This can cause a considerable pressure drop at higher frequencies which can cause the experimental flow rates to drop significantly.

#### **5.4 Performance of Micromixers**

The performance characteristics of three micromixer designs were experimentally determined. A qualitative test was first performed to compare the active mixing with diffusion mixing that occurs naturally when no external mixing is performed.

##### **5.4.1 Qualitative Testing**

The performance of the mixer was qualitatively tested for mixing of two colored dyes. The time taken for active mixing was compared with time for mixing purely by diffusion. Figure 5.18 shows the pictures of the dye mixing within the device by diffusion as time progresses. It takes 6 min for the two dyes to mix and reach one uniform color. Figure 5.19 shows the pictures of the two dyes mixing within the device by active mixing caused by the deflecting membranes of the micromixer as time progresses. It took only 20 s to complete the mixing process by active mixing and mixing time is 18 times shorter than mixing by pure diffusion. These results indicate that the designed active micromixers are effective in reducing mixing times.

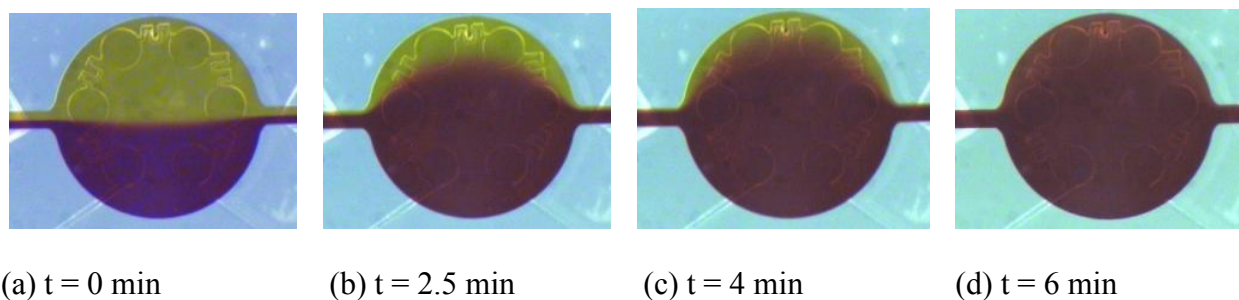


Figure 5.18 Diffusion only mixing at various time instants

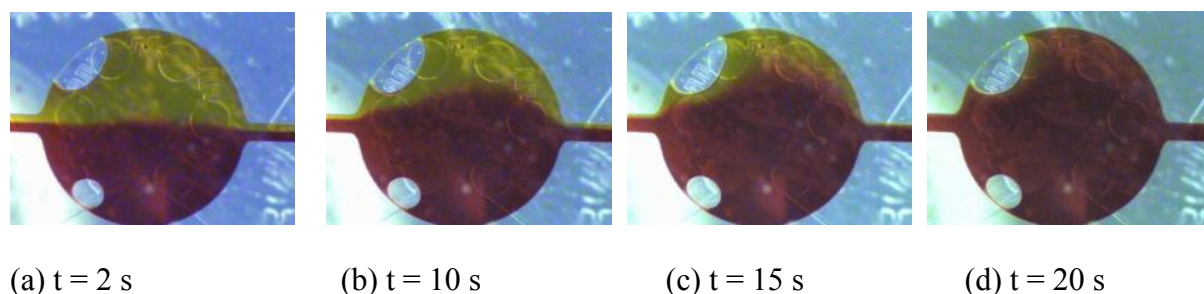


Figure 5.19 Active mixing at various time instants

#### 5.4.2 Comparison with Table Top Mixer

The mixing process at micro scale using the micromixer was compared with the macro scale mixing using the table top mixer. A micromixer and a table top mixer were used to mix SCP beads and BCF beads in order to achieve a streptavidin-biotin conjugation reaction. The relative increase in conjugation reactions due to active mixing methods when compared to mixing by pure diffusion alone (control) is shown in Figure 5.20 for micromixer and a table top mixer. The intensity of fluorescence signal is a direct measure of the extent of mixing. Both micromixers and table top mixers resulted in a significant increase in fluorescence signal. This clearly indicates the need for active mixing on both micro and macro scale for streptavidin-bioin conjugation reaction, and confirms that agitation of the flow improves binding efficiency. Due to the absence of turbulence in microfluidic systems, unless some form of flow agitation by active

mixing is present, mixing can only happen by diffusion. In case of micromixers, there was a 45% increase in the fluorescence signal due to active mixing, whereas in case of the table top mixer, there was only a 15% increase. These results indicate that active mixing at micro scale can improve the mixing performance.

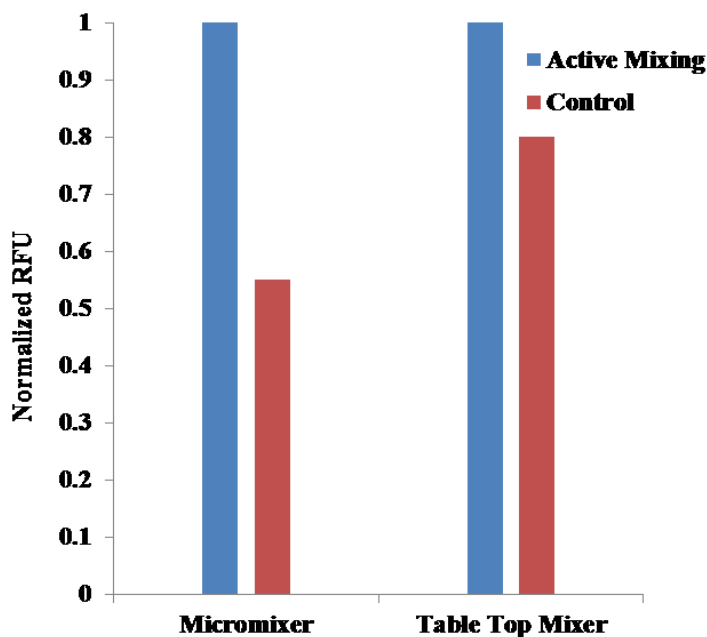


Figure 5.20 Increase in binding efficiency using a micromixer and table top mixer

### 5.4.3 Mixing Performance Variation with Frequency

Figure 5.21 shows a normalized plot of the average RFU with respect to frequency for the three micromixer designs tested three times. The actuation frequency was varied from 5 – 20 Hz at a constant flow rate of 2  $\mu\text{L}/\text{min}$  and a compressed air pressure of 20 psi. The mean variation in RFU with respect to average RFU for a micromixer of Design 3 was 3.3%, with a maximum variation of 4.2% and a minimum variation of 2.56%. The mean variation in RFU for a micromixer of Design 2 with respect to average RFU was 8.27%, with a maximum variation of 13.03% and a minimum variation of 2.87%. The mean variation in RFU with respect to average



RFU for a micromixer of Design 1 was 12.9%, with a maximum variation of 15.3% and a minimum variation of 9.66%. Design 3 has the best mixing performance when compared to other designs during the frequency test. The peak RFU signal obtained for Design3 is 70% higher than Design2. In case of Design1, there was no significant change in RFU with change in frequency.

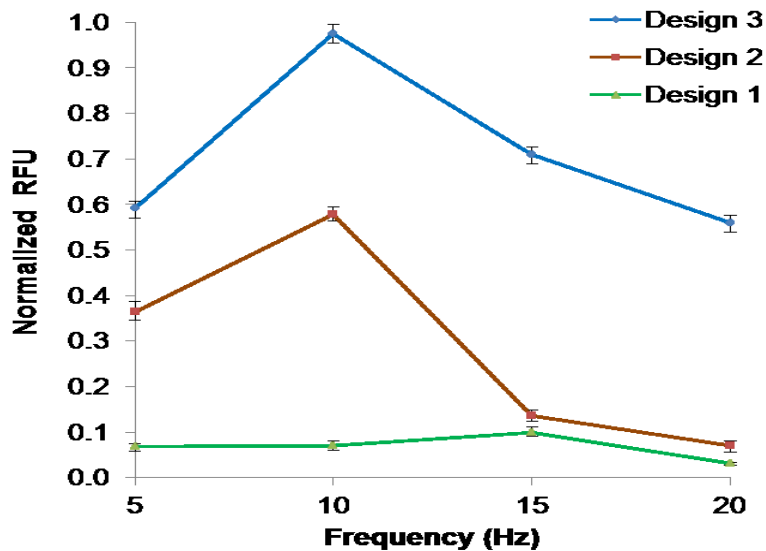


Figure 5.21 Normalized RFU vs Frequency for three mixer designs

As the actuation frequency increases, the agitation within the mixing chamber increases and results in an increase in the streptavidin-biotin conjugation reaction until an optimal frequency is reached. The reduction in conjugation reaction at higher frequencies beyond the optimal frequency can be attributed to the response time of the membrane. At higher frequencies, there is insufficient time for the air chamber to be completely filled and exert pressure on the membrane to actuate it.

#### 5.4.4 Mixing Performance Variation with Flow Rate

The mixing performance was tested three times with respect to change in flow rate for the three micromixer designs. The flow rate range was varied from 1.2 – 4  $\mu\text{L}/\text{min}$  at a constant frequency of 10 Hz and a constant compressed air pressure of 20 psi. Figure 5.22 shows the normalized plot of the average RFU with respect to flow rate for the three micromixer designs.

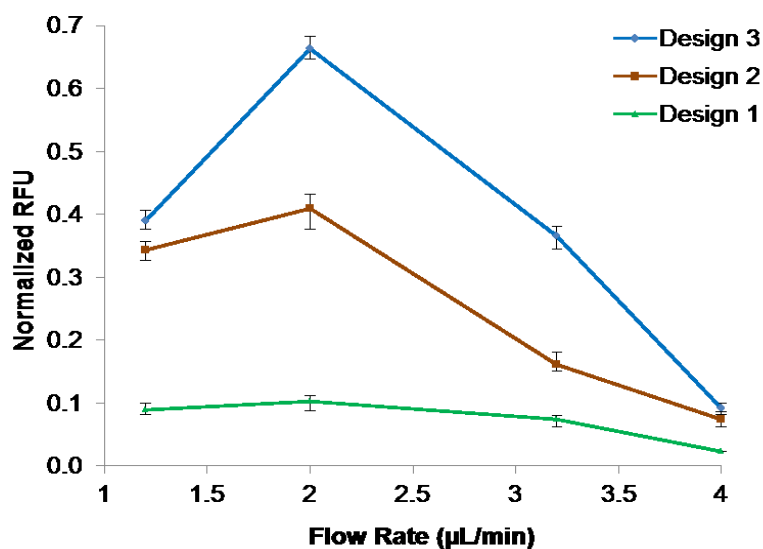


Figure 5.22 Normalized RFU vs. Frequency for individual mixer designs

It can be observed that the streptavidin-biotin conjugation reaction increases with the flow rate until it reaches a peak value. The mean variation in RFU with respect to flow rate for a micromixer of Design3 was 6.33%, with a maximum variation of 12.9% and a minimum variation of 3.13%. The mean variation in RFU with respect to average RFU for a micromixer of Design2 was 9.13%, with a maximum variation of 13.92% and a minimum variation of 4.82%. The mean variation in RFU with respect to average RFU for a micromixer of Design1 was 10.29%, with a maximum variation of 14.29% and a minimum variation of 3.85%.

As the flow rate increases, the microbeads' retention time in the mixer is reduced and the microbeads thus have less time to interact with each other, which reduces streptavidin-biotin conjugation reaction. However, at the lowest flow rate (1.2  $\mu\text{L}/\text{min}$ ), which corresponds to the largest retention time, the conjugation efficiency is the lowest. This is most likely due to the absence of recirculating eddies which occur only at higher Reynolds numbers ( $\text{Re}$ ). The backwards flow and re-circulation of the fluid in these eddies allows more time within the mixing chamber for the beads to interact with each other and increases flow agitation, thus increasing streptavidin-conjugation reaction. At 1.2  $\mu\text{L}/\text{min}$ ,  $\text{Re} \sim 0.01$  and the flow falls in the range of Stokes flow which closely follows the contour of the mixing chamber without recirculation. The recirculation phenomenon depends on the Reynolds number, and the channel geometry is the same for all designs. Therefore, the differences in designs do not significantly affect the flow rate at which peak mixing efficiency occurs. The highest mixing performance was observed at 2  $\mu\text{L}/\text{min}$ . Design3 has the best mixing performance with respect to flow rate. At 2  $\mu\text{L}/\text{min}$ , the peak RFU value of Design3 is 70% higher than Design2. Design1 did not show any significant variation in performance with change in flow rate. Based on the highest performance of Design3 with respect to both frequency and flow rate, Design3 was selected to be incorporated into the fully integrated microfluidic system.

Despite the numerous recent works on micromixers, characterization of micromixers still remains a challenge [175]. Micromixers are commonly characterized based on three nondimensional fluid parameters:  $\text{Re}$ , Péclet number ( $\text{Pe}$ ), and Strouhal number ( $\text{St}$ ) [176]. Péclet number is a measure of the relative importance of advection and diffusion in providing the mass transport associated with the mixing.  $\text{Pe}$  is defined as

$$\text{Pe} = \frac{UL}{D} \quad (5.9)$$

where  $U$  is the velocity of the fluid,  $L$  is the mixing path which is on the same order of the height of the mixing chamber in this study and  $D$  is the diffusivity of the fluids. Strouhal number is generally associated with active mixers and represents the ratio between the residence time of a species and the time period of disturbance.  $St$  is defined as:

$$St = \frac{fD_h}{U} \quad (5.10)$$

where  $f$  is the frequency of the disturbance action and  $D_h$  is the hydraulic diameter. The optimum mixing efficiency occurs at a frequency of 10 Hz and a flow rate of 2  $\mu\text{L}/\text{min}$ . The characteristic  $Pe$ ,  $St$  and  $Re$  values of the micromixer to perform at the optimum mixing efficiency conditions were calculated to be 11.2, 17.5 and 0.02 respectively.

A magnetic particle driven micromixer design has been reported [177] with a mixing performance dependence on driving frequency similar to the one observed in this study. The peak mixing efficiency was observed at an optimum frequency of 20 Hz. A microfluidic electroosmotic mixer has been reported [178] with a study on the effect of frequency on the mixing efficiency. The performance curve for variation of mixing efficiency with frequency, with a peak mixing efficiency at an optimum frequency of 22 Hz, is similar to the one observed in this study.

### **5.5 Performance of Integrated Micromixer and Micropump**

A micropump (Design3) and micromixer (Design3) were integrated on a single device to obtain an integrated micromixer-micropump and tested for mixing efficiency based on streptavidin biotin conjugation reaction. Mixing efficiency was calculated by comparing the RFU values of 20  $\mu\text{L}$  volumes of fluorescent bead sample with the RFU value of 20  $\mu\text{L}$  of the post mixing sample after magnetic separation/washing step. Figure 5.23 (a) and (b) shows the normalized

plot of average RFU and mixing efficiencies for a frequency range of 5 to 25 Hz. The mean variation in RFU with respect to average RFU is 4.08%, with a maximum variation of 5.4% and a minimum variation of 2.4%. A maximum mixing efficiency of 83.3 % was observed at 10 Hz.

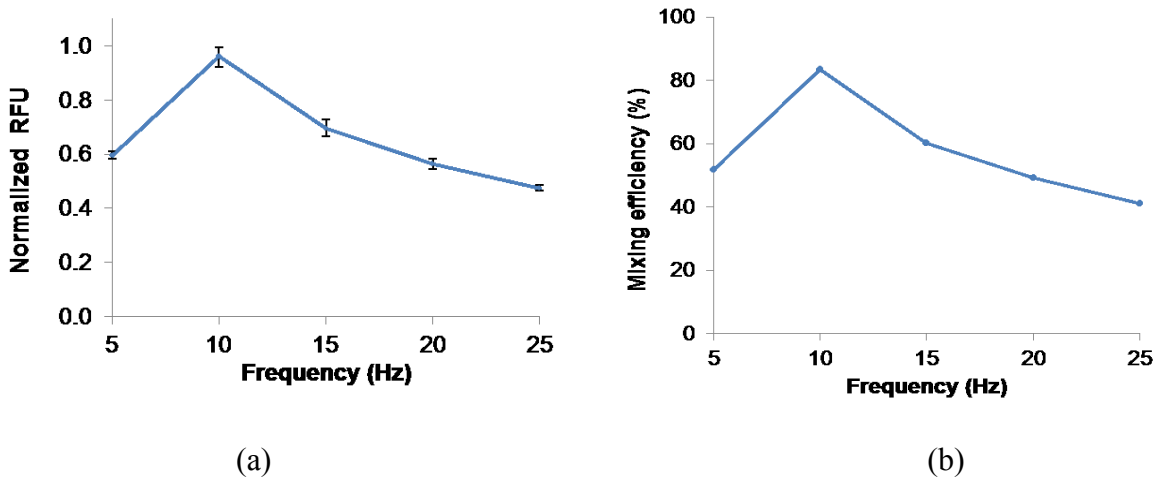
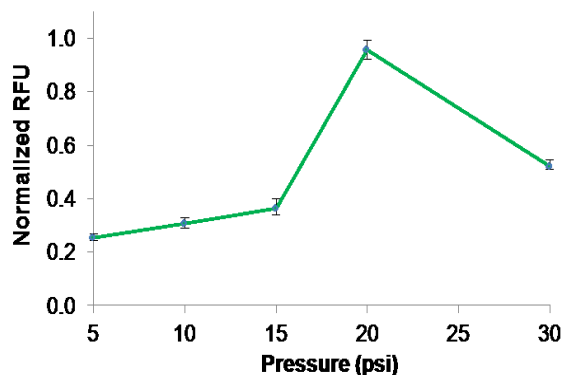
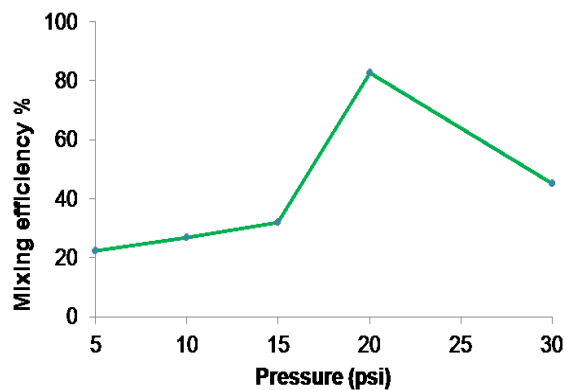


Figure 5.23 (a) Normalized RFU vs Frequency (b) Mixing efficiency vs Frequency

Figure 5.24 (a) and (b) shows the normalized plot of average RFU and mixing efficiencies for a pressure range of 5 to 30 psi. The mean variation in RFU with respect to average RFU is 6.7%, with a maximum variation of 10.5% and a minimum variation of 3.4%. A maximum mixing efficiency of 82.8 % was observed at 20 psi. Figure 5.25 (a) and (b) shows the normalized plot of average RFU and mixing efficiencies for a flow rate range of 1 to 6  $\mu\text{L}/\text{min}$ . The mean variation in RFU with respect to average RFU is 6.58%, with a maximum variation of 11.5% and a minimum variation of 2.66%. A maximum mixing efficiency of 82.1 % was observed at 2  $\mu\text{L}/\text{min}$ .

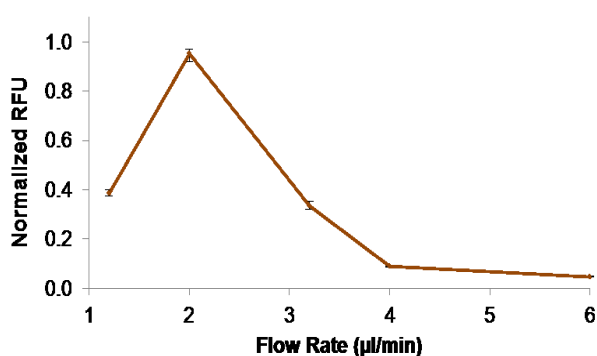


(a)

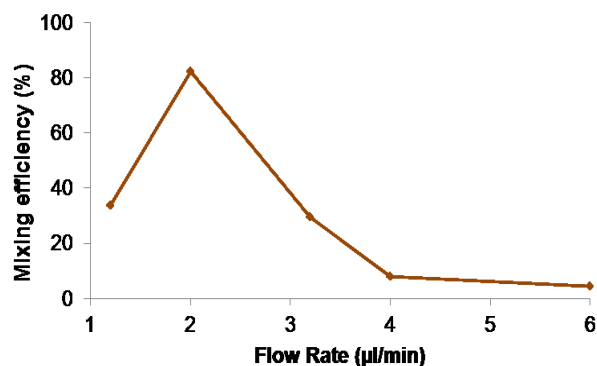


(b)

Figure 5.24 (a) Normalized RFU vs. pressure (b) Mixing efficiency vs. pressure



(a)



(b)

Figure 5.25 (a) Normalized RFU vs. flow rate (b) Mixing efficiency vs. flow rate

Based on the performance testing results, the optimum operating conditions for obtaining the highest mixing performance is 2  $\mu\text{L}/\text{min}$  sample flow rate, 10 Hz actuation frequency and a compressed air pressure of 20 psi. The micromixer was operated under these conditions for all further testing.

## 5.6 Magnetic Microbead Separation Scheme

The testing for magnetic microbead separation included both electromagnets and permanent magnets of various sizes and magnetic strengths.

### 5.6.1 Electromagnets

Three electromagnets of different size and strength, namely EM1, EM2 and EM3 were tested. In case of electromagnets EM1 and EM3, it was not possible to capture all the SCP beads even at a SCP bead sample flow rate of 1  $\mu\text{L}/\text{min}$ . The magnetic field strength generated by EM1 and EM3 was not sufficient enough to overcome the hydrodynamic drag force. In case of EM2, it was possible to capture SCP beads successfully up to a bead sample flow rate of 1.5  $\mu\text{L}/\text{min}$ . The magnetic force exerted on the SCP bead was calculated using Equation 2.2 for all three electromagnets selected. The hydrodynamic drag force on the SCP beads was calculated for various flow rates using Equation 2.3. The hydrodynamic drag force for flow rates in the range of 1-10  $\mu\text{L}/\text{min}$  and magnetic force exerted by three electromagnets is shown in Figure 5.26.

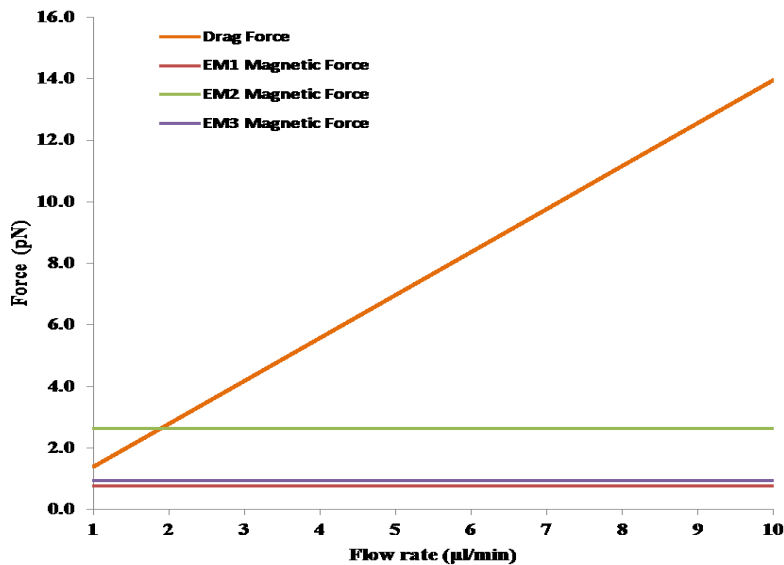


Figure 5.26 Comparison of magnetic field strengths of electromagnets with drag force

It can be seen from Figure 6.18 that EM1 and EM3 can generate a magnetic force of 0.76 pN and 0.73 pN which are not sufficient to overcome the hydrodynamic drag force of 1.4 pN at a flow rate of 1  $\mu\text{L}/\text{min}$ . EM2 can generate a magnetic force of 2.6 pN which is enough to overcome the hydrodynamic drag force up to 1.5  $\mu\text{L}/\text{min}$ . In case of EM2 which could be used up to 1.5  $\mu\text{L}/\text{min}$ , it was not possible to obtain repeatable results as the top surface of the electromagnet was not perfectly flat and it wasn't possible to make a uniform contact with the bottom surface of the microfluidic system. The setup required a mini lab jack to raise the electromagnet and bring it in contact with the device under test and was also very sensitive to any movements of the device while in operation. The large diameters of the electromagnet would also require the microfluidic connectors to be placed wider apart to provide enough space to position the electromagnets in contact with the mixing chamber of the device. The electromagnets tested had insufficient magnetic field strengths and even when successful at very flow rates could not provide repeatable results. Due to these limitations and disadvantages, the electromagnet approach to capture SCP beads was not suitable.

### **5.6.2 Permanent Magnets**

Three permanent magnets of various size and strengths, namely PM1, PM2 and PM3 were tested. In case of permanent magnet PM3, it was possible to capture the SCP beads up to a sample flow rate of 1.5  $\mu\text{L}/\text{min}$ . In case of permanent magnets PM1 and PM2, it was possible to capture the SCP beads up to 10  $\mu\text{L}/\text{min}$ . The hydrodynamic drag force and magnetic force exerted by the permanent magnets was calculated using Equation 3.1 and Equation 3.2 respectively. Figure 5.27 shows that PM3 can generate a magnetic force of 2.05 pN which can overcome the hydrodynamic drag force up to a flow rate of 1.5  $\mu\text{L}/\text{min}$  only. PM1 and PM2 can



generate a magnetic force of 16.5 pN and 24.0 pN respectively and can overcome the hydrodynamic drag forces up to 10  $\mu\text{L}/\text{min}$ .

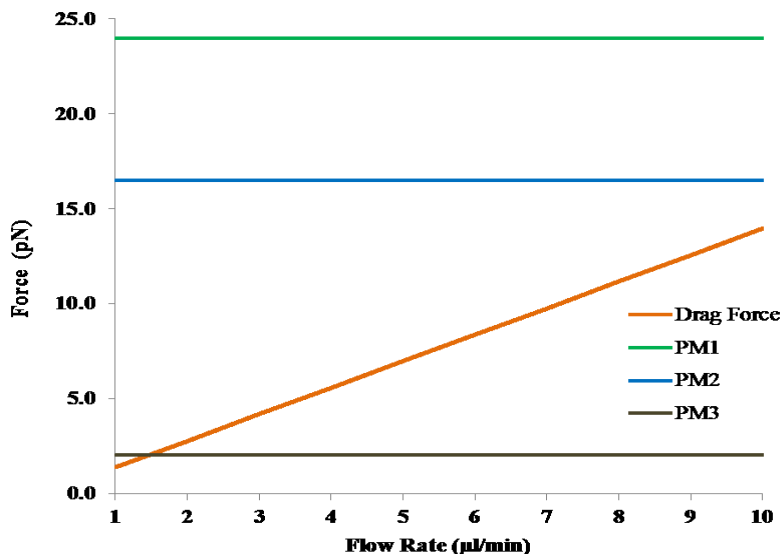


Figure 5.27 Comparison of magnetic field strengths of permanent magnets with drag force

Figure 5.28 (a) shows a top view of an empty mixing chamber of a microfluidic channel with a permanent magnet placed below it and before a bead sample was injected into the device. Figure shows the empty mixing chamber and mixing chamber with the trapped beads after the SCP beads were injected into the device at a flow rate of 10  $\mu\text{L}/\text{min}$ . The periphery of the circular mixing chamber can be seen and the group of trapped SCP beads appears with an orange shade in the Figure 5.28 (b). Based on these results, permanent magnet PM1 was selected for all magnetic separations within the microfluidic channel as the magnetic flux density was high enough to capture moving beads up to a flow rate of 10  $\mu\text{L}/\text{min}$ . Also, the small size of PM1 with a diameter of 4.8 mm and a thickness of 3.2 mm makes it compact and easier to integrate with the microfluidic device without interfering with the fluidic connectors.

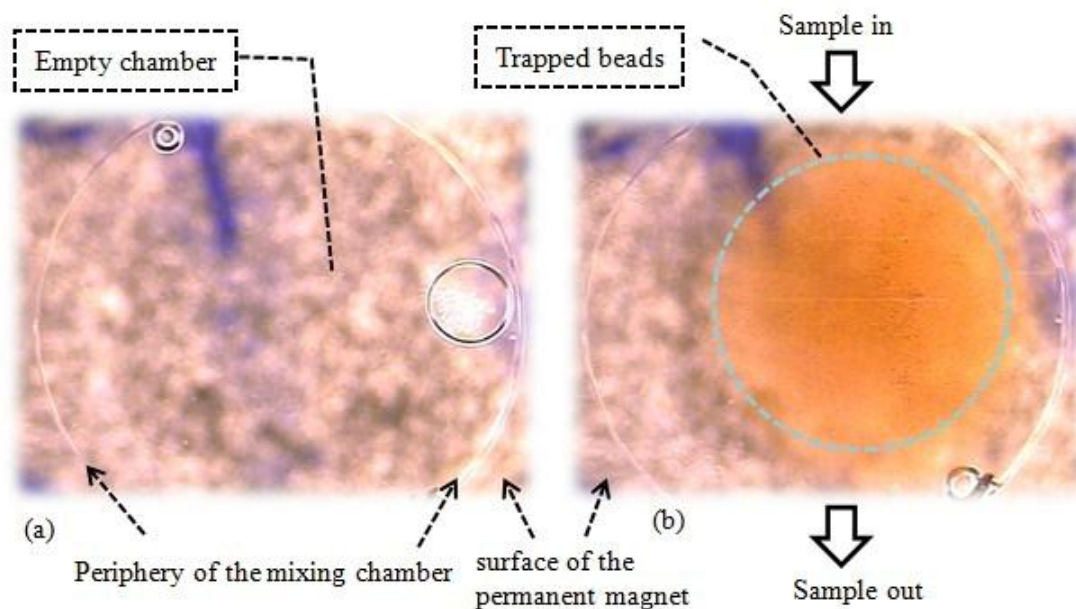


Figure 5.28 Images of the mixing chamber with a permanent magnet in the background (a) Before the beads were injected into the circular mixing chamber (b) after beads were injected with trapped beads (appears orange in color) inside the mixing chamber

## 5.7 Integrated Microfluidic System Testing

Two different testing protocols were employed to evaluate the performance of the integrated microfluidic system. In the first test, the integrated microfluidic system was used for detection of biotin coated microbeads. In the second test, the integrated microfluidic system was used for immune based microbead insulin detection.

### 5.7.1 Impedance Detection of BCF Microbeads

Impedance spectrum results are commonly represented in a Bode plot format, where the magnitude of the impedance (log scale) is plotted on the y-axis and frequency on the x-axis (log scale). Figure 5.29 shows the impedance spectrum (Bode plot representation) for all concentrations of BCF beads ranging from  $1.9 \times 10^5$  to  $4.8 \times 10^6$ . The magnitude of impedance increased with increase in the number of BCF beads. In order to determine the frequency at

which the maximum change in absolute impedance between the BCF beads and the control was obtained, a curve was drawn between normalized impedance change (NIC) and frequency. NIC was defined by the following equation:

$$NIC = \frac{Z_{sample} - Z_{control}}{Z_{control}} \times 100 \quad (5.11)$$

where  $Z_{control}$  is the absolute impedance of the control and  $Z_{sample}$  is the absolute impedance of the sample containing BCF beads.

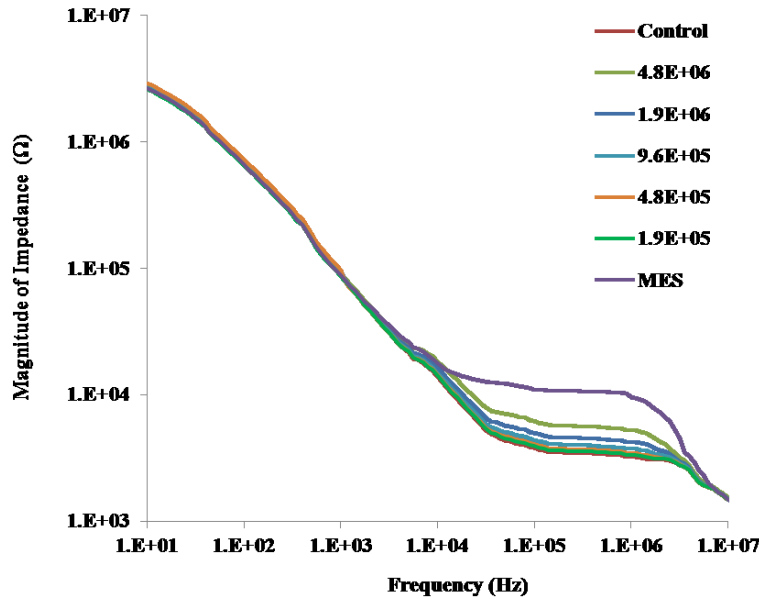


Figure 5.29 Impedance spectrum (Bode plot) for different concentrations of BCF beads

As shown in Figure 5.30, the impedance change (represented by NIC) showed an increase from 5% to 63% in the frequency range from 1 kHz to 80 kHz, remained constant at 63% in the frequency range from 80 kHz to 1 MHz, and then decreased from 63% to 3% at higher frequencies. A mid-frequency value of 200 kHz where a peak NIC was observed was selected to

compare the impedance changes for all concentrations of BCF beads. The magnitude of impedance measured (three replicates) at 200 kHz for different concentrations of BCF beads from  $1.9 \times 10^5$  beads to  $4.8 \times 10^6$  beads is shown in Figure 5.31. It can be observed that there is no significant difference in impedance between control (SCP beads) and concentrations  $1.9 \times 10^5$  and  $4.8 \times 10^5$  microbeads. The difference in impedance with respect to control for a concentration of  $1.9 \times 10^5$  microbeads and  $4.8 \times 10^5$  microbeads was 3% and 7% respectively.

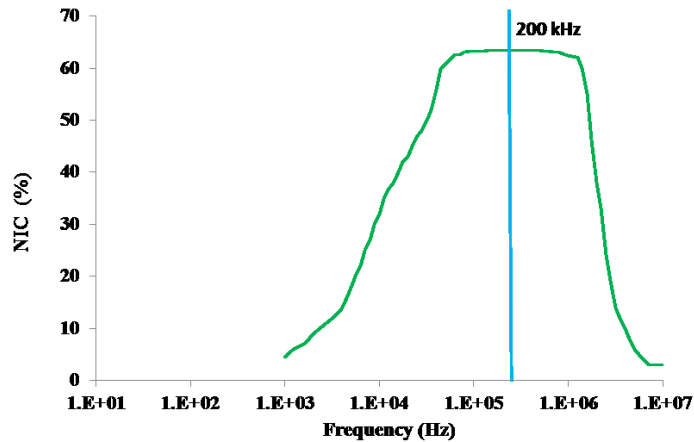


Figure 5.30 The difference in magnitude of impedance (represented by NIC) between  $4.8 \times 10^6$  BCF beads and control sample. NIC was calculated for the measurements in the range of frequency from 1 KHz to 10 MHz.

The difference in impedance with respect to control for concentrations  $9.6 \times 10^5$  microbeads,  $1.9 \times 10^6$  and  $1.9 \times 10^6$  microbeads was observed to increase linearly and was 16%, 32% and 63% respectively. There is no detectable and repeatable change in impedance between  $4.8 \times 10^5$  and  $9.6 \times 10^5$ . The lower detection limit for BCF microbeads is  $1.9 \times 10^6$  microbeads. The experimental data of an impedance biosensor for the detection of BCF beads attached to SCP beads is represented by an equivalent circuit as shown in Figure 5.32 [179-180]. The equivalent circuit consists of two double layer capacitors (CPE), one for each set of the electrodes,

resistance of medium ( $R_s$ ), and a stray capacitance ( $C_s$ ) connected in parallel. Constant phase element (CPE) is used to model the double layer capacitance of the electrodes.

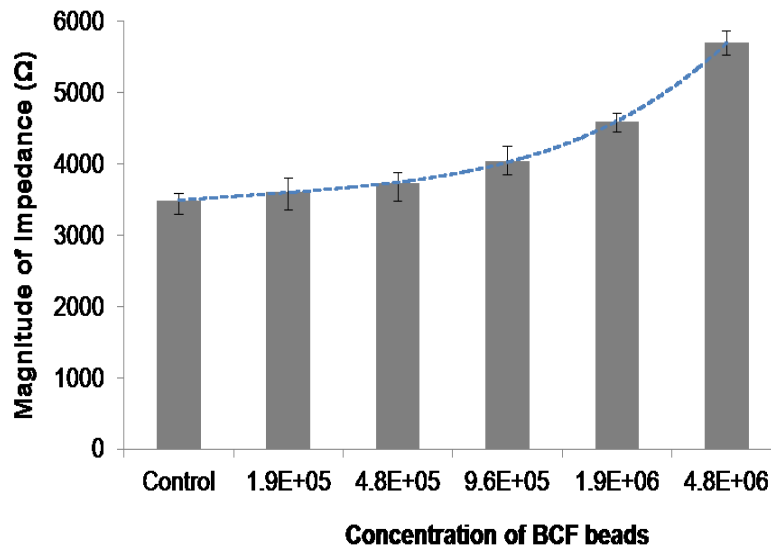


Figure 5.31 Magnitude of impedance at 200 kHz for various concentrations of BCF beads

This is commonly favored over the use of a simple capacitor [181]. CPE accounts for the effect of ionic species on the capacitance near the surface of an electrode.  $R_s$  accounts for change in conductivity and charge transport across the bulk medium.  $C_s$  represents the stray capacitance of the impedance measurement system associated with electrodes, shielding, wiring and connecting cables and chrome adhesion layer between gold and glass. The total impedance of the equivalent circuit can be expressed by the following equations:

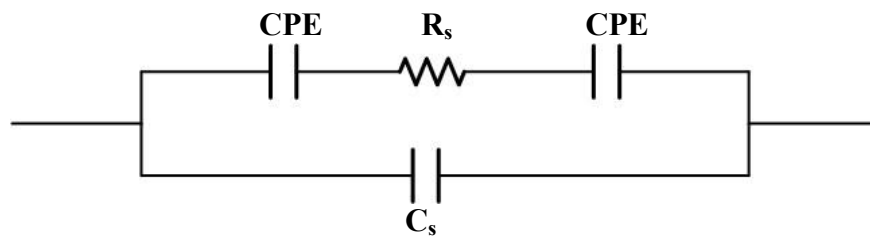


Figure 5.32 Equivalent circuit for impedance measurement system

$$|Z_1| = \sqrt{R_s^2 + \frac{1}{(\pi f CPE)^2}} \quad (5.12)$$

$$|Z_2| = \sqrt{\frac{1}{(2\pi f C_s)^2}} \quad (5.13)$$

$$\frac{1}{Z_{total}} = \frac{1}{Z_1} + \frac{1}{Z_2} \quad (5.14)$$

where  $Z_1$  and  $Z_2$  are the impedance of the two branches of the equivalent circuit containing (CPE +  $R_s$  + CPE) and  $C_s$  respectively.  $Z_{view}$  software (Scribner Associates Inc., Southern Pines, NC) was used to fit the experimental impedance data to the chosen equivalent circuit model. The fitting was performed by the software using complex non-linear least-square method. Figure 5.33 shows the bode plot of the experimental and fitted data from  $Z_{view}$  software based on equivalent circuit.

There are three distinct regions in the impedance spectrum which correspond to the three types of elements in the equivalent circuit. The double layer region is in the low frequency range from 10 Hz to approximately 30 kHz, where the double layer capacitance of the electrodes represented by CPE dominates the impedance signal. For frequency ranging from 30 kHz to 1 MHz, conductivity of the medium is the key factor and the bulk medium resistance determines the signal. At a frequency greater than 1MHz is the dielectric region where the signal is dominated by the stray capacitance of the system.

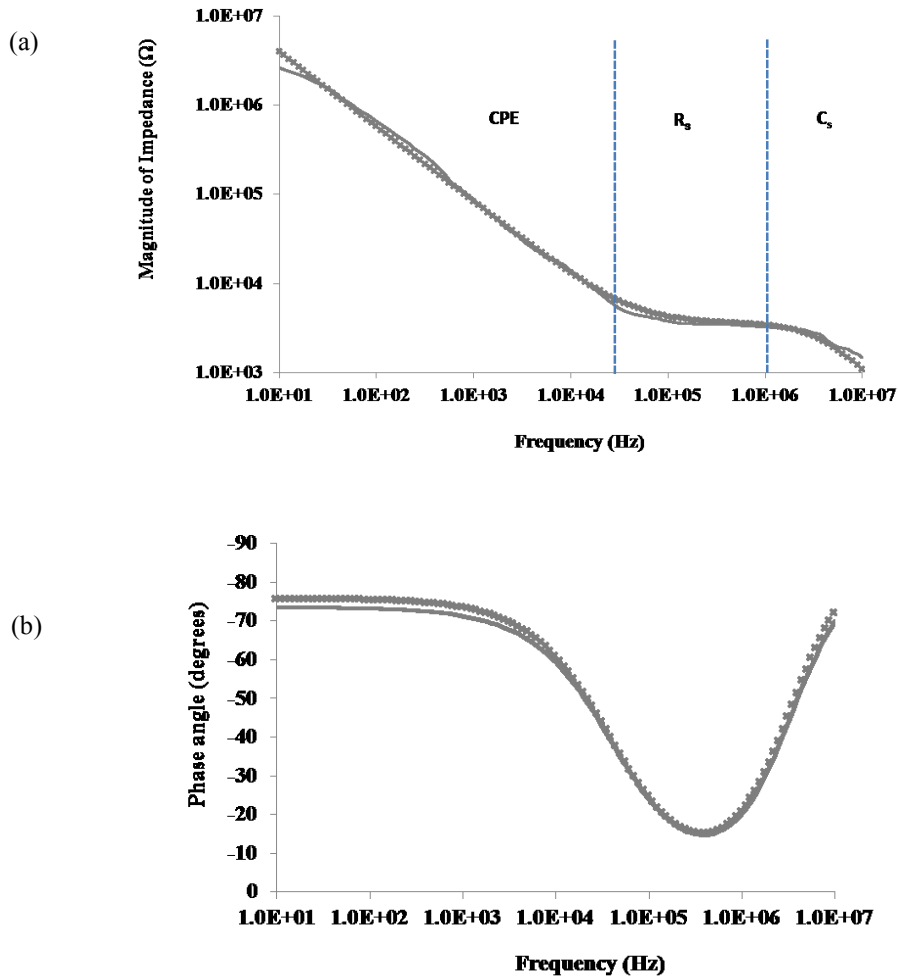


Figure 5.33 Bode plots of the impedance spectra of experimental and curve fitted data of control in the frequency range 10 Hz to 10 Mhz. Solid lines indicate the experimental data and crosses indicate the fitted data obtained from Zview software based on the the equivalent circuit. (a) Magnitude of impedance (b) Phase angle in degrees

The division of the impedance spectrum into three distinct regions can be further analyzed with the help of the phase angle spectrum shown in Figure 5.33 (b). An electrical current passing through a capacitor is phase shifted by  $-90^\circ$  with respect to the applied voltage. The phase angle in a capacitance dominated region of the impedance spectrum is therefore close to  $-90^\circ$ . The current passing through a resistor is always in phase with the applied voltage. Therefore the phase angle in resistance dominated region of the impedance spectrum is close to  $0^\circ$ . As shown

in Figure 5.33 (b), the phase angle is close to  $-90^\circ$  on both ends of the impedance spectrum, and close to  $0^\circ$  in the middle. It can thus be concluded that both the low and high frequency spectra are dominated by a capacitance while the mid frequency region by a resistance. The simulated values of  $R_s$ , CPE and  $C_s$  in the equivalent circuit for control sample and sample with  $4.86 \times 10^6$  BCF microbeads are listed in Table 5.3. These values were obtained by curve fitting the respective experimental impedance data to the equivalent circuit.

<b>Sample</b>	<b><math>R_s</math> (k<math>\Omega</math>)</b>	<b>CPE (nF)</b>	<b><math>C_s</math>(pF)</b>
<b>Control</b>	3.56	15.33	13.70
<b><math>4.86 \times 10^6</math> BCF beads</b>	5.47	16.36	13.60
<b>Change (%)</b>	53.65	6.72	0.73

Table 5.3 Simulated values of  $R_s$ , CPE and  $C_s$  in the equivalent circuit for control sample and sample with  $4.86 \times 10^6$  BCF microbeads and their respective percentage changes with respect to control

The presence of BCF microbeads increased the value of the bulk medium resistance by 53.65% when compared to the control sample. The presence of BCF microbeads increased the value of CPE by 6.72% when compared to the control sample. The value of  $C_s$  did not change significantly since the connecting wires, electrode chip and all other parameters in the system remained constant. The change in impedance due to the presence of BCF microbeads was dominated by change in the bulk medium resistance when compared to change in values of double layer capacitance and stray capacitance.

### 5.7.2 Immuno Microbead Based Insulin Detection

The procedure for determining the coupling efficiency of MAI-Ab and magnetic microbeads has been described in Chapter 3 under “Coupling efficiency determination”. The fluorescence values



measured for the provided BSA standards in the Quant-iT protein assay kit is shown in Figure 5.34.

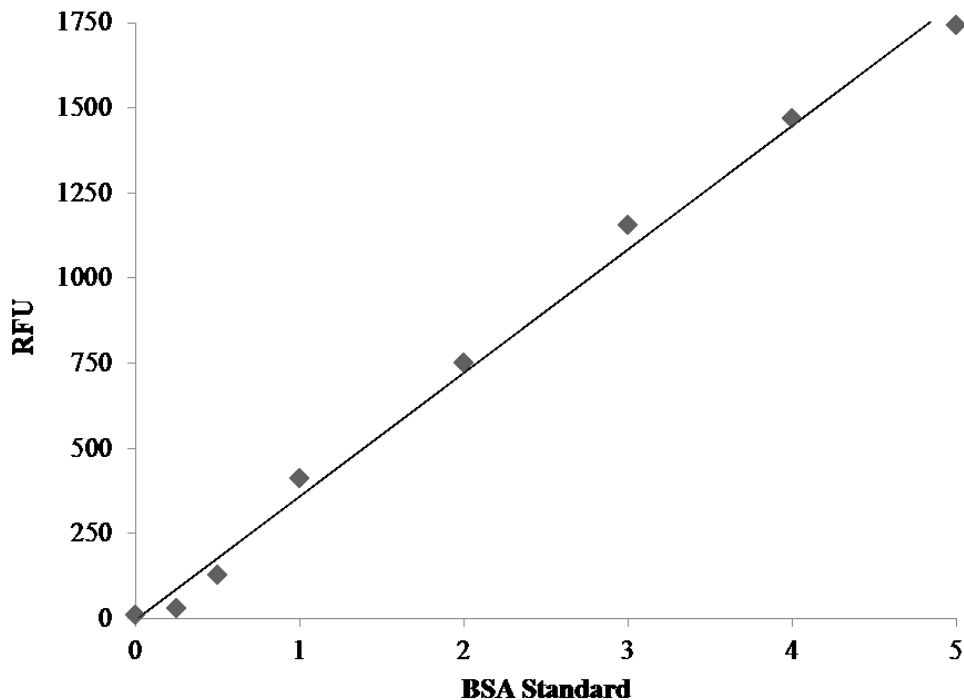


Figure 5.34 RFU vs concentration of BSA standards

Each data point is an average of three readings obtained by fluorescence measurements of three samples of each BSA standard. A standard curve was obtained by fitting a straight line to the data points. The coupling efficiency CE was calculated to be 85% using the following equation

$$CE = \frac{(\text{Pre-coupling sample RFU}) - (\text{Post-coupling sample RFU}) \times 100}{(\text{Pre-coupling sample RFU})} \quad (5.15)$$

The impedance spectrum (Bode plot representation) for all concentrations of insulin ranging from  $10^{-10}\text{M}$  to  $10^{-5}\text{M}$  is shown in Figure 5.35. The magnitude of impedance increased with an increase in the concentration of insulin.

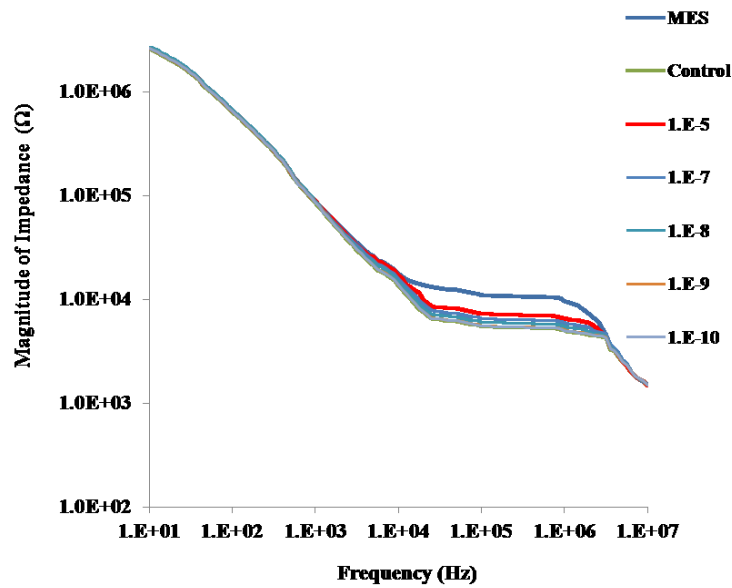


Figure 5.35 Impedance spectrum (Bode plot) for different concentrations of insulin

As shown in Figure 5.36, the impedance change (represented by NIC) showed an increase from 3% to 32% in the frequency range from 1 kHz to 28 kHz, remained constant at 32% in the frequency range from 28 kHz to 1 MHz, and then decreased from 32% to 1% at higher frequencies. A mid-frequency value of 100 kHz where a peak NIC was observed was selected to compare the impedance changes for all concentrations of insulin with respect to control. The magnitude of impedance measured at 100 kHz for different concentrations of insulin from  $10^{-10}$ M to  $10^{-5}$ M insulin is shown in Figure 5.37

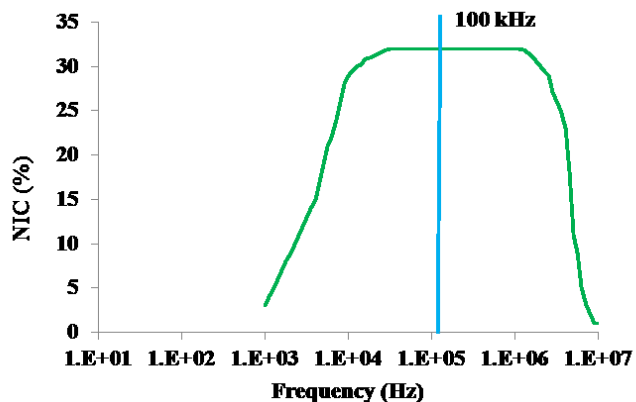


Figure 5.36 The difference in magnitude of impedance (represented by NIC) between  $10^{-5}$ M insulin sample and control sample. NIC was calculated for the measurements in the range of frequency from 1 KHz to 10 MHz.

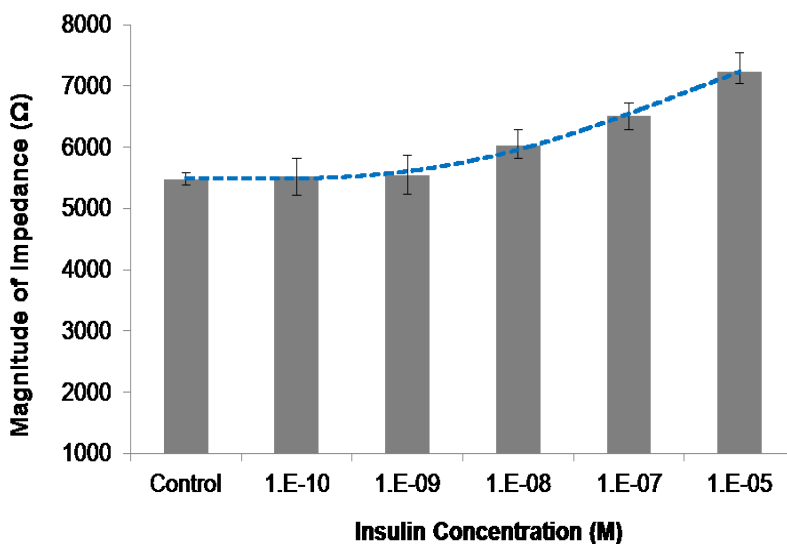


Figure 5.37 Magnitude of impedance at 100 kHz for various concentrations of insulin

Figure 5.38 shows the experimental and fitted data simulated from  $Z_{view}$  software based on equivalent circuit. The simulated values of  $R_s$ , CPE and  $C_s$  in the equivalent circuit for control sample and sample with insulin concentration of  $10^{-5}$ M are listed in Table 5.4. These values were obtained by curve fitting the respective experimental impedance data to the equivalent circuit.

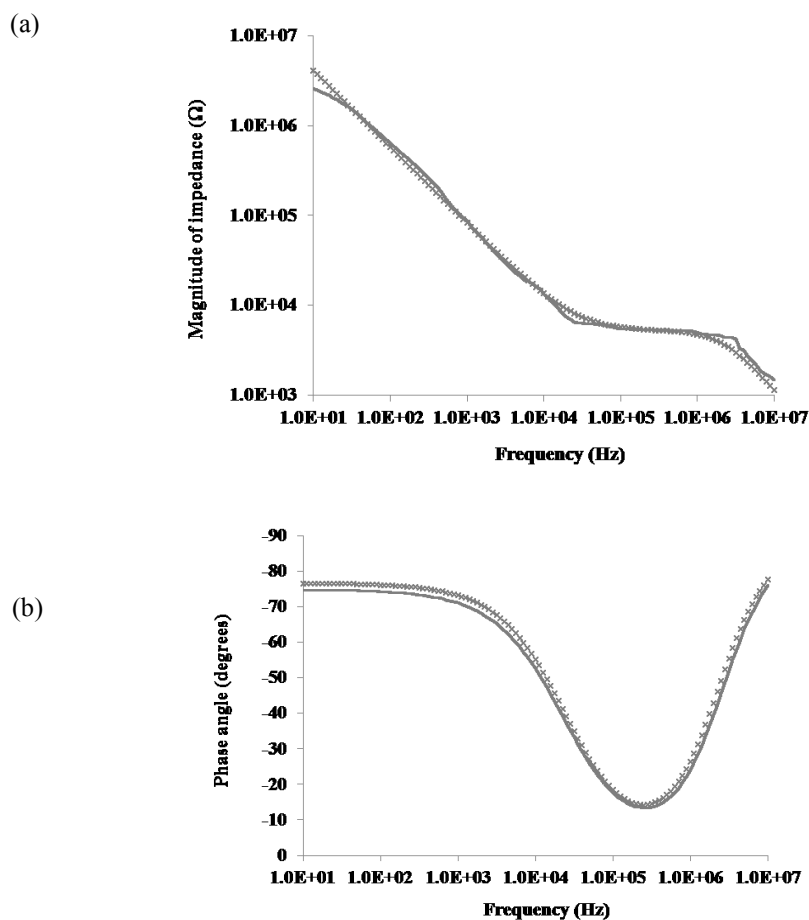


Figure 5.38 Bode plots of the impedance spectra of experimental and curve fitted data of control in the frequency range 10 Hz to 10 Mhz. Solid lines indicate the experimental data and crosses indicate the fitted data obtained from Zview software based on the equivalent circuit. (a) Magnitude of impedance (b) Phase angle in degrees

Sample	$R_s$ (k $\Omega$ )	CPE (nF)	$C_s$ (pF)
Control	5.23	14.46	13.50
$10^{-5}$ M insulin	6.73	16.19	13.70
Change (%)	28.68	11.96	1.48

Table 5.4 Simulated values of  $R_s$ , CPE and  $C_s$  in the equivalent circuit for control sample and sample with  $10^{-5}$ M insulin and their respective percentage changes with respect to control.

The presence of insulin increased the value of the bulk medium resistance by 28% when compared to the control sample. The presence of insulin increased the value of CPE by 12%

when compared to the control sample. The value of  $C_s$  did not change significantly (1.5%) since the connecting wires, electrode chip and all other parameters in the system remained constant. The change in net impedance due to the presence of insulin was dominated by change in the bulk medium resistance when compared to change in values of double layer capacitance and stray capacitance.

It can be observed from Figure 5.37 that there is no detectable difference in impedance between control and the lower insulin concentrations of  $10^{-10}$ M and  $10^{-9}$ M. The difference in average impedance with respect to control for  $10^{-10}$ M and  $10^{-9}$ M is only 0.8% and 1 % respectively. In case of insulin concentrations  $10^{-8}$ M,  $10^{-7}$ M and  $10^{-5}$ M there is a detectable difference with respect to control. The difference in average impedance with respect to control for insulin concentrations  $10^{-8}$ M,  $10^{-7}$ M and  $10^{-5}$ M was observed to increase linearly and was 10%, 19% and 32% respectively. The variation in impedance with respect to the average value for  $10^{-8}$ M,  $10^{-7}$ M and  $10^{-5}$ M is 10%, 7% and 7% respectively. There is not a detectable difference in impedance between concentrations of  $10^{-8}$ M and  $10^{-7}$ M when taking the variation with respect to the average impedance value into consideration. The lower detection limit is  $10^{-5}$ M with a 32% increase in the average impedance with respect to control. The total detection time was 20 minutes.

A multiwalled carbon nanotube/dihydropan (MWCNT/DHP) composite sensor for the electrochemical detection of insulin in a microphysiometer device has been reported [182]. This device has been reported to have a detection limit of  $10^{-6}$ M insulin, compared to the  $10^{-5}$ M detection limit achieved with the microfluidic system in this study. The microphysiometer device is more suitable for laboratory testing when compared to the fully integrated microfluidic system in the present study that can be used for point-of-care testing. The microphysiometer electrodes

had to be conditioned for 1 hour before any insulin testing. Also, the resistance of MWCNT/DHP film to shear force under flow conditions has been reported [182] to be a concern. The microelectrode used for impedance detection in this study does not require any conditioning and the stability of the electrodes under flow conditions was good.

## 6. CONCLUSIONS

The performance testing of the three micropump designs were successfully completed. The performance tests were performed to determine the flow rate variation with respect to actuation frequency and actuation pressure. The performance testing results indicated that the flow rate increased with frequency until a peak flow rate was observed at an optimum frequency. The flow rate dropped for frequencies higher than optimum frequencies. At frequencies below the optimum frequency, the flow rate increased with increasing pressure. The repeatability of flow rates within a micropump and also between multiple micropumps of each design was experimentally determined. The highest flow rate was observed in Design3 micropumps, with a peak flow rate of 16  $\mu\text{l}/\text{min}$  at 30 psi, 20 Hz operating condition. The mean variation in flow rate for a micropump of Design3 was 1.9%, with a maximum variation of 5.4% and a minimum variation of 0.8%. The fabrication yield with Design 3 was also observed to be higher than other designs. Based on the performance test results, Design3 was selected for the fully integrated microfluidic system. In order to better explain the results of the micropump performance and to validate the trend of flow rate variation with actuation frequency, an equivalent circuit simulation and COMSOL simulation was carried out. The simulation and experimental results showed a consistent trend for flow rate variation with respect to frequency and the peak flow rate at an optimum frequency.

The performance testing of three micromixer designs were successfully completed. Both qualitative and quantitative tests were performed. A qualitative testing based on mixing colored dyes indicated that the active mixing using a micromixer shortened the mixing time by 18 times when compared to mixing based on diffusion alone. The quantitative tests were performed to determine the mixing performance based on streptavidin-biotin conjugation reaction with respect

to flow rate and actuation frequency. The performance testing results indicated that the mixing efficiency increased with frequency until a peak mixing efficiency was observed at an optimum frequency. The mixing efficiency dropped for frequencies higher than optimum frequencies. The mixing efficiency was also observed to depend on the sample flow rates. The optimum flow rate for mixing efficiency was experimentally determined. The highest mixing efficiency was observed in Design3 micromixer, with an 85% mixing efficiency at an operating condition of 2  $\mu\text{L}/\text{min}$ , 10 Hz and 20 psi. Based on the performance test results, Design3 micromixer was selected for the fully integrated microfluidic system.

A micropump (Design3) and micromixer (Design3) were integrated on a single device to obtain an integrated micromixer-micropump and tested for mixing efficiency based on streptavidin biotin conjugation reaction. Based on the performance testing results, the optimum operating conditions for obtaining the highest mixing performance was determined to be 2  $\mu\text{L}/\text{min}$  sample flow rate, 10 Hz actuation frequency and a compressed air pressure of 20 psi. The micromixer was operated under these conditions for all further testing in the fully integrated microfluidic system.

The testing for magnetic microbead separation included both electromagnets and permanent magnets of various sizes and magnetic strengths. Three permanent magnets and three electromagnets of different size and strength were tested for their suitability in magnetic separation of SCP microbeads flowing within a microfluidic system. It was experimentally determined that the magnetic field strength generated electromagnets was not sufficient enough to overcome the hydrodynamic drag force for flow rates in the range 1 – 10  $\mu\text{L}/\text{min}$ . The test results with permanent magnet indicated that permanent magnet PM1 was suitable in separating



moving microbeads up to a flow rate of 10  $\mu\text{L}/\text{min}$ . Also, the compact size of makes it easier to integrate within the microfluidic system without interfering with the microfluidic connectors.

Multiple designs of IDE were successfully developed and tested for impedance spectrum measurements. A labVIEW plug and play instrument driver for HP4192A was downloaded from National Instruments website and modified to perform a log sweep. An impedance analyzer coupled with the labVIEW program was used to record the impedance spectrum measurements in a microfluidic system.

A fully integrated microfluidic system with a micropump, micromixer and IDE was successfully developed for detection of biomolecules. The fully integrated microfluidic system was used to detect target BCF microbeads and insulin. The detection of BCF microbeads was based on streptavidin-conjugation reactions between SCP microbeads and target BCF microbeads. Impedance spectrum measurements were made for concentrations of BCF microbeads ranging from  $1.9 \times 10^5$  to  $4.8 \times 10^6$  microbeads. The lower detection limit for BCF microbeads was experimentally determined to be  $1.9 \times 10^6$  microbeads. The insulin detection was based on mixing MBAC with target insulin molecules to allow binding reaction between target insulin molecules and MAI-Ab, and followed by impedance spectrum measurements. Impedance spectrum were made for insulin concentrations ranging from  $10^{-10}\text{M}$  to  $10^{-5}\text{M}$ . The lower detection limit for insulin detection was determined to be  $10^{-5}\text{M}$ . The total detection time was 20 minutes. An equivalent circuit analysis was performed to explain the impedance spectrum results.

## **7. FUTURE WORK**

Based on the results of the present study, some of the future work possibilities are discussed in the sections below.

### **7.1 Parallel Processing**

The fully integrated microfluidic system can be expanded to enable parallel processing of different insulin concentration samples simultaneously. Also, multiple testing of a single insulin sample can be performed simultaneously to confirm the reliability of the results.

### **7.2 Inclusion of Valves**

In the present study, a continuous flow microfluidic system was developed without any control valves. The inclusion of valves will be necessary for expanding the current design to perform parallel processing and will also provide better process control. For example, inclusion of valves in the micromixer mixing chamber would enable a closed system mixing and control over the residence time of the mixing species within the mixing chamber.

### **7.3 Nanobeads**

The replacement of microbeads with nanobeads can make the reaction kinetics faster and improve the capture efficiency. The high surface to volume ratio of nanobeads can reduce the quantity of bead sample required. However, the magnetic separation of nanobeads would require higher magnetic field strength when compared to microbeads.

### **7.4 COMSOL simulation**

A 3D COMSOL model can be implemented instead of the 2D model used in this study. Also, the model can be updated to include the effects of air bubbles within the microfluidic system and the

effects of pressure drop caused by the microfluidic connectors and external tubing on the microfluidic system. Also, COMSOL can be used for simulation of impedance change.

## **7.5 PDMS Alignment System**

All the alignments between different layers of PDMS in the present study were performed by manual alignment with tweezers under a stereo microscope. The development of a rapid and reproducible PDMS layer aligning and bonding system would improve the yield of fabrication.

## REFERENCES

- [1] S.C. Terry, "Ph.D. Thesis", Stanford, Stanford, CA, 1975
- [2] M. Esashi, S. Shoji, A. Nakano, *Sensors and Actuators*, 1989, 20, 163-169
- [3] S. Shoji, M. Esashi, T. Matsuo, *Sensors and Actuators*, 1988, 14, 101-107
- [4] T. Matsuo and K.D. Wise, "An integrated field effect electrode for biopotential recording", *IEEE Trans. Biomed. Eng.*, BME-21 (1974) 485-48
- [5] A. Manz, Y. Miyahara, J. Miura, Y. Watanabe, H. Miyagi, K. Sato, *Sens. Actuators* 1990, B1, 249-255
- [6] Dr. Janusz, "Roadmap to a \$1T MEMS market" <http://www.meptec.org/Resources>
- [7] L. Buchailot, E. Farnault, M. Hoummady, H. Fujita, *Jpn. J. Appl. Phys.* 2 36, L794 (1997)
- [8] M. A. Unger, H. P. Chou, T. Thorsen, A. Scherer and S. R. Quake, "Monolithic Microfabricated Valves and Pumps Using Multi-layer Soft Lithography," *Science*. 2000 Apr 7; 288 (5463):113-6.
- [9] M.J. Madou, "Fundamentals of microfabrication: the science of miniaturization", Boca Raton: CRC Press
- [10] D.B. Wolfe, D. Qin, and G.M. Whitesides, "Rapid prototyping of microstructures by soft lithography for biotechnology", *Methods in Molecular Biology: Microengineering in Biotechnology*, Humana Press, New York, NY, pp. 81-107 (2009).
- [11] D.C. Duffy, J.C. McDonald, O.J.A. Schueller and G.M. Whitesides, *Anal. Chem.*, 1998, 70, 4974-4984.
- [12] B.D. DeBusschere, D.A. Borkholder, and G.T.A. Kovacs, "Design of an integrated silicon-PDMS cell cartridge," in *Solid State Sens. Actuators Conf.*, Hilton Head, SC, June 1998, pp. 358-362.
- [13] S. Masuda, M. Washizu, and T. Nanba, "Novel method of cell fusion in field constriction area in fluid integrated circuit," *IEEE Ind. Applicat. Mag.*, vol. 25, pp. 732-737, 1989.
- [14] Y. Xia and G. Whitesides, "Soft lithography," *Angew Chem. Int. Ed.*, vol. 37, pp. 550-575, 1998.
- [15] K. Hosokawa, T. Fujii, and I. Endo, "Hydrophobic microcapillary vent for pneumatic manipulation of liquid in TAS," in *Process. uTAS '98*, Banff, Canada, pp. 307-310.
- [16] C.K. Malek, V. Saile, "Applications of LIGA Technology to Precision Manufacturing of High-aspect-ratio Micro-components and -systems: a Review", 2004

- [17] A. Bertsch, S. Jiguet, P. Renaud, “Microfabrication of ceramic components by microstereolithography”
- [18] S. Kaminaga, “Success in MEMS, from DRIE technology to social innovation” 2011, 3 pp., IEEE, Piscataway, NJ, USA
- [19] H. Lorenz, M. Despont, N. Fahrnl, N. LaBianca, P. Renaud, P. Vettiger, “SU-8: a low-cost negative resist for MEMS” *J Micromech Microengineering*, 1997, 7, 3, 121-4, IOP Publishing, UK
- [20] J.H. Leamon, W.L. Lee, K.R. Tartaro, J.R. Lanza, G.J. Sarkis, A.D. deWinter, J. Berka, and K.L. Lohman, “A massively parallel PicoTiterPlate™ based platform for discrete picoliter-scale polymerase chain reactions”, 2003, *Electrophoresis*, 24: 3769–3777
- [21] S. Takayama, E. Ostuni, P. LeDuc, K. Naruse, D.E. Ingber, G.M. Whitesides, “Subcellular positioning of small molecules”, 2001, *Nature*, 411, 1016
- [22] Jing Cheng, Larry J. Kricka, “Biochip Technology”, 2001, Chapter 1. Harwood Academic Publishers.
- [23] Daniel Mark, Stefan Haerberle, Gunter Roth, Felix von Stetten, Roland Zengerle, “Microfluidic lab-on-a-chip platforms: requirements, characteristics and applications” *Chem. Soc. Rev.*, -3, -1153, The Royal Society of Chemistry
- [24] Kumar A and G.M. Whitesides GM, *Appl. Phys. Lett.*, 1993, 63, 2002–2004
- [25] Olivier Lazcka, Javier Del Campo, Xavier Munoz, “Pathogen detection: A perspective of traditional methods and biosensors”, *Biosensors and Bioelectronics*, Volume 22, Issue 7, 15, 2007, 1205-1217
- [26] P. Leonard, S. Hearty, J. Brennan, L. Dunne, J. Quinn, T. Chakraborty, R. O’Kennedy, "Advances in biosensors for detection of pathogens in food and water", *Enzyme and Microbial Technology*, 2003,32, pp 3-13.
- [27] P. D. Patel, *Trends Anal. Chem.*, 2002, 21 (2), 96–115.
- [28] K.M.E Emde, H.Z Mao and G.R. Finch, “Detection and occurrence of waterborne bacterial and viral pathogens”, *Water Environment Research*,1992,64(4), pp 641– 647
- [29] J. Theron, J. Cilliers, M. Du Preez, V.S. Brözel, S.N. Venter “Detection of toxigenic *Vibrio cholerae* from environmental water samples by an enrichment broth cultivation-pit-stop semi-nested PCR procedure.” *Journal of Applied Microbiology*, 2000, 89(3),pp 539-46.
- [30] Atlas, 1999, <http://www.idf.org/diabetesatlas/>
- [31] F.L. Bryan, “Diseases transmitted by foods. Atlanta” Centers for Disease Control, 1982.

- [32] P.S. Mead, L. Slutsker, V. Dietz, L.F. McCaig, J.S. Bresee, C. Shapiro, P.M.Griffin, and R.V. Tauxe, “Food-Related Illness and Death in the United States”, 1999, *Emerging Infectious Diseases* 5(5): 607-25.
- [33] E.C. Alocilja and S. Radke, “Market Analysis of Biosensors for Food Safety”, *Biosensors and Bioelectronics Journal*, 2003, 18(5-6):841-846
- [34] American Cancer Society. *Cancer Facts and Figures 2006*. Atlanta: American Cancer Society; 2006.
- [35] P. Hogan, T. Dall, P. Nikolov, “Economic costs of diabetes in the US in 2002”, *Diabetes Care* 2003; 26:917- 932.
- [36] C.H. Ahn, Jin-Woo Choi, G. Beaucage, J.H. Nevin, Jeong-Bong Lee, A. Puntambekar, J.Y. Lee, “Disposable Smart Lab On A Chip For Point-Of-Care Clinical Diagnostics”, *Proceedings of the IEEE* Volume 92, Issue 1, Jan 2004 pp. 154-173.
- [37] A.J. Baeumner, N. A. Schlesinger, N.S. Slutzki, J. Romano, E.M. Lee, R. A. Montagna, "Biosensor for Dengue Virus Detection: Sensitive, Rapid, and Serotype Specific", *Anal. Chem.*, 2002, 74 (6), pp 1442–1448
- [38] P. Crepin, L. Audry, Y. Rotivel, A. Gacoin, C. Caroff, H. Bourhy, "Intravital Diagnosis of Human Rabies by PCR Using Saliva and Cerebrospinal Fluid", *J. Clin. Microbiol.* April 1998 vol. 36 no. 4 1117-1121
- [39] D.J. Hu, A. Buvé, J. Baggs, G. van der Groen, T.J. Dondero, “What role does HIV-1 subtype play in transmission and pathogenesis? An epidemiological perspective” *AIDS* 1999; 13: 873–81
- [40] R.L. Caygill, C.S. Hodges, J.L. Holmes, S.P. Higson, G.E. Blair, P.A. Millner, "Novel impedimetric immunosensor for the detection and quantitation" *Biosensors and Bioelectronics* Volume 32, Issue 1, 15 February 2012, Pages 104–110
- [41] E.C.D Todd, “Preliminary estimates of costs of foodborne diseases in the United States”, 1989, *J.Food Prot.* 52(8): 595-601
- [42] R.A.M Fouchier, V.J. Munster, A. Wallensten, T.M. Bestebroer, R. Herfst, D.J. Smith, G.F. Rimmelzwaan, B. Olsen and A.D.M.E Osterhaus, “Characterization of a novel influenza A virus hemagglutinin subtype (H16) obtained from black-headed gulls”, 2005, *Journal of Virology* 79: 2814–2822.
- [43] T. Horimoto, Y. Kawaoka, “Influenza: lessons from past pandemics, warnings from current incidents”, 2005, *Nat. Rev. Microbiol.* 3, 591–600.
- [44] CDC, 2009, <http://www.cdc.gov/>
- [45] IDF, <http://www.idf.org/>

- [46] Germán Campetelli, David Zumoffen, and Marta Basualdo, “Improvements on Noninvasive Blood Glucose Biosensors Using Wavelets for Quick Fault Detection,” *Journal of Sensors*, vol. 2011, Article ID 368015, 11 pages, 2011.
- [47] A. Thomas, M. Thevis, P. Delahaut, A. Bosseloir, W. Schänzer, “Mass spectrometric identification of degradation products of insulin and its long-acting analogues in human urine for doping control purposes.” *Anal Chem*, 2007, 79:2518–2524
- [48] J.M. Neal, W. Han, “Insulin immunoassays in the detection of insulin analogues in factitious hypoglycemia”, 2008, *Endocr. Pract.* 14: 1006–1010
- [49] Y.M. Bae, B.K. Oh, W. Lee, W.H. Lee, J.W. Cho, "Detection of insulin-antibody binding on a solid surface using imaging ellipsometry," 2004, *Biosensors and Bioelectronics*, 20, 895-902
- [50] Y. Wang, J.H. Li, “A Carbon Nanotubes Assisted Strategy for Insulin Detection and Insulin Proteolysis Assay”, *Anal. Chim. Acta*, 2009, 650, 49–53
- [51] A. Arvinte, A.C. Westermann, A.M. Sesay, V. Virtanen, “Electrocatalytic oxidation and determination of insulin at CNT-nickel-cobalt-oxide modified electrode” *Sensors and Actuators B*, 2010, 150 (2): 756-763.
- [52] M. Frasconi, C. Tortolini, F. Botrè, F. Mazzei, “Multifunctional au nanoparticle dendrimer-based surface plasmon resonance biosensor and its application for improved insulin detection” *Anal Chem.* 2010; 82: 7335-42.
- [53] P.A. Lieberzeit, A. Afzal, D. Podlipna, S. Krassnig, H. Blumenstock, F.L. Dickert, “Printing materials in micro- and nano-scale: Systems for process control.” *Sensors and Actuators B: Chemical* 2006
- [54] R.R. Holman, "Assessing the potential for alpha-glucosidase inhibitors in prediabetic states" *Diabetes Res Clin Pract.* 1998 Jul; 40 Suppl: S21-5
- [55] M. Tietjen and D.Y.C Fung, “Salmonellae and food safety”, *Crit. Rev. Microbiol.* 21 (1995), pp. 53–83
- [56] B. Bork, H. Stryhn, A.K. Ersboll, K. Pedersen, “Thermophilic *Campylobacter* spp. in turkey samples: evaluation of two automated enzyme immunoassays and conventional microbiological techniques.” *J. Appl Microbiol* 2002; 92:574-82
- [57] R.W. Bennett, "Staphylococcal enterotoxin and its rapid identification in foods by enzyme-linked immunosorbent assay-based methodology" *J Food Prot.* 2005 Jun; 68(6):1264-70
- [58] A.G. Gehring, P.L. Irwin, S.A. Reed, S. Tu, “Enzyme-linked immunomagnetic chemiluminescence incorporating anti-h7 and anti-O157 antibodies for the detection of escherichia coli O157:H7”, 2006, *Journal of Rapid Methods and Automation in Microbiology.* 14:349-361.

- [59] J.S. Dickson, J.A. Chen, "Fast and accurate detection method of E.coli O157:H7 in beef" Abstr Gen Meet Am Soc Microbiol, 2001, 101:573
- [60] P.T. Feldsine, M.T. Falbo-Nelson, S.L. Brunelle, R.L. Forgey, "Visual immunoprecipitate assay (VIP) for detection of enterohemorrhagic Escherichia coli (EHEC) O157:H7 in selected foods: collaborative study", 1997, J AOAC Int. May-Jun; 80(3):517-29.
- [61] A. Rasooly, R.S. Rasooly, "Detection and analysis of Staphylococcal enterotoxin A in food by Western immunoblotting", 1998, Int J Food Microbiol. Jun 16; 41(3):205-12.
- [62] J. Meng, M.P. Doyle, "Introduction. Microbiological food safety" Microbes Infect. 2002 Apr; 4(4):395-7.
- [63] K. Mullis, F. Faloon, S. Scharf, R. Saiki, G. Horn, H. Erlich, Cold Spring Harbor Symposia on Quantitative Biology, 1986, 51, 263–273
- [64] C.A. Batt, "Food pathogen detection", Science 2007; 316:1579-80
- [65] S.F. D' Souza, "Microbial biosensors", 2001, Biosensors and Bioelectronics, 16(6): 337-53
- [66] J.C. Ehrhart, B. Bennetau, L. Renaud, J.P. Madrange, L. Thomas, J. Morisot, A. Brosseau, S. Allano, P. Tauc, P.L. Tran, "A new immunosensor for breast cancer cell detection using antibody-coated long alkylsilane self-assembled monolayers in a parallel plate flow chamber" Biosensor and Bioelectronics, 2008, 24, 467-474.
- [67] V. Mani, B.V. Chikkaveeraiah, V. Patel, J.S. Gutkind, J.F. Rusling, "Ultrasensitive immunosensor for cancer biomarker proteins using gold nanoparticle film electrodes and multienzyme-particle amplification", 2009, ACS Nano, 3: 585-594
- [68] E. Carnes, E. Wilkins, "The Development of A New, Rapid, Amperometric Immunosensor for the Detection of Low Concentrations of Bacteria Part I: Design of the Detection System and Applications", American Journal of Applied Sciences, 2 (3):597-606, 2005
- [69] M.K.A. Kadir, I.E. Tothill, "Development of an Electrochemical Immunosensor for Fumonisin Detection in Foods", 2010, Toxins 2: 382—398.
- [70] J. Katrlík, A. Pizzariello, V. Mastihuba, J. Švorc, M. Stred'anský, S. Miertuš, "Biosensors for L-malate and L-lactate based on solid binding matrix", 1999, Analytica Chimica Acta, 379, 193-200
- [71] J. Katrlík, J. Švorc, M. Stred'anský, S. Miertuš, "Composite alcohol biosensors based on solid binding matrix", 1998, Biosensors and Bioelectronics, 13:181–91.
- [72] J.C. Vidal, J. Espuelas, E. Garcia-Ruiz, J.R. Castillo, "Amperometric cholesterol biosensors based on the electropolymerization of pyrrole and the electrocatalytic effect of Prussian-Blue layers helped with self-assembled monolayers", 2004, Talanta, 64, 655-664.



- [73] B. Elsholz, R. Wörl, L. Blohm, J. Albers, T. Grunwald, B. Jürgen, T. Schweder, H. Feucht and R. Hintsche, “Automated detection and quantitation of bacterial RNA by using electrical microarrays”, *Analytical Chemistry*, 2006, 78, 4794-4802
- [74] R.S. Mikkelsen, E. Corton, *Bioanalytical Chemistry*, 2004, Hoboken, N.J., John Wiley and Sons.
- [75] J. Homola, *Anal Bioanal Chem*, 2003, 377:528–539
- [76] D.J. Schofield, N.J. Dimmock, *J Virol Methods*, 1996, 62:33–42
- [77] P.M. Boltovets, V.R. Boyko, I.Y. Kostikov, N.S. Dyachenko, B.A. Snopok, Y.M. Shirshov, *J Virol Methods*, 2002, 105:141–146
- [78] K. Bizet, C. Gabrielli, H. Perrot, *Analysis*, 1999, vol. 27, p. 609.
- [79] M.A. Cooper, F.N. Dultsev, T. Minson, V.P. Ostanin, C. Abell, D. Klenerman, *Nat Biotechnol*, 2001, 19:833–837
- [80] A. Gupta, D. Akin, R. Bashir, “Single virus particle mass detection using microresonators with nanoscale thickness”, 2004, *Applied Physics Letters*, 84(11), pp. 1976–1978
- [81] J.M. Kauffmann, G.G. Guilbault, “Potentiometric enzyme electrodes” *Bioprocess Technol.* 15: 63–82, 1991.
- [82] J. Wang, “Amperometric biosensors for clinical and therapeutic drug monitoring: a review” *J. Pharm. Biomed. Anal.* 19:47–53, 1999.
- [83] H. Ohnuki, T. Saiki, A. Kusakari, H. Endo, M. Ichihara, M. Izumi M, “Incorporation of glucose oxidase into languir-blodgett films based on Prussian blue applied to amperometric glucose biosensor” *Langmuir* 23:4675–4681, 2007.
- [84] S.A. Marzouk, S.S. Ashraf, K.A. Tayyari, “Prototype amperometric biosensor for sialic acid determination” *Anal. Chem.* 79:1668–1674, 2007.
- [85] M. Yemini, Y. Levi, E. Yagil, J. Rishpon, “Specific electrochemical phage sensing for *Bacillus cereus* and *Mycobacterium smegmatis*” *Bioelectrochemistry* 70:180–184, 2007.
- [86] M. Pohanka, P. Skládal, M. Kroča, “Biosensors for biological warfare agent detection” *Def. Sci. J.* 57:185–193, 2007b.
- [87] G. Liu, Y. Lin, “Biosensor based on self-assembling acetylcholinesterase on carbon nanotubes for flow injection/amperometric detection of organophosphate pesticides and nerve agents” *Anal. Chem.* 78:835–843, 2006
- [88] Y. Wang, Q. Chen, X. Zeng, “Potentiometric biosensor for studying hydroquinone cytotoxicity in vitro.” *Biosensor and Bioelectronics*, 2010, 25(6):1356-62.
- [89] A. W. Bott, “Electrochemical techniques for the characterization of redox polymers” *Curr.Sep.* , 2001, 19, 71–75.

- [90] J. Guam, Y. Miao, Q. Zhang, *J. Biosci. Bioeng.*, 2004, 97 (4), 219–226.
- [91] L. Yang, Y. Li, G.F. Erf, *Anal. Chem.*, 2004a 76, 1107–1113
- [92] S.M. Radke, E.C. Alocilja, *IEEE Sens. J.*, 2004, 4 (4), 434–440.
- [93] L. Yang, Y. Li, *Biosens. Bioelectron.*, 2005, 20, 1407–1416.
- [94] R. Gomez, R. Bashir, A.K. Bhunia, *Sens. Actuators*, 2002, B 86, 198–208.
- [95] R. Gomez-Sjoberg, T. Morissette, R. Bashir, *J. Microelectromech. Syst.*, 2005, 14 (4), 829–838.
- [96] L. Yang, Y. Li, *J. Microbiol. Method*, 2006, 664 (1), 9–16
- [97] H. Li, R. Bashir, *Sens. Actuators*, 2002, B 86, 215–221
- [98] J. Suehiro, R. Yatsunami, R. Hamada, M. Hara, *J. Appl. Phys.*, 1999, 32, 2814–2820.
- [99] J. Suehiro, D. Noutomi, R. Hamada, M. Hara, *IEEE*, 2001, 1950–1955.
- [100] F. Aldaeus, Y. Lin, J. Roeraade, G. Amberg, *Electrophoresis*, 2005, 26, 4252–4259
- [101] W. Laureyn, D. Nelis, P. Van Gerwen, K. Baert, L. Hermans, R. Magnee, J.J. Pireaux, G. Maes, *Sens. Actuators B*, 2000, 68, 360–370.
- [102] Ruan, C., Yang, L., Li, Y., 2002. *Anal. Chem.* 74, 4814–4820.
- [103] Kim, S.K., Hesketh, P.J., Li, C., Thomas, J.H., Halsall, H.B., Heineman, W.R., 2004. *Biosens. Bioelectron.* 20, 887–894.
- [104] Thomas, J.H., Kim, S.K., Hesketh, P.J., Halsall, H.B., Heineman, W.R., 2004. *Anal. Biochem.* 328, 113–122.
- [105] M.L. Antonelli, C. Spadaro, R.F. Tornelli, “A microcalorimetric sensor for food and cosmetic analyses: l-Malic acid determination”, *Talanta*, 2008 Feb 15;74(5):1450-4.
- [106] H.C. Ng Alphonsus, U. Uddayasankar, A.R. Wheeler "Immunoassays in microfluidic systems" *Anal Bioanal Chem* (2010) 397:991–1007
- [107] A.J. de Mello, Nigel Beard, “Dealing with ‘real’ samples: sample pre-treatment in microfluidic systems”, *Lab Chip*, 2003,3, 11N-20N
- [108] C.T. Lim, Y. Zhang, "Bead-based microfluidic immunoassays: The next generation" *Biosensors and Bioelectronics*, 2007, 22, 1197–1204

- [109] H. Miyaguchi, H. Takahashi, T. Ohashi, K. Mawatari, Y.T. Iwata, H. Inoue, T. Kitamori “Rapid analysis of methamphetamine in hair by micropulverized extraction and microchip-based competitive ELISA” *Forensic Science International*, 2009,184(1-3):1-5.
- [110] D. Holmes, J.K. She, P.L. Roach, H. Morgan, “Bead-based immunoassays using a microchip flow cytometer.” *Lab on a Chip.* , 2007, 7:1048–1056
- [111] V. Sivagnanam, B. Song, C. Vandevyver, M.A.M. Gijs, “On-chip immunoassay using electrostatic assembly of streptavidin-coated bead micropatterns” *Analytical Chemistry*, 2009, 81: 6509-6515
- [112] M.A. Hayes, N.A. Polson, A.N. Phayre, A.A. Garcia, “Flow-based microimmunoassay”, *Analytical Chemistry.*, 73, 5896–5902, 2001.
- [113] J.H. Cho, S.M. Han, E.H. Paek, I.H. Cho, S.H. Paek “Plastic ELISA- on-a-chip based on sequential cross-flow chromatography”. *Analytical Chemistry*, 2006, 78:793–800
- [114] H. Yousef, S. Reyad, C. Irina, Q. Ahmad, L.T. Ee and G.O. Keat, “Magnetic Techniques for Rapid Detection of Pathogens”, *Principles of Bacterial Detection: Biosensors, Recognition Receptors and Microsystems*, 2008, Springer Science, II, 415-458
- [115] A. Manz, N. Graber, H.M. Widmer, “Miniaturized total chemical analysis systems : A novel concept for chemical sensing”, 1990, *Sensors and Actuators B1*:244-248.
- [116] P.A. Auroux, Y. Koc, A deMello, A. Manz, P.J. Day “Miniaturised nucleic acid analysis” *Lab on a Chip*, 2004, 4, 534–546
- [117] D.J. Laser, J.G. Santiago, “A review of micropumps”, *J. Micromech. Microeng.* 2004, 14(6), R35–R64.
- [118] J. Dopfer, M. Clemens, W. Ehrfeld, S. Jung, K.P. Kämper, H. Lehr “Micro gear pumps for dosing of viscous fluids” *J. Micromech. Microeng.* 7 230–2
- [119] M. Koch, N. Harris, A.G.R. Evans, N.M. White, A. Brunnschweiler, “A novel micromachined pump based on thick-film piezoelectric actuation”, 1998, *Sensors Actuators A* 70 98–103
- [120] V. Gass V, B.H. Vanderschoot, S. Jeanneret, N.F. Derooij, “Integrated flow-regulated silicon micropump”, 1994, *Sensors Actuators A* 43 335–8
- [121] H.J. Yoon, W.Y. Sim, S.S. Yang. “The fabrication and test of a phase-change micropump”, 2001, *Proc. ASME Int. Mechanical Engineering Congress and Exposition (New York)*
- [122] A. Wego, L. Pagel, “A self-filling micropump based on PCB technology *Sensors*”, 2001, *Sensors Actuators A* 88 220–6

- [123] W.H. Grover, A.M. Skelley, C.N. Liu, E.T. Lagally, R.A. Mathies, "Monolithic membrane valves and diaphragm pumps for practical large-scale integration into glass microfluidic devices", 2003, *Sensors Actuators B* 89 315–23
- [124] J.G. Smits, "Piezoelectric micropump with 3 valves working peristaltically", 1990, *Sensors Actuators A* 21 203–6
- [125] R. Zengerle, J. Ulrich, S. Kluge, M. Richter, A. Richter, "A bidirectional silicon micropump", 1995, *Sensors Actuators A*, 50 81–6
- [126] S. Zimmermann, J.A. Frank, D. Liepmann, A.P. Pisano, "A planar micropump utilizing thermopneumatic actuation and in-plane flap valves", 2004, *Proc. 17th IEEE Int. Conf. on Micro Electro Mechanical Systems (Maastricht, The Netherlands)*
- [127] R. Rapp, W.K. Schomburg, D. Maas, J. Schulz, W. Stark, "LIGA micropump for gases and liquids", 1994, *Sensors Actuators A* 40 57–61
- [128] S. Bohm, W. Olthuis, P. Bergveld, "A plastic micropump constructed with conventional techniques and materials", 1999, *Sensors Actuators A* 77 223–8
- [129] H.T.G. Van Lintel, F.C.M. Van de Pol, S. Bouwstra, "A piezoelectric micropump based on micromachining of silicon", 1988, *Sensors and Actuators*, 15, 153–67
- [130] E. Stemme, G. Stemme, "A valveless diffuser/nozzle-based fluid pump", 1993, *Sensors Actuators A* 39 159–67
- [131] G. Fuhr, T. Schnelle, B. Wagner, "Traveling wave-driven microfabricated electrohydrodynamic pumps for liquids", 1994, *J. Micromech. Microeng.* 4 217–26
- [132] S. Jeong, J. Seyed-Yagoobi, "Experimental study of electrohydrodynamic pumping through conduction phenomenon", 2002, *J. Electrostat.* 56 123–33
- [133] A. Richter, A. Plettner, K.A. Hofmann, H. Sandmaier, "A micromachined electrohydrodynamic (EHD) pump", 1991, *Sensors Actuators A* 29 159–68
- [134] P.K. Dasgupta, S. Liu, "Auxiliary electroosmotic pumping in capillary electrophoresis", 1994, *Anal. Chem.* 66 3060–5
- [135] R.S. Ramsey, J.M. Ramsey, "Generating electrospray from microchip devices using electroosmotic pumping", 1997, *Anal. Chem.* 69 1174–8
- [136] T.E. McKnight, C.T. Culbertson, S.C. Jacobson, J.M. Ramsey, "Electroosmotically induced hydraulic pumping with integrated electrodes in microfluidic devices", 2001, *Anal. Chem.* 73 4045–9

- [137] A. E. Kamholz, B.H. Weigl, B.A. Finlayson, Paul Yager, “Quantitative analysis of molecular interactive in microfluidic channel: the T-sensor”, 1999, *Anal.Chem.* 71 5340–7
- [138] R.F. Ismagilov, A.D. Stroock, P.J.A. Kenis, G. Whitesides, H.A. Stone, “Experimental and theoretical scaling laws for transverse diffusive broadening in two-phase laminar flows in microchannels”, 2000, *Appl. Phys.Lett.* 76 2376–78
- [139] R. Miyake, T.S.J Lammerink, M. Elwenspoek, J.H.J. Fluitman, “Micro mixer with fast diffusion”, 1993, *Proc.MEMS’93*, 6th IEEE Int. Workshop Micro Electromechanical System (San Diego, CA) pp 248–53
- [140] Y. Lin, G.J. Gerfen, D.L. Rousseau, S.R. Yeh, “Ultrafast microfluidic mixer and freeze–quenching device” *Anal. Chem.* 75 5381–6
- [141] H. Song, M.R. Bringer, J.D. Tice, C.J. Gerdts, R.F. Ismagilov, “Experimental test of scaling of mixing by chaotic advection in droplets moving through microfluidic channels”, 2003, *Appl. Phys. Lett.* 83 4664–6
- [142] A. Deshmukh, D. Liepmann, A.P. Pisano, “Characterization of a micro-mixing, pumping, and valving system”, 2001, *Proc. Transducers’01*, 11th Int. Conf. on Solid-State Sensors and Actuators (Munich, Germany) pp 779–82
- [143] A.O. El Moctar, N. Aubry, J. Batton, “Electro–hydrodynamic micro–fluidic mixer Lab on a Chip”, 2003, 3 273–80
- [144] Deval J, Tabeling P and Ho C M 2002 A dielectrophoretic chaotic mixer *Proc. MEMS’02*, 15th IEEE Int. Workshop Micro Electromechanical System (Las Vegas, Nevada) pp 36–9
- [145] H.H. Bau, J. Zhong, M. Yi, “A minute magneto hydro dynamic (MHD) mixer”, 2001, *Sensors Actuators B* 79 207–15
- [146] S.C. Jacobson, T.E. McKnight, J.M. Ramsey, “Microfluidic devices for electrokinematically driven parallel and serial mixing”, 1999, *Anal. Chem.* 71 4455–9
- [147] R.M. Moroney, R.M. White, R.T. Howe “Ultrasonically induced microtransport”, 1991, *Proc. MEMS’91*, 3th IEEE Int. Workshop Micro Electromechanical System (Nara, Japan) pp 277–82
- [148] Z. Wu, N. Nguyen, “Convective–diffusive transport in parallel lamination micromixers”, 2005, *Microfluid Nanofluid* 1(3):208–217
- [149] M. Yamada, M. Nakashima, M. Seki, *Analytical Chemistry*, 2004, 76, 5465.
- [150] M. Yamada, M. Seki, *Analytical Chemistry*, 2006, 78, 1357
- [151] P. Sethu, A. Sin, M. Toner M, *Lab on a Chip*, 2006, 6, 83.

- [152] L.R. Huang LR, Cox EC, Austin RH and Sturm JC, *Science*, 2004, 304, 987.
- [153] I. Doh, Y.H. Cho, *Sensors and Actuators, A*, 2005, 121, 59.
- [154] C.H. Ahn, M.G. Allen, W. Trimmer, Y.N. Junand, S. Erramilli, “A fully integrated micromachined magnetic particle separator”, *Journal of Microelectromechanical Systems*, 1996, 5, 151.
- [155] J.W. Choi, T. M. Liakopoulos, C. H. Ahn, “An on-chip magnetic bead separator using spiral electromagnets with semi-encapsulated permalloy”, *Biosensors and Bioelectronics*, 2001, 16, 6, 409-416
- [156] J.W. Choi, C. H. Ahn, S. Bhansali, H. T. Henderson, “A New Magnetic Bead-Based, Filterless Bio-Separator with Planar Electromagnet Surfaces for Integrated Bio-Detection Systems” *Sensors and Actuators B*, Vol. 68, pp. 34-39, 2000.
- [157] Nicole Pamme “Magnetism and microfluidics” *Lab on a Chip*, 6:24 38, 2006
- [158] J.R. Macdonald, “Impedance Spectroscopy”, 1987, Wiley, New York
- [159] M.B. Xavier, G. Neus, L. Olivier, B. Eva, X.M. Francesc, J.D.C. Fco, “Impedance-Based Biosensors for Pathogen Detection”, *Principles of Bacterial Detection: Biosensors, Recognition Receptors and Microsystems*, 2008, Springer Science, II, 341-376
- [160] D. Linda, W.A. Brian, “Design for manufacture of a micro-interdigitated electrode for impedance measurement in a biochemical assay”, 2012, *Proceedings of the SPIE*, Volume 8251, pp. 82510Y-1 to 82510Y-6
- [161] R. Qasem, S. Victor, P.P. Daniel, Y. Chen, “An integrated microfluidic platform for magnetic microbeads separation and confinement” 2006, *Biosensors and Bioelectronics*, Volume 21, Issue 9, 15, 1693–1702
- [162] E.P. Diamandis, T.K. Christopoulos, “The biotin-(strept)avidin system: principles and applications in biotechnology” *Clin Chem*. 1991 May;37(5):625-36.
- [163] W.Y. Zhang, G.S. Ferguson, S. Tatic-Lucic. “Elastomer-supported cold welding for room temperature wafer-level bonding.” *MEMS 2004 Technical Digest*, Maastricht, The Netherlands, January 25-29, 2004, 741-744
- [164] M. Kawabe, S. Tasaka, N. Inagaki, “Effects of surface modification by oxygen plasma on peel adhesion of pressure-sensitive adhesive tapes” *J. Appl. Polym. Sci.*, 78, p. 1392, 2000
- [165] R. Mukhopadhyay, “When PDMS isn't the best. What are its weaknesses, and which other polymers can researchers add to their toolboxes?” *Anal Chem*. 2007 May 1; 79(9):3248-53.

- [166] H. Makamba, J.H. Kim, K. Lim, N. Park, J.H. Hahn, "Surface Modification of Poly(dimethylsiloxane) Microchannels" *Electrophoresis* 2003, 24, 3607-3619.
- [167] Z. Wu, K. Hjort, "Surface modification of PDMS by gradient-induced migration of embedded Pluronic" *Lab Chip*, 2009, 9, 1500-1503
- [168] Y.C. Hsu, N.B. Le, "Equivalent electrical network for performance characterization of piezoelectric peristaltic micropump", *Microfluidics Nanofluidics*, 2009, 7, 237-248
- [169] H. Lai, A. Folch, "Design and dynamic characterization of "single-stroke" peristaltic PDMS micropumps", *Lab on a Chip*, 2011, 11(2), 336-342
- [170] X Thomas, "Silicones in Medical Applications", [www.DowCorning.com](http://www.DowCorning.com)
- [171] T. Bourouina, J.P. Grandchamp, "Modeling micropumps with electrical equivalent networks", *J. Micromech. Microeng.* 6 (1996) 398-404
- [172] R.E. Oosterbroek, "Modelling, design and realization of microfluidic components" PhD thesis, Univ. of Twente., MESA Research Institute, 1999
- [173] E. Morganti, I. Fuduli, A. Montefusco, M. Petasecca, G.U. Pignatelli, "SPICE modelling and design optimization of micropumps", *IAEAC*, vol.85, pp. 687-699 (2005)
- [174] D. Armani D, N. Aluru, C. Liu, "Re-configurable fluid circuits by PDMS elastomer micromachining", pp 222-227, *MEMS '99. Twelfth IEEE International Conference on Micro Electro Mechanical Systems*
- [175] N.T. Nguyen, Z. Wu, "Micromixers- A review", *Journal of Micromechanics and Microengineering*, 2005, 15 R1
- [176] L. Capretto, W. Cheng, M. Hill, X. Zhang, "Micromixing Within Microfluidic Devices", *Topics in Current Chemistry Volume 304*, 2011, pp 27-68
- [177] Y. Wang, J. Zhe, B.T.F. Chung, P. Dutta, "A rapid magnetic particle driven micromixer", *Microfluid Nanofluid* (2008) 4:375-389
- [178] A.Z. Kouzani, K. Khoshmanesh, S. Nahavandi and J.R. Kanwar, "A microfluidic electroosmotic mixer and the effect of potential and frequency on its mixing efficiency", *Proceedings of the IEEE International Conference on Systems, Man and Cybernetics*, IEEE, 2009, pp. 4618-4622
- [179] L. Yang, Y. Li, G.F. Erf, "Interdigitated array microelectrode-based electrochemical impedance immunosensor for detection of *Escherichia coli* O157:H7", *Analytical Chemistry*. 76 (2004) 1107-1113.
- [180] W. Laureyn, D. Nelis, P. Van Gerwen, K. Baert, L. Hermans, R. Magnee, J.J. Pireaux, J. Maes, "Nanoscale interdigitated titanium electrodes for impedimetric biosensing", *Sensors and Actuators B*, 68 (2000) 360-370

- [181] S. Gawad, K. Xheung, U. Seger, A. Bertsch, P. Renaud, "Dielectric spectroscopy in a micromachined flow cytometer: theoretical and practical considerations", *Lab Chip* 4 (2004) 241–251.
- [182] R.M. Snider, M. Ciobanu, A.E. Rue, D.E. Cliffler, "A multiwalled carbon nanotube/dihydropyran composite film electrode for insulin detection in a microphysiometer chamber" *Anal Chim Acta*. 2008 Feb 18;609(1):44-52